NATIONAL INSTITUTE FOR FUSION SCIENCE

Recent trends in technologies of pulse power, high-density plasma and particle beams

Edited by Koichi Takaki and Tetsuo Ozaki

(Received - March. 20, 2023)

NIFS-PROC-125 July. 1, 2023

Recent trends in technologies of pulse power, high-density plasma and particle beams

Edited by Koichi Takaki and Tetsuo Ozaki

January 10-11, 2023
National Institute for Fusion Science
Toki, Gifu, Japan

Abstract

The papers appeared in this volume of research reports have been presented at the “Recent trends in technologies of pulse power, high-density plasma and particle beams” in online style arranged by National Institute for Fusion Science. They reported the recent progress in experimental and theoretical studies on pulsed power technology and its applications.

Keywords: pulsed power, particle beam, plasma, high power microwave, bio application, atmospheric pressure plasma

Some figures and tables are in color only PDF.

Editor’s Preface

The collaborative research symposium on “Recent trends in technologies of pulse power, high-density plasma and particle beams" was held as online style (Zoom meeting ID: 899 2830 5305) arranged by National Institute for Fusion Science (NIFS) on January 10-11, 2023. This symposium was attended by 35 researchers and students from universities, institute, and industrial companies. At the symposium, 18 research papers were presented each of them was followed by fruitful discussions. This symposium has provided an excellent environment for information exchange between the researchers and has promoted collaborations between NIFS and universities.

I would like to express my sincere thanks to all of the symposium attendees, all of the paper authors, and the staffs of National Institute for Fusion Science.

Koichi Takaki
Iwate University

Tetsuo Ozaki
National Institute for Fusion Science

NIFS 2022 Coordinated Research (Symposium)
Project Title: Recent trends in technologies of pulse power, high-density plasma and particle beams
Project ID: NIFS22KIGH003
NIFS Contact Person: Dr. Tetsuo Ozaki

List of participants

T. Kikuchi *(Nagaoka University of Technology*)
Z. Lin *(Nagaoka University of Technology*)
T. Kazuma *(Nagaoka University of Technology*)
H. Ito (*University of Toyama*)
T. Takezaki (*University of Toyama*)
Y. Fukada (*University of Toyama*)
K. Tanaka (*University of Toyama*)
A. Yamamoto (*University of Toyama*)
T. Koguchi (*University of Toyama*)
T. Matsuzawa (*University of Toyama*)
Y. Ohmura (*University of Toyama*)
A. Fujino (*University of Toyama*)
T. Matsui (*University of Toyama*)
H. Matsuyama (*University of Toyama*)
J. Miyamoto (*University of Toyama*)
W. Jiang *(Nagaoka University of Technology*)
T. Sugai *(Nagaoka University of Technology*)
S. Inoue *(Nagaoka University of Technology*)
N. Terashima *(Nagaoka University of Technology*)
H. Katayori *(Nagaoka University of Technology*)
S. Tokutake *(Nagaoka University of Technology*)
S. Li *(Nagaoka University of Technology*)
A. Tokuchi (Pulsed Power Japan Lab.)
N. Ikoma (Pulsed Power Japan Lab.)
K. Nakata (Pulsed Power Japan Lab.)
G. Imada (*Department of Information & Electronics Engineering, Niigata Institute of Technology*)
T. Kawamura (*Tokyo Institute of Technology*)
K. Takaki (*Iwate University*)
K. Takahashi (*Iwate University*)
S. Joshita (*Iwate University*)
T. Sato (*Iwate University*)
S. Mukaigawa (*Iwate University*)
R. Akaishi (*Iwate University*)
Z. Sasaki (*Iwate University*)
D. Wang (*Kumamoto University*)
S. Katsuki (*Kumamoto University*)
T. Ozaki (*National Institute for Fusion Science*)

CONTENTS

Design and prototyping of tesla transformer for a compact pulsed electron beam accelerator

Shota Inoue, Naoki Terajima, Kosuke Nakamura,
Taichi Sugai, Akira Tokuchi, Weihua Jiang

Nagaoka University of Technology Extreme Energy Density Research Center

ABSTRACT

Need to develop pulse power supply with coreless tesla transformer that one to downsize Extreme Impulse Generation System (EIGS) small. Calculation of the coupling coefficient of the Tesla transformer and circuit simulation methods were shown, and an actual Tesla transformer designed based on these methods was created and tested. Simulation results show that energy is not fully transferred from primary to secondary due to insufficient resonance. Experiment results show that the stray inductance at the switch affects the period, boost ratio, and transfer efficiency.

Keywords

Extreme Impulse Generation System, Tesla transformer, Coupling coefficient

1. Introduction

The Extreme Impulse Generation System (EIGS) is characterized by GW-class output power, output voltage of several 100kV, and pulse width of about 100ns. Industry requires output power of 4 GW, pulse width of 100 ns, volume of 0.2 m^3, mass of 200 kg, and repetition rate of 10 Hz. Therefore, this research is aiming for miniaturization by developing a pulse power supply with a coreless Tesla transformer, ultra-compact waveform forming lines, and a multilayer radial-insulation type power feed. Here, we show the simulation method and experimental results of the coreless Tesla transformer.

2. Experimental Setup

2.1 How to calculate the coupling coefficient of a Tesla transformer

Figure 1 shows a schematic diagram of a coreless Tesla transformer. If a current is applied to the primary coil and the it is divided into n slices on a loop, the current flowing in each loop is $i = I/n$.

Consider the magnetic flux density that the primary makes in a single turn coil. The magnetic flux density created at point Q(r, z) is given by

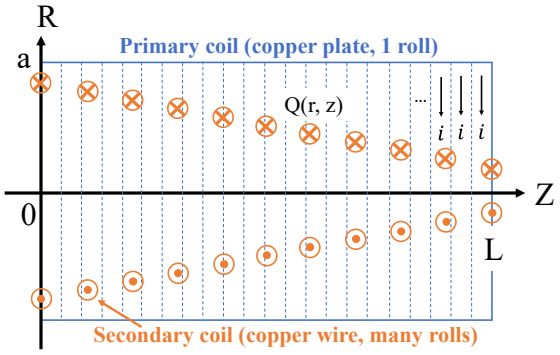

Fig. 1 Neutron production rate vs. cathode current

$$B = \frac{\mu_0 i}{4\pi}$$

$$\int_0^L \int_0^{2\pi} \frac{a - r\cos\Theta}{((z-dz)^2 + a^2 + r^2 - 2ar\cos\Theta)^{\frac{3}{2}}} d\Theta dz \quad (1)$$

The magnetic flux created by the current flowing in the primary side in a coil of radius r centered at (0,z) is the product of flux density and area and can be expressed as

$$\varphi = Br^2\pi \text{ [Wb]} \quad (2)$$

Since the secondary of a Tesla transformer has many turns, the magnetic flux created in each coil is calculated and the average value is calculated. This is the magnetic flux φ_2 that passes through the secondary out of the magnetic flux generated on the primary side. Here, if the magnetic flux generated on the primary side is φ_1, the coupling coefficient k is the ratio of the amount of flux that passes through the secondary side of the magnetic flux generated on the primary side, and can be expressed as

$$k = \frac{\varphi_2}{\varphi_1} \quad (3)$$

A coupling coefficient of $k = 0.6$ is recommended, in which case the maximum induced maximum induced electromotive force occurs at the second peak. [1]

2.1 How to simulate the circuit

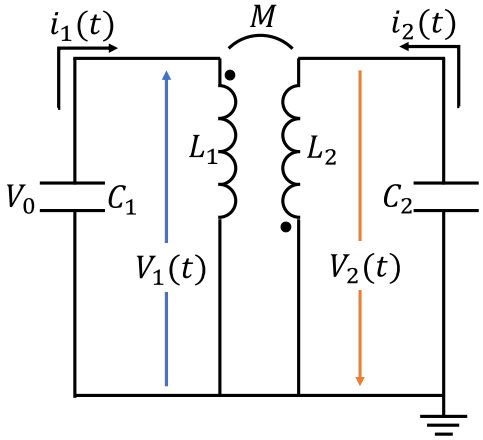

Fig.2 Circuit diagram of Tesla transformer

Figure 2 shows the equivalent circuit of a tesla transformer. The circuit equation of the equivalent circuit is shown as

$$V_1(t) = -L_1\frac{di_1}{dt} - M\frac{di_2(t)}{dt} \quad (4)$$

$$V_2(t) = M\frac{di_1(t)}{dt} + L_2\frac{di_2(t)}{dt} \quad (5)$$

The magnetic flux passing through the secondary due to the primary current φ_2 and applying the number of secondary windings *N*, Equation (5) becomes

$$V_2(t) = N\frac{d\varphi_2}{dt} + L_2\frac{di_2(t)}{dt} \quad (6)$$

Simulate the circuit by solving Equation (4) and Equation (6).

3. Simulation and Experimental result

3.1 Simulation result

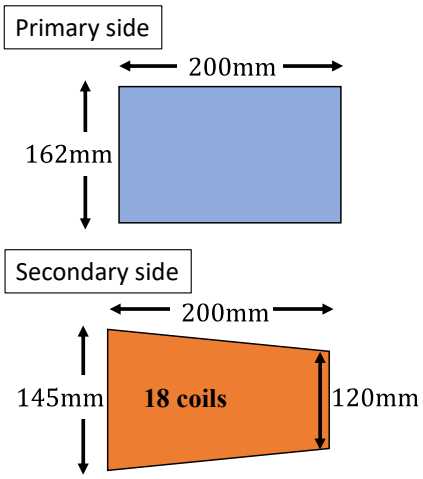

Fig.3 Dimensions of simulation conditions

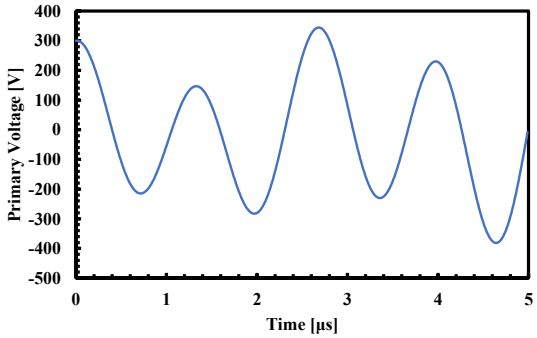

Fig.4(a) Primary voltage (simulation)

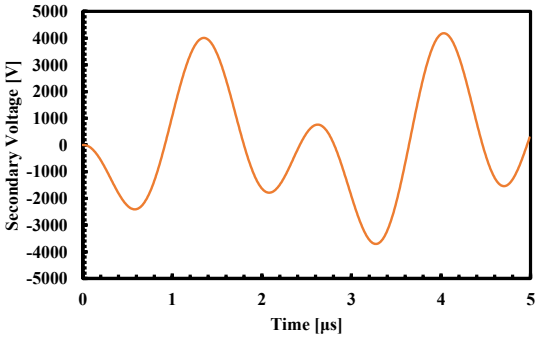

Fig.4(b) Secondary voltage (simulation)

Simulations were performed using the methods in Chapter 2 with the dimensions shown in Figure 3. Under the conditions shown in Figure 3, the coupling

coefficient $k = 0.618$, the primary inductance $L_1 = 94.9$ [nH], and the secondary inductance $L_2 = 30.7$ [μH]. If the primary capacitance $C_1 = 1.0$ [μF], the secondary capacitance $C_2 = 5.2$ [nF], and the voltage to charge the primary capacitor $V_0 = 300$ [V], the waveforms shown in Figure 4(a) and (b) were output.

The voltage at the second peak in Figure 4(b) was about 4 [kV] for a charging voltage $V_0 = 300$ [V]. This means that the voltage boost ratio in the simulation was 13.3 times.

3.2 Experimental result

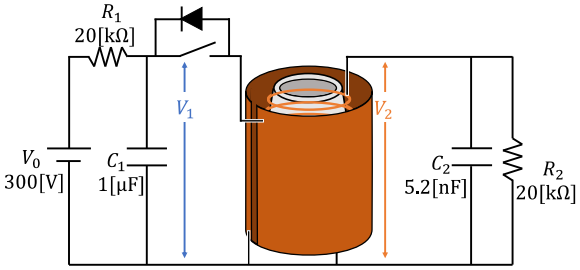

Fig.5 Experimental device

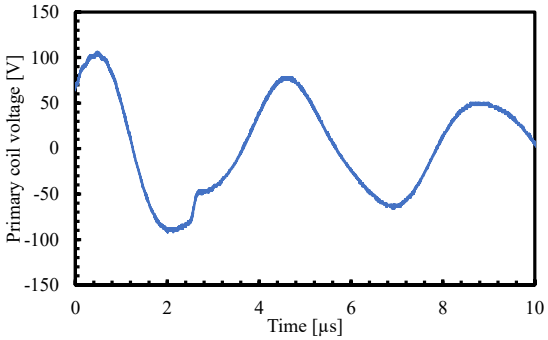

Fig.6(a) Primary coil voltage (experimental)

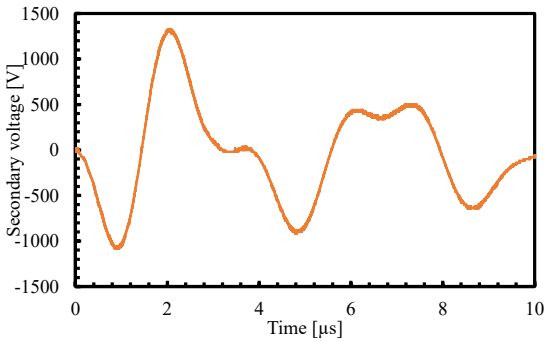

Fig.6(b) Secondary coil voltage (experimental)

Figure 5 shows the experimental setup. The dimensions of the Tesla transformer, primary and secondary capacitance, and charging voltage were the same as in the simulation. Thyristors were connected to the coil in 2 series and 2 parallel. R_1 was to prevent the charging voltage from flowing to the power supply, and R_2 was to consume the energy that flows to the secondary side without returning it to the primary side.

Figure 6(a) and Figure 6(b) show the primary and secondary voltages of the experiment, respectively. The maximum voltage of the primary coil was 106 [V] while the voltage at the second peak of the secondary coil was 1320 [V]. In other words, the step-up ratio of the transformer was 12.5 times.

From the experimental results, only about one-third of the input voltage was applied to the coil. The voltage boost ratio was lower than in the simulation.

4. Discussion of simulation and experimental results

4.1 Discussion of simulation result

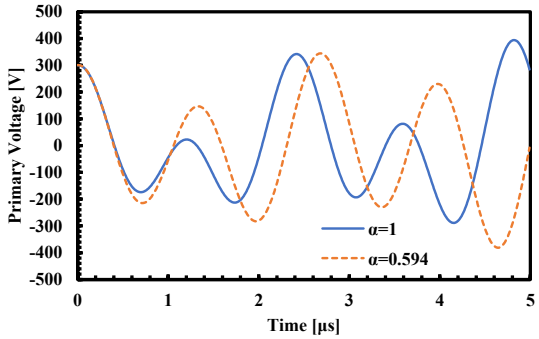

Fig.7(a) Primary voltage (turning ratio change)

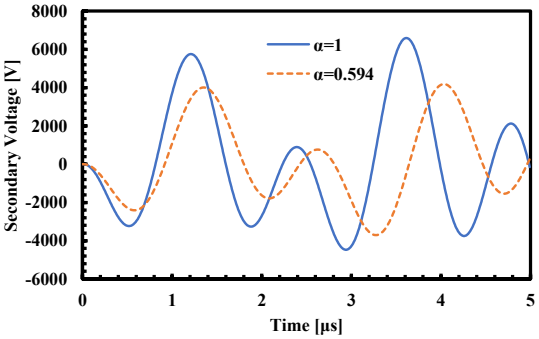

Fig.7(b) Secondary voltage (turning ratio change)

The output performance of a Tesla transformer was affected by the tuning ratio, which was the degree of detuning that indicates the resonance state. When the

tuning ratio $\alpha = 1$, the circuit was resonant and therefor energy efficient.[1] The detuning ratio α could be expressed as

$$\alpha = \frac{L_1 C_1}{L_2 C_2} \tag{7}$$

In this simulation, $\alpha = 0.594$. If the values of L_1, L_2, and C_1 are fixed, the tuning ratio $\alpha = 1$ when $C_2 = 3.09$ [nF]. Comparison of simulation results when $\alpha = 1$ and when $\alpha = 0.594$ is shown in Fig. 7(a) and Fig. 7(b). At $\alpha = 1$, the primary voltage is 0 [V] when the second peak of the secondary voltage is 6 [kV].At $\alpha = 1$, the primary voltage is 150 [V] when the second peak of the secondary voltage is 4 [kV]. For $\alpha = 1$, the energy is completely transferred from the primary to the secondary at the second peak of the secondary, whereas for $\alpha = 0.594$, the energy remains in the primary at the second peak of the secondary. The two waveforms also have different periods due to the change in the value of C_2.

4.2 Discussion of experimental result

Identify where the voltage charged to the capacitor was consumed. Consider that the voltage discharged from the capacitor was consumed by the switch section, the copper section connecting the capacitor and switch, and the primary coil section. Figure 8 shows the voltage of each element on the primary side. From the figure, 200 [V] of the 300 [V] voltage input to the capacitor was consumed by the switch section. This is thought to be since the output voltage of the coil and capacitor was divided by the floating inductance of the switch.

Figure 9 compares the waveforms of the capacitor with the sum of the waveforms of the switch section, the copper section connecting the switch and coil, and the coil section, and found that the voltage output from the capacitor was entirely consumed on the primary side.

The energy efficiency from primary to secondary was calculated on a time axis and shown in Figure 10. The formula for calculating energy efficiency E is expressed as

$$E = \frac{\frac{1}{2} C_2 V_2^2}{\frac{1}{2} C_1 V_0^2} \times 100 \text{ [\%]} \tag{8}$$

The graph shows that only about 10 [%] of the energy input to the primary side is transferred to the secondary side. This is thought to be since the resonance is not working well because of the low tuning ratio and that more than half of the energy is consumed at the switch.

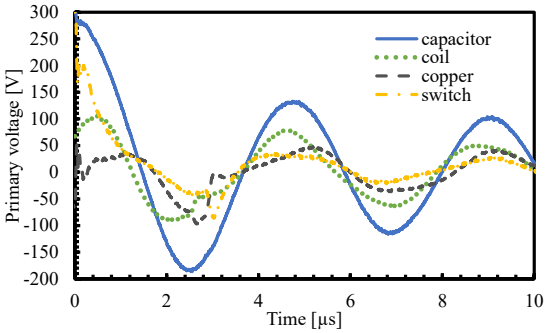

Fig.8 Voltage waveform of each element on primary side

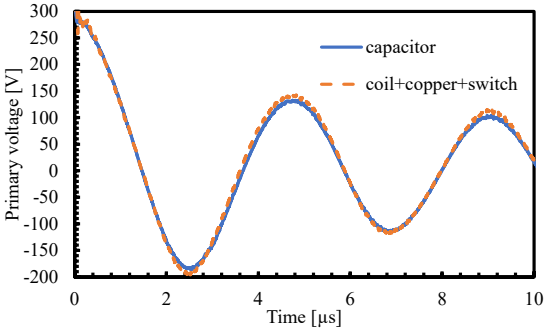

Fig.9 Comparison of primary side capacitor waveforms and other parts

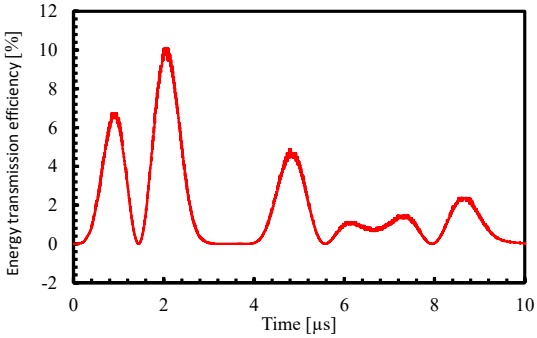

Fig.10 Energy transfer efficiency of Tesla transformer

5. Conclusion

A simulation of a tesla transformer for boosting voltage to reduce the size of EIGS was performed, and based on the simulation, experiments were conducted on the actual equipment. The boost ratio of the simulation results was 13.3 times. However, the energy efficiency was low because the tuning ratio was smaller than 1. This can be adjusted by changing the value of the capacitor. The boost ratio of the experimental results was 12.5 times. Transfer efficiency was low because of insufficient resonance and because more than half of the voltage charged to the capacitor was consumed by the switch.

In the future, we will change the capacitor so that the tuning ratio $\alpha = 1$ and conduct the experiment again. In addition, we will check the waveform change by changing the coupling coefficient and the number of turns, and improve the simulation based on these results.

References

[1] Lee Li et al., “Study on Double Resonant Performance of Air-core Spiral Tesla Transformer Applied in Repetitive Pulsed Operation”, *IEEE Transactions on Dielectrics and Electrical Insulation, 11August 2015, Volume:22, p.1916-1922.*

Design and analysis of a compact PFL for a small pulsed electron beam accelerator

N.Terajima, S.Inoue, K.Nakamura, T.Sugai, W.Jiang, A.Tokuchi*

Nagaoka University of Technology

**Pulsed Power Japan Lab.*

ABSTRACT

A bent Pulse Forming Line for downscaling high pulse power supply system, was simulated to investigate how the electric field distribution and output waveform are affected when the transmission line of the PFL is bent and a 3D model of a straight PFL and a bent PFL with the same transmission distance and a PFL folded once were designed, and simulation results of electric field distribution between inner and outer conductors and input/output delay were compared. The results of the electric field distribution showed that the distribution of the electric field changed at the uneven part of the bent PFL, but analysis of the electric field between conductors showed that breakdown was unlikely to occur. The input/output delay results showed that there was almost no change in delay time between the straight PFL and the bent PFL.

Keywords

Pulse Forming System, Transmission Line, Coaxial cable, Electromagnetic field simulation

1. Introduction

In pulsed power generators, a pulse forming line (PFL) is one way of shaping the pulse, and it has a coaxial cylindrical shape. Generally, when a pulse voltage is applied between the inner and outer conductors of a PFL, it behaves as a distributed constant circuit with a capacitor and inductor. The magnitude and phase of the output pulse wave depend on the radius of the inner and outer conductors and the length of the cylinder.

We are currently conducting research using the high-repetition pulsed power generator "ETIGO IV".[1] However, ETIGO-IV is very large, with a volume of approximately 11.6 m^3 (length 3.9 m, height 2.7 m, width 1.1 m) and a weight of 6200 kg, making it impossible to carry around.

Thus, we attempt to downscale a new pulsed power generator with a smaller volume PFL. To achieve this, we suggest a bent back transmission line to ensure that the volume of the transmission line is smaller than that of ETIGO-IV.

In this paper, three-dimensional simulation models of the straight PFL used in ETIGO-IV and the bent back PFL proposed in this power were created influence of a bent part. Simulations were conducted to verify.

2. Simulation Summary

2.1 Specified conditions

In this simulation, the electromagnetic simulation software "MAGIC" was used. In order to compare the obtained results, the geometry was unified for the two types of PFLs created as shown in Table 1. The input pulse voltage was also unified with $V_{in} = 400$ kV and pulse width t = 100 ns, and the rise time was set to 10 ns. The gap was filled with pure water (relative permittivity e = 80).

From each value set by the design, the capacitance C, inductance L, and pulse transfer rate of PFL were expressed by the following equation.[2]

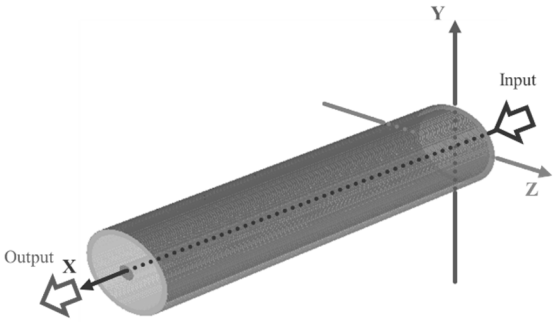

Fig 1 3D model of a straight line PFL

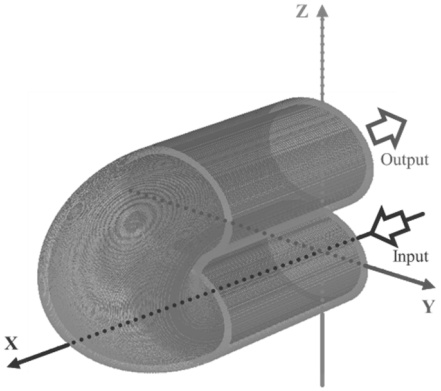

Fig 2 3D model of a folded PFL

$$C = \frac{2\pi\epsilon}{\left(\ln\left(\frac{b}{a}\right)\right)} \ [\mathrm{F/m}] \quad (1)$$

$$L = \frac{\mu}{2\pi}\ln\left(\frac{b}{a}\right) [\mathrm{H/m}] \quad (2)$$

$$v = \frac{1}{\sqrt{LC}} \ [\mathrm{m/s}] \quad (3)$$

The respective values of PFL derived from Equation (1) to Equation (3) are shown in Table 2.

2.2 Designed PFL model

The model of the designed straight PFL is shown in Fig 1 and the model of the bent PFL is shown in Fig 2. The radius and length of the inner and outer conductors are the same for both, but the bent PFL shown in Fig 2 is bent back at the half length of the transmission line.

Table 1 Shape of PFL

Inner conductor radius a [m]	Outer conductor radius b [m]	Transmission line l [m]
0.02	*0.10*	*0.93*

Table 2 Design values of PFL by calculation

Capacitor C [nF/m]	Inductance L [μH/m]	Transfer Speed v [m/s]
2.76	*31.8*	3.37×10^7

3. Simulation Results

3.1 Electric field distribution

The electric field distribution of the two PFLs for 20 ns, 50 ns, and 125 ns after applying the input pulse is shown in Fig 3 and Fig 4. The electric field distribution results are showed in the X-Y plane at Z=0 mm for the straight PFL and in the X-Z plane at Y=0 mm for the bent PFL in order to verify the change in the electric field distribution from input to output.
It is found in the both PFLs that the electric field is distributed in the gap.

3.2 Input/Output Delay

The results for input/output delay are shown in Fig. 5. The input/output delay of the straight PFL was τ_{str} = 27.7 ns and that of the bent PFL was τ_{cur} = 28,3 ns. Using the values specified in Table 2.1, the delay of the straight PFL was calculated to be τ = 27.6 ns. Compared to the simulation results, the error rate ϵ_{str} = 0.36 % for the straight PFL and ϵ_{cur} = 2.53 % for the bent PFL, indicating that the delay times are almost identical regardless of the PFL shape.

4. Discussion

Looking at the results of the electric field distribution, it appears that the input and output are almost lossless. Figs. 6 and 7 show comparison of the electric field simulation with the calculation results.

The electric field distribution between conductors in a straight PFL is

$$E = \frac{CV_{in}}{2\pi\epsilon r} \quad (4)$$

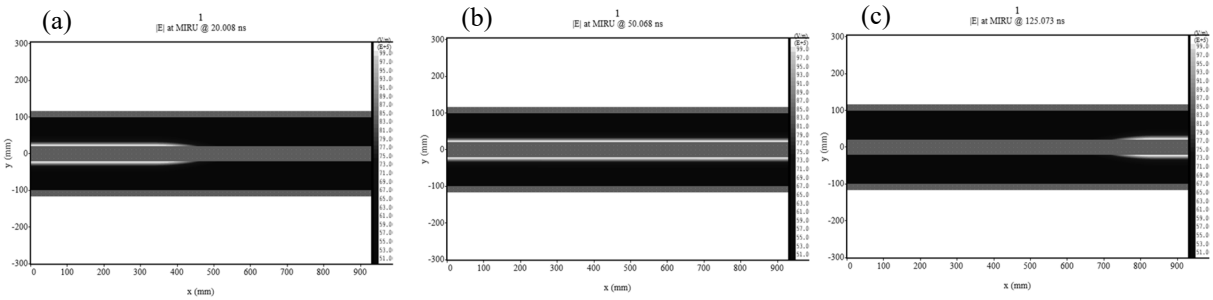

Fig 3 Electric field distribution in a straight PFL (a) t = 20 ns (b) t = 50 ns (c) t = 125 ns

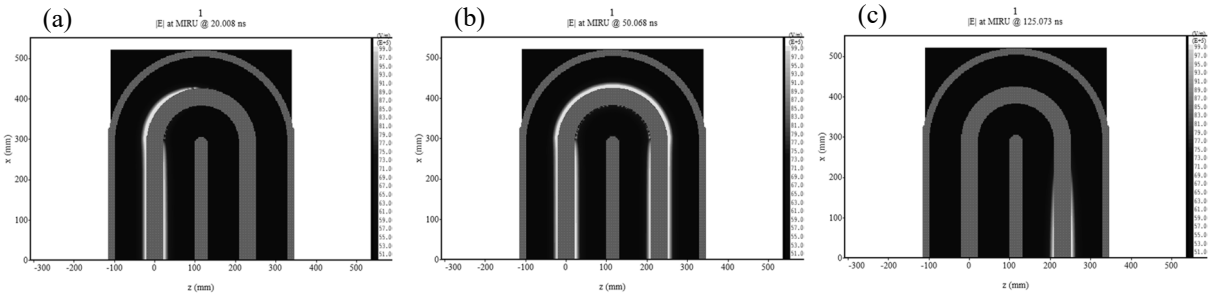

Fig 4 Electric field distribution at bent PFL (a) t = 20 ns (b) t = 50 ns (c) t = 125 ns

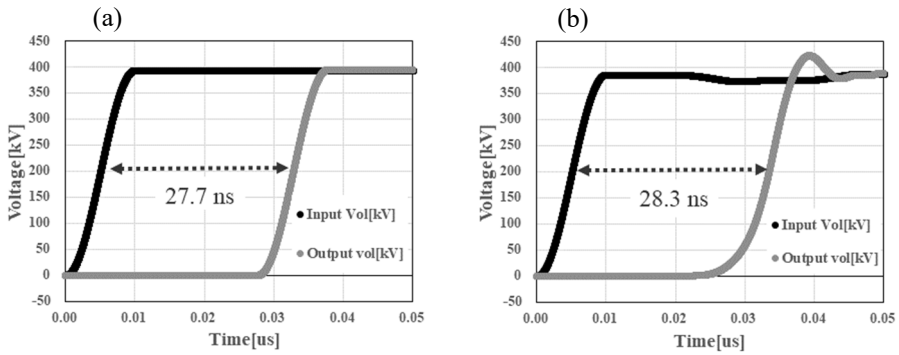

Fig 5 PFL input/output delay results (a) Straight PFL (b)Bent PFL

where the capacitance $C = 2.76$ nF/m, the input voltage $V_{in} = 400$kV, the dielectric constant $\epsilon = \epsilon_0\epsilon_s = 7.083 \times 10^{-10}$ F/m and r is the distance from center of the inner conductor center and the origin.

The darker colored areas in Fig. 6 indicate the inside of the conductor. In case of straight PFL, the simulation results are in close agreement with the calculation results.

The shape of the bent PFL differs between the inner and outer circumference of the electric field track.

Fig. 7(a) shows that the field of inner circumference at the bend portion differ significantly from the calculation results of the simple strait coaxial structure.

Especially in the part close to the outer conductor, the simulation result has a larger electric field value than the calculation result.

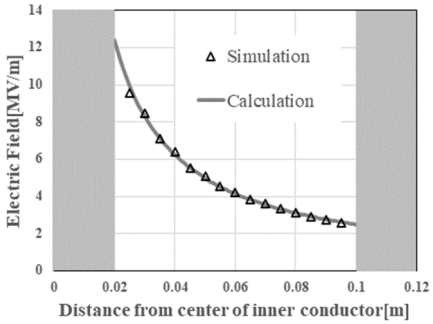

Fig 6 Comparison of electric field (Straight PFL)

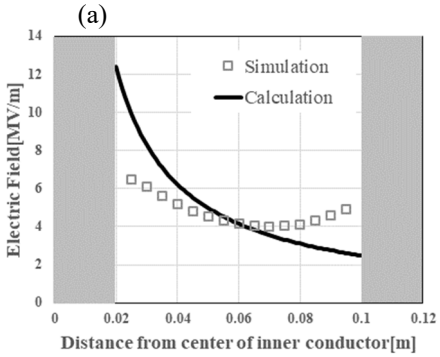

(a) The inner circumference side of the bent PFL

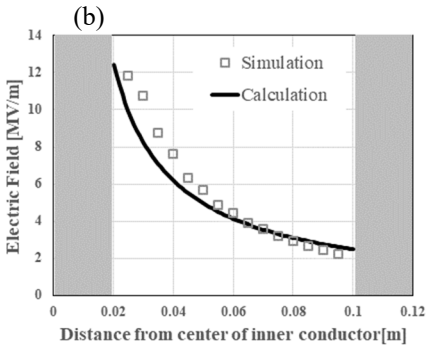

(b) The outer circumference side of the bent PFL

Fig 7 Comparison of electric field

In the outer circumference, the trend of the two results is almost identical, but in the part close to the inner conductor, the field value is larger than the calculation result of the straight structure. This is because the electric field concentrates in the convex part.

5. Conclusions and Future Prospects

Simulations of the straight PFL and the bent PFL were performed and compared with the calculation results of the simple straight structure.

As the result, it is found that the electric field increases at the convex part in the bent back part.

In the future, we would like to verify how the electric field in the bent part changes when the bending angle is changed. We will verify how the input/output delay time is affected when the number of the bent back part is increased.

References

[1] A. Tokuchi, et al. :" Repetitive pulsed-power generator "ETIGO-IV"", *IEEE Trans. Plasma Sci.*, Vol 30, No.5, pp.1637-1641(2002)

[2] Jane Lehr, Pralhad Ron, "Foundations of PULSED POWER TECHNOLOGY", *WILEY & Sons, Inc.,* pp.97-99,102-106(2017)

A Study of Charging Methods in High-Repetition Bipolar Pulse Power Generators

Hiromu Katayose,Taichi Sugai, Akira Tokuchi, Weihua Jiang

Nagaoka University of Technology

Pulsed Power Japan Laboratory Ltd.

ABSTRACT

Bipolar MARX generators have been investigated for use in discharge pumping of CO_2 gas lasers using a barrier discharge. The relationship between repetition rate and energy efficiency was calculated from a simple equivalent circuit with the aim of achieving both charge rate and energy efficiency in a high repetition rate bipolar MARX generator. In addition, charge waveforms for each circuit were obtained using LTspice, and it was confirmed that some circuit configurations are suitable for MARX generators. Based on the calculation results, a tentative circuit parameter design method was proposed.

Keywords

Pulse power, bipolar MARX, MARX charging circuit

1. Introduction

One application of pulsed power is carbon dioxide lasers using barrier discharges, which require a high-repetition rate, high-efficiency, bipolar output pulsed power supply for discharge pumping. Development of bipolar MARX generators is underway, but the challenge is to achieve both high repetition rate and high efficiency. Also in the pulsed power field, there is little discussion on the charging method and parameter determination method of bipolar MARX. In this study, we focused on the charging method using an inductor, obtained the relationship between repetition rate and efficiency, and examined the circuit configuration suitable for charging using simulation. We also aim to propose a parameter design method applicable to the design of actual equipment.

The bipolar MARX power supply has the circuit configuration shown in Fig. 1. One module consists of a capacitor(200 μF)and an inverter, and the capacitors are connected by a charging inductor. High voltage output is obtained by connecting multiple modules. The laser power supply is planned to have 8 stages with 600 V charging and 4.8 kV output. with 25-shot burst operation. The charge consumption per burst was estimated to be 3.8×10^{-4} C based on the experimental waveform with a discharged load.

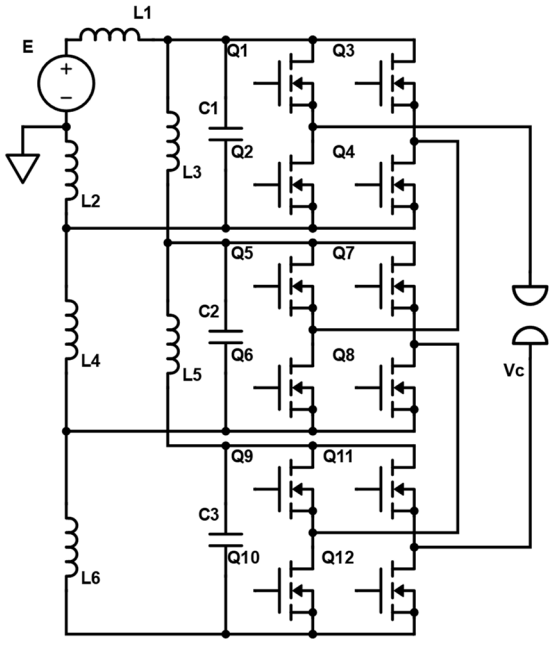

Fig.1 Bipolar Pulse Power Generators

In a typical unipolar MARX generator[1] current passes through a diode for charging, as shown in Fig. 2(a). The use of diodes enables ideal charging with high efficiency and no leakage current. On the other hand, when such diode charging is applied to a bipolar MARX generator, the circuit becomes (b) during charging. During output, the circuit becomes (c) and both ends of the capacitor are short-circuited. Therefore, the diode cannot be used and charging is done through a resistor or inductor. Resistive charging is not suitable for high efficiency because it generates losses, although the parameters are easy to set. In this study, we examined the operation when an inductor is used to achieve higher efficiency.

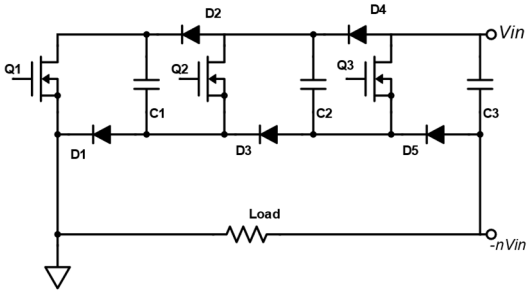

(a) Unipolar charging mode

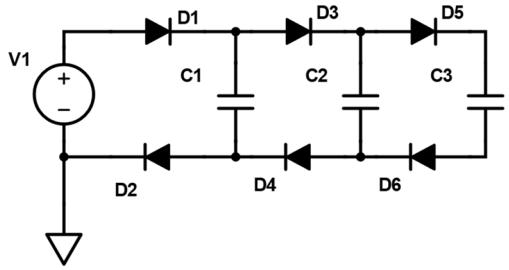

(b) Bipolar charge mode

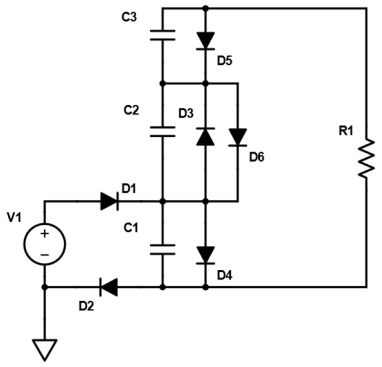

(c) Bipolar discharge Mode

Fig.2 MARX generator Charging circuit.

Consider the charging speed and efficiency in the circuit where the diode in Fig. 2(b) and (c) is replaced by an inductor. During charging, the capacitor is charged through the inductor, so a small inductance is advantageous for high-speed charging and enables high repetition. However, during discharge, charge leaks out of the capacitor, on the other hand, if the inductance is large, the leakage current is small and high efficiency is possible although repetition rate is limited. Thus, there is a trade-off between repetition rate and energy efficiency, the determination of inductance is important.

2. Experimental Setup

2.1 Charging time

Leakage charge was calculated to determine the relationship between inductance and charging rate. In the bipolar MARX, the first and final stages have one inductor as the leakage current path, while the second to n-1 stages have two inductors as the leakage current path, so a model with two inductors in parallel as shown in Fig. 3 was used. The leakage charge that travels from the 600 V DC power supply through the inductors during the on-time period, was calculated by equations (1) and (2). The on-time is assumed as 19 μs, which is obtained by multiplying the pulse period by the number of bursts. As can be seen from the calculation result in Fig. 4, the leakage charge decreases inversely proportional to the inductance.

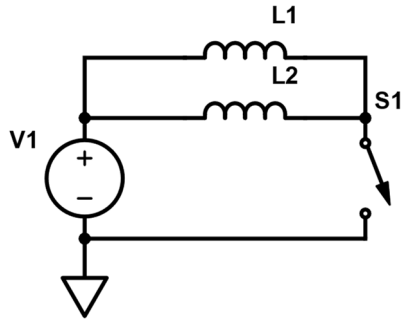

Fig.3 Leakage Current Model

$$v = L\frac{di}{dt} \tag{1}$$

$$Q = \int \mathrm{i}\,\mathrm{d}t = t_{on}^2\frac{v}{L} \tag{2}$$

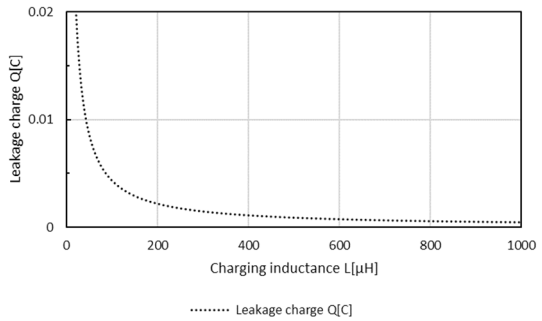

Fig. 4 Charging inductance - Leakage charge

Next, the charging time is determined. First, the initial capacitor voltage V_{c0} immediately after discharge is obtained from the calculated leakage charge and the charge consumed by the load. When inductance is $500\ \mu H$, the voltage drops to 593.7 V due to discharge from a full charge of 600 V. The charging time t can be obtained from the target charging voltage V_{C1}, initial voltage V_{C0}, and supply voltage E by solving the circuit equation from the charging circuit model in Fig. 5.

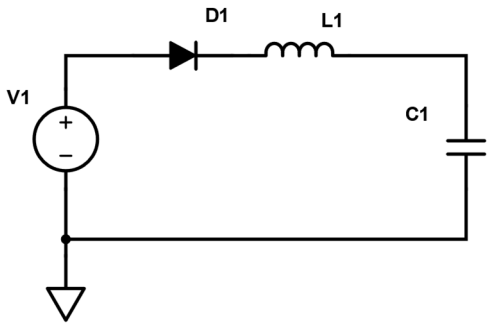

Fig. 5 Charge current model

$$V_{C0} = V_{c1} - \frac{Q}{C} \simeq 593.7V\ (L = 500\mu H) \qquad (3)$$

$$E - v_{co} = L\frac{\mathrm{di}}{\mathrm{d}t} + \frac{1}{c}\int \mathrm{i}\,\mathrm{d}t \qquad (4)$$

$$I = \frac{E - v_{c0}}{\sqrt{\frac{L}{c}}} \sin\frac{1}{\sqrt{Lc}}t \qquad (5)$$

When $t = 0$ $\quad \frac{1}{c}\int \mathrm{i}\,\mathrm{d}t = 0$

$$\frac{1}{c}\int \mathrm{i}\,\mathrm{d}t = (v_{co} - E)\cos\frac{1}{\sqrt{LC}}t + E - v_{co} \qquad (6)$$

$$V_{c1} = V_{c0} + \frac{1}{c}\int \mathrm{i}\,\mathrm{d}t\ = (V_{c0} - E)\cos\frac{t}{\sqrt{LC}} \qquad (7)$$

$$t = \sqrt{LC}\cos^{-1}\left(\frac{V_{c1} - E}{V_{c0} - E}\right) \qquad (8)$$

The charge time is defined as the time until the target voltage is reached. In this calculation, it is assumed that a diode is inserted thus, reverse current to the power supply side doesn't flow.

3. Results and Discussion

3.1 Repetition frequency and energy efficiency

Maximum repetition frequency and energy efficiency for inductance connecting to Marx circuit, is shown in Fig. 6. The energy efficiency η is defined as the ratio of load consumption to sum of load consumption $Qload$ and leakage charge $Qloss$.

$$\eta = \frac{Q_{load}}{Q_{load} + Q_{loss}}[\%] \qquad (9)$$

The maximum frequency in the region from 500 μH to 2000 μH, which is a realistic inductance, is ranged from 2 to 1 kHz, and the energy efficiency is ranged from 30 to 63%. If higher repetition rates or higher efficiencies are required, it is difficult to meet the specifications. As a method to increase the repetition rate without changing inductance, one can consider increasing supply voltage than the target voltage.

Fig. 7 shows the effect of increasing supply voltage on maximum repetition frequency. The speed is approximately 3.6 times faster at 660 V charging, which is 10 % higher than the target voltage.

It is thought that the capacitor is charged at high speed because there is a sufficient difference between the capacitor voltage and the supply voltage. Fig. 8 shows variation of charging time with an increase of

supply voltage, which is obtained by equation (8). If the power supply for charging becomes too higher than the target power supply, the advantage of the pulse power supply fades away, so voltage charging in the range from 600 to 650 V with a large slope is considered most effective.

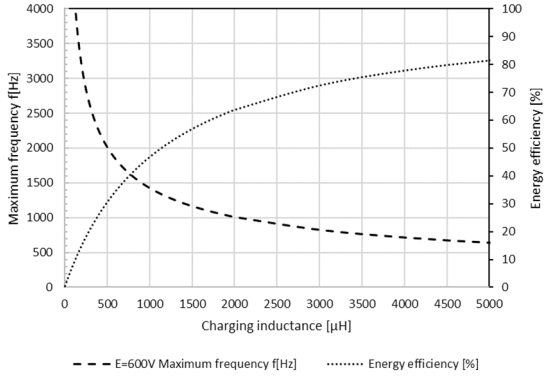

Fig.6 Maximum repetition frequency and energy efficiency

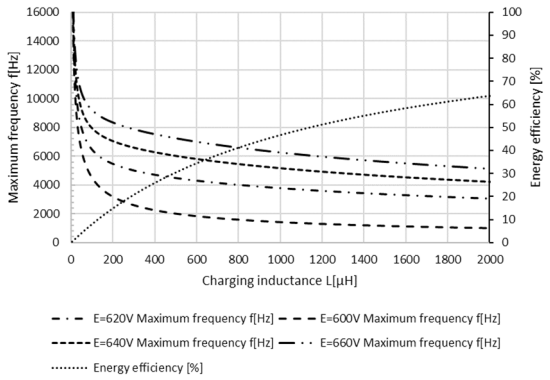

Fig.7 Maximum repetition frequency and energy efficiency (High Voltage Charging)

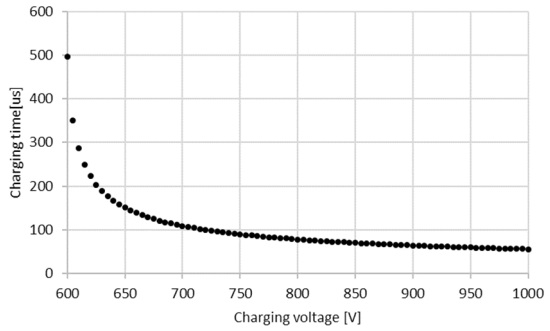

Fig.8 Charging Voltage - Charging Time

3.2 Charging circuit simulation

Actually, capacitors and inductors of Marx circuit is formed into ladder configuration such as fig.9. For the analysis of capacitor charge in the ladder configuration, charge voltage of three configurations with five stages in fig.9 was simulated. As initial condition, supply DC voltage is 600 V, and voltages of capacitors are 593.7 V. Fig.10 shows simulation results. Because of the ladder type circuit, there is a time delay of completion of each capacitor charge, and in the case of the diode in parallel, the voltage of each capacitor is almost constant until the charge of the last stage is completed. The time required for the C5 voltage to reach the target 600 V is also shorter in the parallel configuration than in the series configuration.

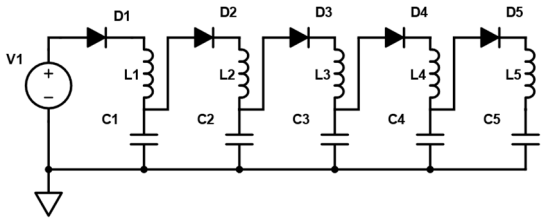

(a) Diode series configuration

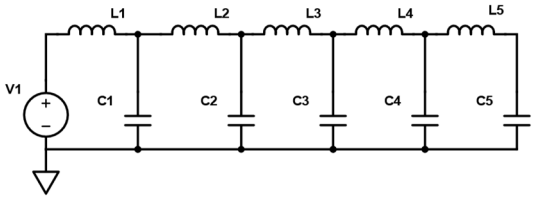

(b)Configuration without diode

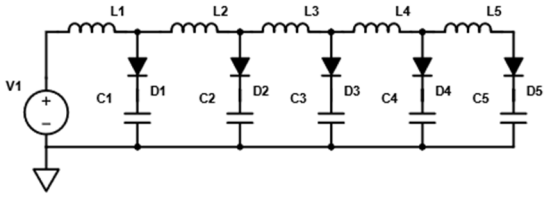

(c)Diode parallel configuration

Fig.9 Simulation circuit

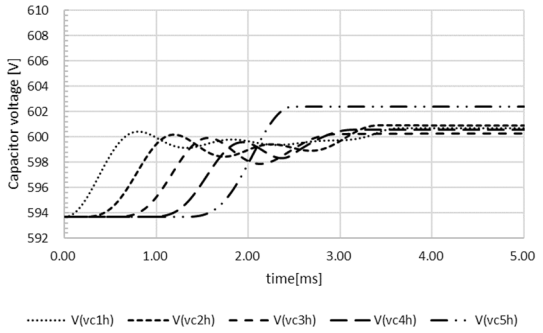

(a) Diode series configuration

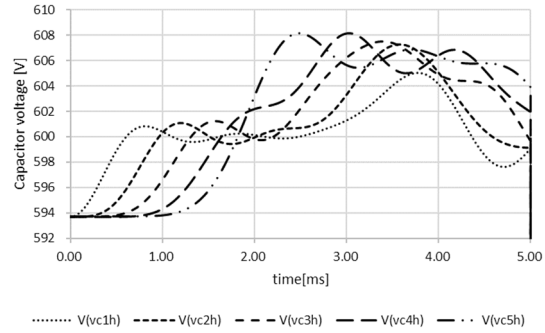

(b)Configuration without diode

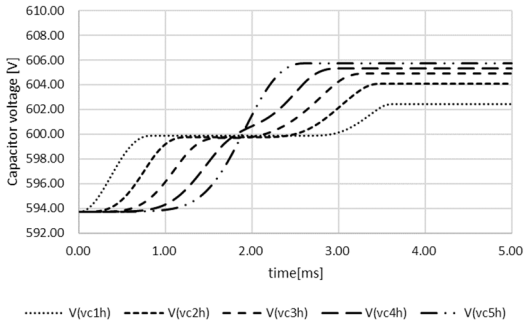

(c)Diode parallel configuration

Fig.10 Charge waveform

Fig. 11 shows the simulation results of a 660 Vcharge with a diode parallel configuration. In the case of 660 V charging, each capacitor voltage is stable at around 665 V until the charging of C5 is completed. The time until the voltage of C5 reaches 600 V is about 1.26 ms, which is shorter than the 1.89 ms of 600 V charging. However, the target voltage cannot be output because it stabilizes above the target voltage of 600 V.

Therefore, to implement high-voltage charging, it is necessary to control the voltage at each stage by incorporating another circuit such as a buck chopper circuit..

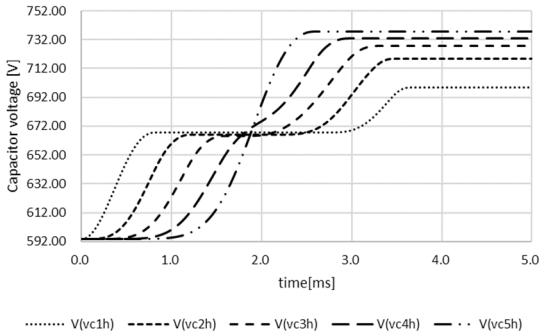

Fig.11 High-voltage charging waveform

3. 3 Selection of inductance

Finally, based on the results of the previous calculations, how to select inductance for Marx generator is summarized as follows. First, the repetition rate (frequency) is determined, and the charge consumed by the load is calculated. Next, the inverse of the repetition rate is divided by the number of stages, to obtain the charging time per stage. Finally, the inductance is determined from the graph of maximum frequency in Fig.6 and 7. Energy efficiency of the determined inductance is calculated by Equation (1),(2), and (9).

4. Conclusions

The relationship between charging time and inductance was obtained for higher repetition rate and higher efficiency of bipolar MARX. Furthermore, an improvement in charging speed was observed with high-voltage charging. Although compatibility of higher efficiency and high repetition rate can be expected by increasing the inductance with higher supply voltage, adjustment of the charge completion timing is an issue for realization. Thus, voltage control, by power switching is necessary.

References

[1] W. JIANG, K. TAKAGI et al., “The Role of Power Semiconductor Devices”, J. Plasma Fusion Res. Vol.87, No.2 (2011)106-111).

Characterization of MOS-Gated Thyristor for High Repetition Rate High Current Pulsed Power Generator

Shintarou Tokutake, Akira Tokuchi *, Taichi Sugai, and Weihua Jiang

Nagaoka University of Technology

** Pulsed-Power Laboratory Ltd.*

ABSTRACT

In order to realize a high-repetition high-current pulsed power generator, a switching device with high power capacity and high repetition capability is required. In this paper, loss and high-repetition operation of MOS-gated thyristors are investigated for use in actual circuits. Regarding losses, magnetic assist, in which a magnetic switch is inserted into the circuit to slow down the current, reduced both the thyristor losses and the overall circuit losses. Increasing the number of turns of the magnetic switch reduced the leakage current during blocking, but extended the pulse width, resulting in increased losses. Regarding high repetition rate operation, operation at 1 kHz was confirmed.

Keywords

MOS-Gated thyristor, switching loss, magnetic switch

1. Introduction

Pulsed power is a technology that compresses stored energy over time to produce a large output. One application of pulsed power is the generation of plasma in semiconductor manufacturing, such as thin film generation processes. The circuit for generating high-current glow discharge requires a high current of several ~kA and repetitive operations of several ~kHz. Therefore, switching elements used in the circuit must also have high power capacity and high repetition rate.

In this paper, we evaluated the characteristics of MOS-gated thyristors as switching elements for high-current pulse power generator.

2. Experimental Setup

2.1 MOS-gated thyristor

Thyristor is turned ON by applying voltage to the gate voltage, resulting in a conducting state. Once turned on, thyristor cannot be turned off by an external signal, and will not turn off until a reverse voltage is applied or the current falls below a threshold value. MOSFET are often used as switching devices in pulsed power generator, but thyristors are characterized by their high power capacity compared to MOSFET.

MOS-gated thyristor used in this paper is IXHX40N150V1HV made by IXYS Corp. Peak anode-cathode voltage is 1500V. Peak current are 7.6kA (1μs) and 3.5kA (10μs) [1].

2.2 Experimental circuit

Assuming use in an actual pulsed power generator, the loss was measured when a half-sine wave with a maximum current of 1kA and a pulse width of approximately 2μs was applied. Fig.1 shows a circuit used in the experiments. The primary capacitor C_1 and secondary capacitor C_2 were 1.6 μF. As the operation process, C_1 is charged initially. Then, when the thyristor turned on, C_1 is discharged and C_2 is charged. The voltage and current of the thyristor during this operation were measured and the loss was calculated.

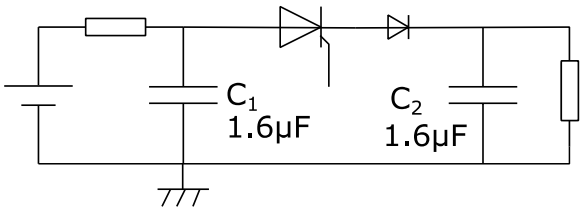

Fig.1 Experimental circuit schematic

3. Results and Discussion

3.1 Loss of thyristor

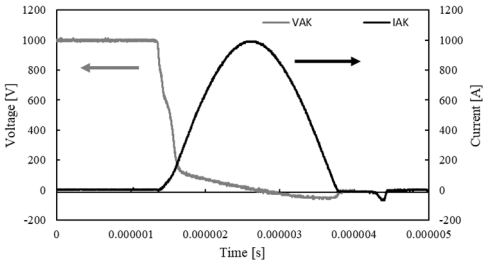

Fig.2 Thyristor voltage and current

Fig.2 shows waveform of thyristor voltage and current. The pulse width was 2.4 μs and the maximum current was 1 kA. The loss calculated from equation (1) was 31 mJ.

$$\int V_{AK} \times I_{AK}\, dt = 33mJ \qquad (1)$$

Regarding turn-on, ideally the voltage would immediately drop, but in reality the voltage did not drop immediately, and the loss was caused during the transition of voltage and current. One way to improve this loss at turn-on is magnetic assist[2].

3.2 Magnetic assist

Magnetic assist means inserting a magnetic switch into the circuit and blocking the current until the magnetic switch saturates, delaying the flow of current. In operation, immediately after the thyristor is turned on, the magnetic switch blocks current because the magnetic switch is not saturated. After the magnetic switch saturates, current flows to the thyristor. This allows current to flow after the thyristor voltage drops, thus reducing losses during turn-on. Fig.3 is an image of a magnetic switch.

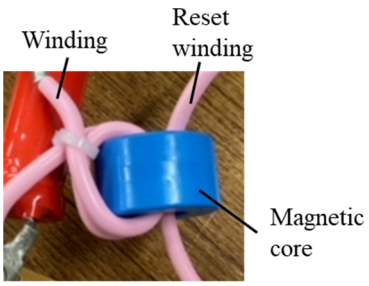

Fig.3 Magnetic switch

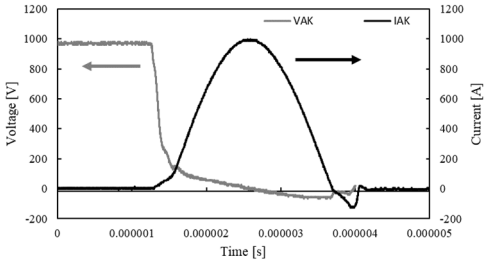

Fig.4 One turn

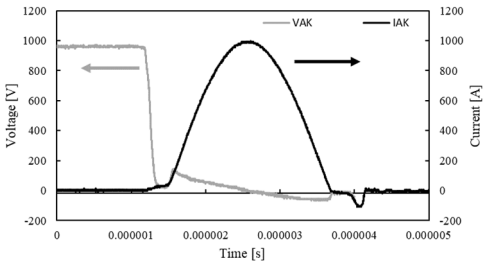

Fig.5 Two turns

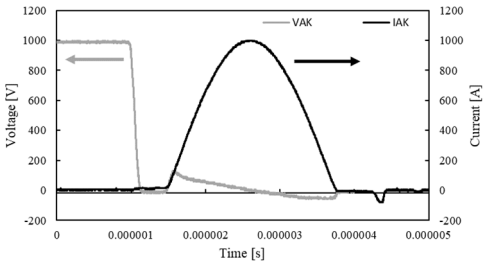

Fig.6 Three turns

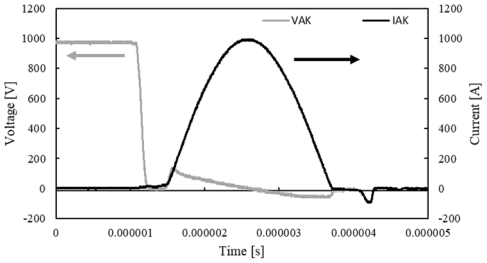

Fig.7 Four turns

Fig.4~Fig.7 show waveforms at each number of turns of the magnetic switch.

When the turn is one, the current is not blocked until the voltage falls since the core saturation time is too short.

When the turn is more than two, it can be confirmed that the current is blocked until the voltage drops. The delay time of the current after the voltage drops increased with an increase of number of turns. While current blocking, a little leak current was confirmed, which decreases with an increase of number of turns.

3.3 Variation of loss due to winding and reset current

The Table.1 shows the thyristor losses for each magnetic switch winding and reset current. This table shows that the loss of the thyristor in the no assist case was 31 mJ, while the loss was reduced to a minimum of 12 mJ. In the case of one turn, the loss was reduced compared to the unassisted case, but the loss was higher than in the case of two to four turs, indicating that the turns of the magnetic switch was not enough. The increase in loss in the case of four turns compared to the case of two to three turns can be attributed to the increase in inductance of the magnetic switch due to the increased number of windings. Fig.8 shows the current waveforms of the thyristor with two to four turns. This waveform shows that the pulse width increases as the number of turns is increased. This suggests that increasing the number of turns of the magnetic switch decreases the leakage current, but increases the pulse width, leading to an increase in loss.

The Table.2 summarizes the overall circuit loss for each number of switch winding and reset current. It can be seen that the loss without magnetic assist is 83.1 mJ, and that the loss is reduced compared to the case without magnetic assist when two to four turns are used. This indicates that the addition of magnetic assist to the circuit decreases the overall circuit loss.

Table 1 Loss of thyristor

	Winding [turn]				No assist
Reset current [A]	1	2	3	4	
4.8	19.2	12.1	12.5	15.4	31.0
9.6	17.9	12.0	12.5	14.6	
14.4	17.0	12.6	12.7	13.0	

Table 2 Loss of circuit

	Winding [turn]				No assist
Reset current [A]	1	2	3	4	
4.8	84.8	67.7	63.1	69.4	83.1
9.6	85.1	66.0	63.7	69.2	
14.4	81.0	66.8	62.7	64.8	

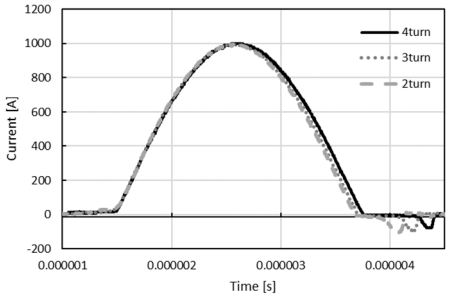

Fig.8 Variation of current with turns

3.4 About continuous operation

Fig.9 and Fig.10 show the voltage and current waveforms of the thyristor when operated at 100 Hz and 1 kHz, respectively. The operation at 1kHz repetition was same as at 100Hz.

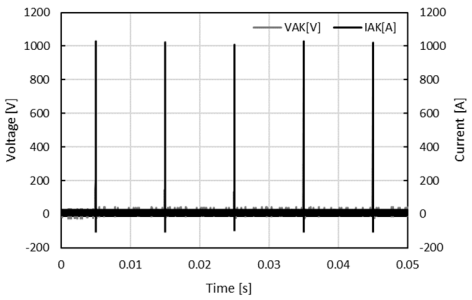

Fig.9 100Hz operation

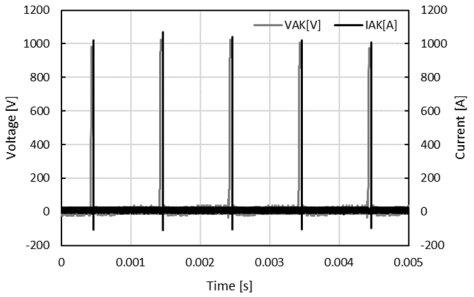

Fig.10 1kHz operation

4. Conclusions

Losses in MOS-gated thyristor were evaluated at 1 kA and 2.4 μs half-sine wave current. By using magnetic assist to allow the current to flow after the voltage on the thyristor had fallen, the thyristor loss and the overall circuit loss could be reduced. Thyristor losses were reduced from 30 mJ to a minimum of 12 mJ.

Regarding the high repetition rate operation, it was found that a repetition rate of 1 kHz was possible.

References

[1] 1500V MOS-Gated Thyristor IXHX40N150V1HV, IXYS, Milpitas, CA, USA, 2014

[2] J. Perez, T. Sugai, A. Tokuchi and W. Jiang, "Marx Generators Based on MOS-Gated Switches With Magnetic Assist for Accelerator Applications", IEEE Trans. Plasma Sci., VOL. 46, NO. 6, pp.2114-2119, JUNE. 2018.

Pulsed Power Generation Using Cumulative Pulse Circuit

Shizhen Li, Taichi Sugai, Akira Tokuchi, Weihua Jiang

Nagaoka University of Technology

Kamitomioka1603-1, Nagaoka Niigata 940-2188, Japan

ABSTRACT

Pulse accumulation is to cumulate the output of multiple independent modules in the pulsed power generator to obtain a higher output voltage or output current. A direct result of pulse accumulation is therefore a multiplier effect in output power. In recent years, with the development of pulse accumulation technology, there have been new changes in the accumulation pulse circuit in pulsed power technology. It not only includes the power synthesis brought by synchronous accumulation, but also reduces the requirements for switches, and the circuit output voltage is far greater than the maximum safe voltage of switches.

Keywords

Blumlein generator, cumulative pulse, voltage adding, PFL, pulsed power, high voltage, short pulse

1. Introduction

From the point of view of pulsed power technology, the significance of pulse accumulation mainly includes two aspects: on the one hand, it can obtain output power that cannot be realized by a single pulsed power generator. The cumulative output of multiple modules can greatly exceed the working capacity of a single module; Another significance of pulse superposition is that the pulsed power generator can be modularized, that is, multiple modules are used to assemble a pulsed power generator. Modularization is beneficial to the operation and maintenance of the pulsed power generator, and also helps to reduce its cost. Standardization and mass production of commercial pulsed power generators are more important in the future[1].

2. Experimental Setup

2.1 Principle

A scheme for voltage multiplication studied in this research is the cumulative pulse line shown in Fig.1. Similarly to the generalised Blumlein line[3], it can produce a multiplication of the initial charging voltage. An advantage compared with the latter is that it needs just one switch. A cumulative pulse line consists of n interconnected transmission line elements of equal transit time. Relative to the first line element, the impedance of the successive elements grows like the sums of the natural numbers: 1+2=3, 1+2+3=6, 1+2+3+4=10,etc. The last (nth) section has an impedance $Zn=n(n+1)Z_1/2$, where Z_1 is the impedance of the first element. After the switch *SW1* is closed, a discharge wave propagates to the load end of the line. If the line is open, this wave creates a voltage $-nU_0$ at the terminals. If the line is connected to a load of impedance Zn at the time of arrival of the wave, the wave produces a pulse of amplitude $-nU_0/2$ for a duration of 2τ. where τ is the transit time for a line element. [2].

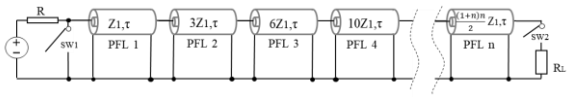

Fig.1 Cumulative pulse line with stepwise-increasing impedance

In this case, the stored energy is completely transferred to the load. The output switch *SW2* which is necessary in the series configuration, but the difficulty synchronisation between the switches *SW1* and *SW2* can be avoided if the output line is combined with a Blumlein configuration as shown in Fig.2.

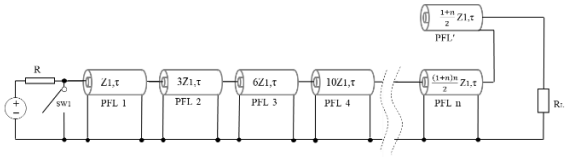

Fig.2 Cumulative pulse line combined with Blumlein configuration

The impedance of the additional line is chosen such that it delivers the same current into a matched load as does the cumulative line, i.e., and hence $Z' = \frac{n+1}{2} Z_1$. The load impedance must then be matched to the sum of Z_n and Z': $R_L = Z_n + Z' = \frac{(n+1)^2}{2} Z_1$.

2.2 Purpose

Use a capacitor and an inductance to form an LC module to replace the PFL in the principle circuit to achieve pulse superposition.

2.3 Simulation

Fig. 3 shows simulation result of cumulative pulse line shown in Fig. 2. The peak of rectangular pulse increases step by step. In this study, the PFL is replaced to a capacitor and an inductor. Table 1 shows Impedance, capacitance and inductance of each stage. Fig. 4 shows simulation results of the cumulative pulse circuit of the LC module. As with the PFL, the peak of pulse increases step by step although waveforms is similar to LC oscillation.

Table 1 Impedance, capacitance and inductance

Stage	1	2	3	4	5	6
Impedance(Ω)	10	30	60	100	150	30
capacitance(nF)	5	1.66	0.83	0.5	0.33	1.66
Inductance(μH)	0.5	1.5	3	5	7.5	1.5
Resistance(Ω)	—	—	—	—	—	180

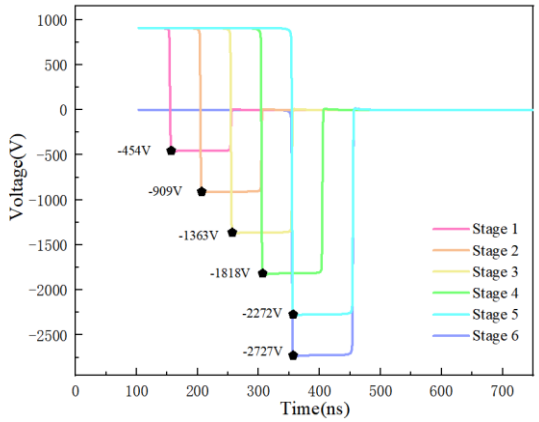

Fig.3 The voltage waveforms at each stage of PFL when the input voltage is 1000V

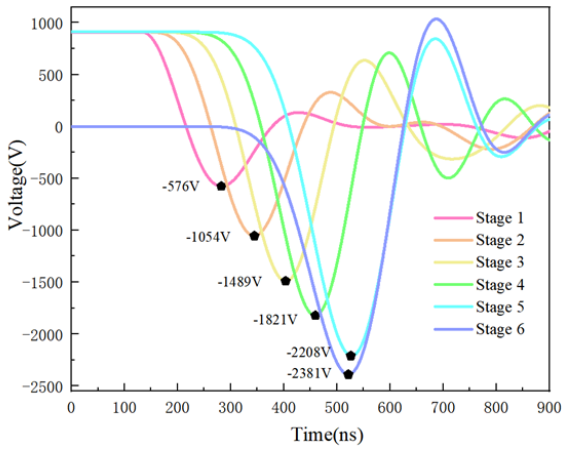

Fig.4 The voltage waveforms at the switch and each stage of LC module when the input voltage is 1000V

2.4 Actually designed

The cumulative pulse circuit based on LC module is shown in Fig.5. It consists of basic circuits of inductance, capacitor, and resistance. The specifications and quantities of the main components are shown in Table 2.

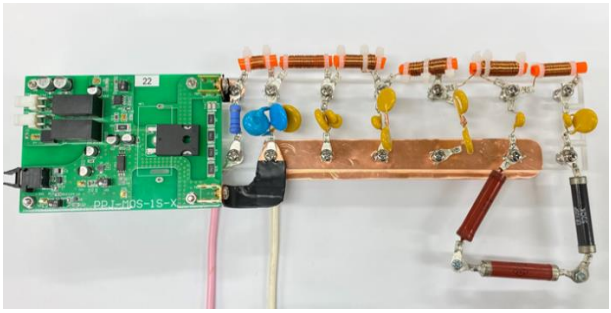

Fig.5 Experimental circuit

Table 2 Specification and quantity of major components

device	manufacture	model	specification	number
capacitor	Vishay	F331K33S3NR63K7R F102K53S3NR63K7R 564R30GASS10	3kV	n n n
resistance	TKK	ER20AS(37Ωk) ER10SP(100Ωk)	20W,30kV/50μs 10w,1kV/50μs	n n
diode	Vishay	UF5408	1 kV,3 A(DC)	1
DC/DC	Murata	MEJ2S1205SC MGJ2D121515SC	12V 12V	1 1
MOSFET	ROHM	SCT3022KL	1.2kV,95A	1

As operation procedure, initially, capacitors are charged to 1000V,then the switch (MOSFET) is turned.

3. Results and Discussion

The voltage value at the switch and each stage of LC circuit are shown in the Fig.6 and 7. At the switch, the measured current was 97.3A.

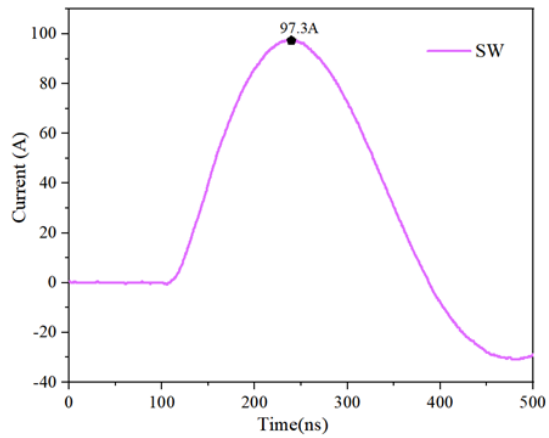

Fig.6 The current waveform at the switch

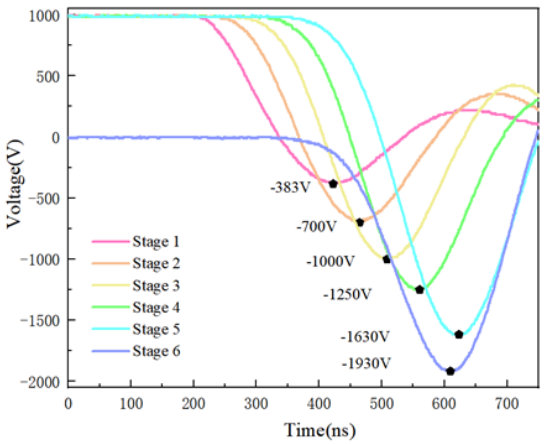

Fig.7 The voltage waveforms at the switch and each stage of LC module

Similar to the simulation results, voltage increased step by step. The requirements for the switch are low, and the circuit output voltage is far greater than the maximum safety voltage of the switch.

The output voltage of the experiment is smaller than that of the simulation because there are many stray parameters in the circuit.

4. Conclusions

Pulse accumulation plays an important role in ultra-large pulsed power generators because it can overcome the physical limitations of a single pulsed power generator. At the same time, it has low requirements for the switch, and the circuit output voltage is far greater than the maximum safe voltage of the switch. Modular cumulative pulses greatly improve the flexibility, compactness and ease of maintenance of pulsed power generators. The technical thought of the accumulative pulse circuit can be seen as decomposing the pulsed power generator into the most basic circuit unit according to the logic of pulse accumulation, so that it can save the step of pulse compression.

It can be applied in many industrial and academic fields, such as gas and liquid handling, dielectric barrier discharge and high voltage pulsed electric field sterilization.

References

[1] Jiang Weihua. High repeated frequency pulsed power technology and its application:(5) The meaning of pulse superposition[J]. High Power Laser and Particle Beams,2013,25(08):1877-1882.

[2] H. Bluhm, Pulsed Power Systems Principles and Applications, Berlin:Springer, 2006.

[3] Zhuang Longyu,Yang Junxiang, Sugai Taichi, Tokuchi Akira, Jiang Weihua. Solid-State Pulsed Power Generator Based on Blumlein PFN Using Saturable Pulse Transformer[J]. IEEE TRANS-ACTIONS ON PLASMA SCIENCE, 2021,49(10).

Evaluation of spatial distribution of soil oxidation using high voltage pulsed discharge

Suguru Joshita, Akira Harimaya, Katsuyuki Takahashi*, Koichi Takaki*, and Kohei Obase**

Faculty of Science and Engineering, Iwate University

**Agri-Innovation Center, Iwate University*

***J&T Kankyo Co., Ltd.*

ABSTRACT

The spatial distribution of soil oxidation using a high-voltage pulse generator was evaluated using indigo carmine. The results showed that the amount of indigo carmine decolorization increased with increasing charging voltage and energy input. It was also found that the decolorization of indigo carmine occurred on the surface of the needle electrode, in the discharge path, and near the ground electrode. The probability of discharge penetrating into the soil increased with decreasing the gap length between the electrode tip and soil surface, which promoted the decolorization reactions. The amount of indigo carmine decolorization per volume decreased with increasing soil depth. When the soil depth was large, discharges reaching the ground electrode could not be confirmed. This suggests that the oxidation reaction of indigo carmine depends on a discharge that penetrates the soil.

Keywords

Pulse discharge, Soil treatment, Radical

1. Introduction

The cultivation of the same crop on the same land for consecutive years is called continuous cropping. The intensive cultivation of crops with high commercial value through continuous cropping has led to the intensification of institutional farming operations. This method has the disadvantage that continuous cropping failure occurs, and the yield decreases due to poor growth of the crop. One of the causes is the increase of soil bacteria diseases [1]. Methyl bromide had been widely used as a soil fumigant because of its usability and low cost [2]. However, since methyl bromide was classified as an ozone-depleting substance, its use has been banned internationally since 2005 [3]. Therefore, the development of alternative technologies to methyl bromide has been required. Alternative techniques include soil disinfection with other chemicals such as chloropicrin and physical soil disinfection using solar heat or hot water [4]. However, soil disinfection with chemicals has problems such as the impact on workers and surrounding organisms, and soil contamination by decomposition products [5]. In addition, soil disinfection using solar heat and steam has problems such as unstable control effects depending on the weather and impractical in terms of labor and cost [6]. Soil disinfection using high-voltage pulsed power has been considered as a new method of soil treatment. High-voltage pulse power enables the generation of a variety of active species, which show an important role in the bactericidal effect on microorganisms [7]. Currently, bactericidal activity in water and air has been reported [8], and it is attracting attention as a promising technology for bacterial inactivation. However, few studies have evaluated the oxidation capacity of soil contaminated with soil-borne

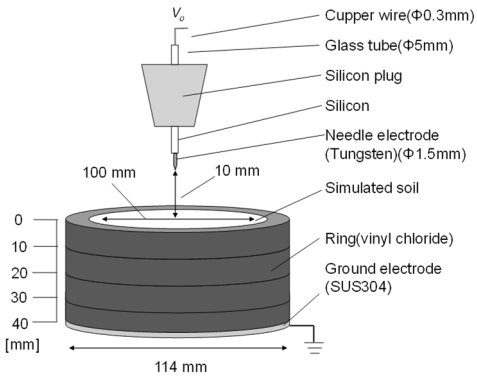

Fig. 1 Schematic diagram of discharge reactor

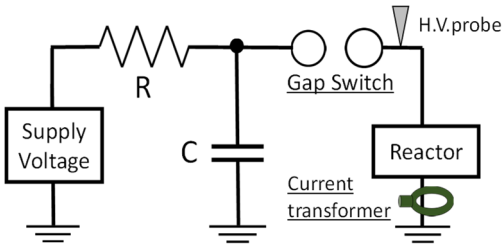

Fig. 2 RC discharge circuit diagram

pathogens by directly applying high-voltage pulses. In this study, the spatial distribution of soil oxidation by discharge treatment using simulated soil was investigated. Since the sterilization process is performed by the oxidizing reactions by active species generated by high-voltage pulses, the oxidation ability of the discharge treatment was evaluated using indigo carmine a common blue color dye which is also decolorized by the oxidizing action of active species.

2. Experimental Setup

2.1 Discharge treatment

Figure 1 shows a schematic diagram of the discharge reactor. Four rings (vinyl chloride tubes) with an outer diameter of 114 mm, an inner diameter of 100 mm, and a height of 10 mm were stacked in the reactor. The high-voltage electrode was a tungsten needle with a diameter of 1.5 mm. A stainless steel disk with a diameter of 114 mm was placed at the bottom of the reactor as a ground electrode. The simulated soil was spread over the ground electrode. Figure 2 shows the circuit diagram of the RC discharge circuit. This circuit consists of a regulated power supply (PEEC HDV-50K 12sk) to store energy in capacitor. After that, a high voltage pulse is applied to the reactor through the gap switch when a certain amount of energy is accumulated. The charging resistance was 10 MΩ and the capacitor was 270 pF. The pulse repetition rate was 120 pps, the distance between the high-voltage needle electrode and the soil surface was varied from 1 to10 mm, and the soil depth was varied from 20 to 60 mm by changing the number of rings used.

2.2 Simulated soil preparation method

Glass beads (UB-120, Akiyama Sangyo Co., Ltd.) were used as simulated soil. Glass beads were selected because they are white and the distribution of decolorization is easy to see. The evaluation sample was prepared by mixing 10 g of glass beads with 1 mL of indigo carmine solution to prepare a soil simulation. The moisture content is 9.1 %. The evaluation sample and soil were mixed using a stainless steel bowl. One layer was defined every 10 mm from the soil surface and evaluated in the depth direction. The area was divided into sections every 10 mm from the soil center and evaluated in the radial direction. The amount of soil in one layer was 125 g, and the soil was compacted with a polyacetal rod whose outer diameter was the same as the inner diameter of the discharge reactor each time one layer of soil was laid.

2.3 Evaluation method

The oxidation ability of discharge treatment on the simulated soil was evaluated by decolorization of indigo carmine (Wako Pure Chemicals, 090-00082). Indigo carmine was used because the amount of reaction is easily estimated by measuring absorbance. The concentration of indigo carmine in the simulated soil was set at 600 mg/L. After the discharge treatment, the soil was sampled by sliding the ring of the discharge reactor one step at a time. The simulated soil inside the ring was transferred to a beaker and distilled water was added. After sampling, the simulated soil was stirred for 1 min and filtered using filter paper (ADVANTEC, No. 5A). The filtered samples were measured using a spectrophotometer (Shimadzu, UV-1850) for absorbance at 610 nm, the wavelength at which indigo carmine has maximum absorbance.

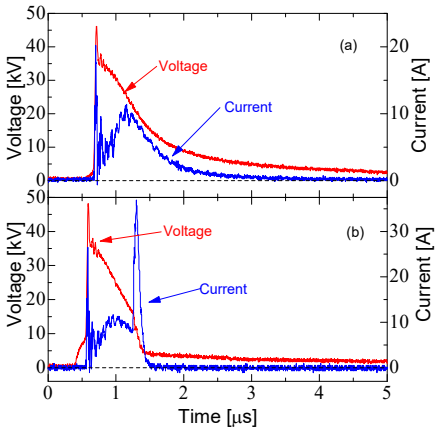

Fig. 3 Voltage and current waveforms for a charging voltage of 45 kV: (a) Waveform with exponentially decreasing current (partial discharge); (b) Waveform with rapidly rising current (total circuit breakdown).

3. Results and Discussion

3.1 Discharge characteristics

Figure 3 shows the voltage-current waveforms at a charging voltage of 45 kV. Two type voltage-current waveforms were mainly acquired in this experiment. Figure 3(a) shows a waveform in which the current decreases exponentially (partial discharge), and Figure 3(b) shows a waveform in which the current rises rapidly. After the streamer propagates from the high-voltage needle electrode and reaches the surface of the simulated soil, it propagates through the voids between the glass beads as a surface discharge. When the discharge reaches the grounded electrode in the bottom, the discharge transits to spark discharge, and the impedance decrease rapidly and the current is increase [9].

3.2 Spatial distribution of decolorization

Figure 4 shows the change in the appearance of decolorization a function of discharge treatment time. The areas where the decolorization reaction occurred remarkably were the soil surface, the soil center, and the soil near the ground electrode. On the soil surface, the decolorization reaction is thought to proceed across the entire soil surface by active species generated near the high-pressure needle electrode. At the soil center, active species are generated by the discharge plasma propagating inside the soil, and the

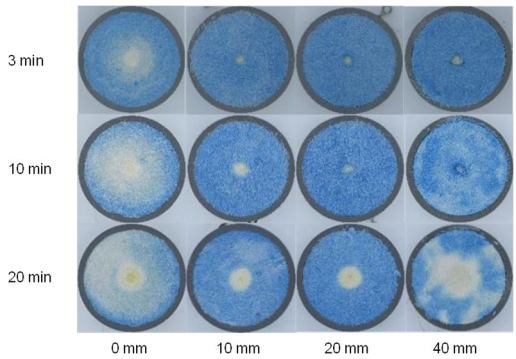

Fig. 4 Change in decolorized appearance as a function of discharge treatment time

decolorization reaction proceeds in the radial direction from the center, which is the pathway for the discharges to propagate. The decolorization rate of the soil center of all layers increased during the discharge penetration, indicating that the oxidation ability of the high-voltage pulses on the soil does not depend on the depth direction. In the soil near the grounding electrode, discharges occur at a triple junction consisting of the grounded electrode, glass beads, and air, and active species are generated, which promotes the decolorization reaction.

3.3 Influence of electrical parameters on decolorization

Figure 5 shows the distribution of decolorization rate of indigo carmine as the discharge treatment time changes. The charging voltage was set at 45 kV. Figure 6 shows that the decolorization rate increases with increasing the discharge treatment time. The longer the discharge treatment time, the greater the number of discharges that penetrate the soil, which would decolorize the soil center and the area near the ground electrode.

Figure 7 shows the indigo carmine decolorization and energy per a pulse as a function of charging voltage. The decolorization rate and energy per a pulse increased by increasing the charging voltage. The energy per discharge was 0.068 J at a charging voltage of 30 kV, 0.10 J at 35 kV, 0.21 J at 40 kV, and 0.22 J at 45 kV. The number of spark discharges observed during 100 discharges was 2 for 40 kV, and 20 for 45 kV. At charge voltages of 30 and 35 kV, where no

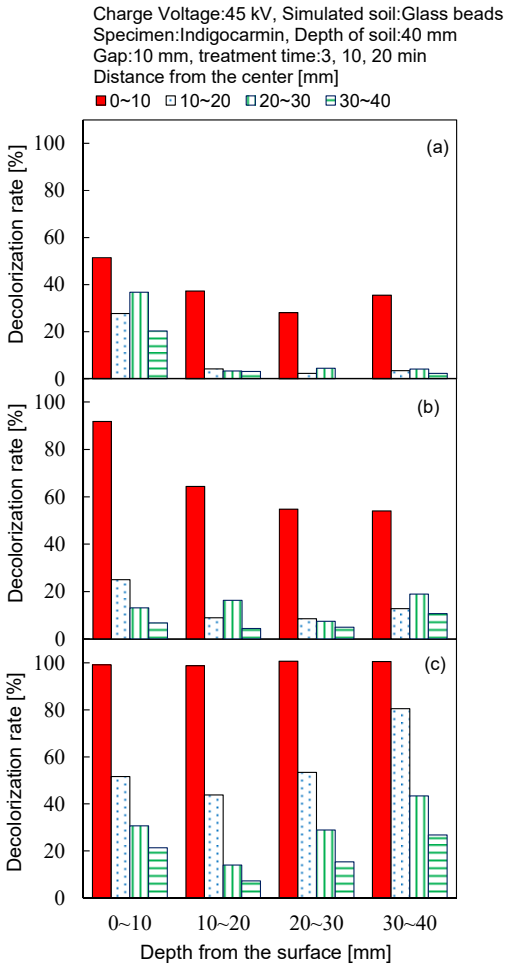

Fig. 5 Indigo carmine decolorization rate change with discharge treatment time change: (**a**) 3 minutes; (**b**) 10 minutes; (c) 20 minutes.

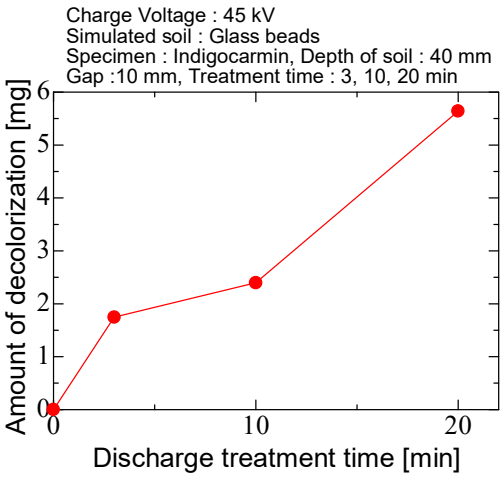

Fig. 6 Change in indigo carmine decolorization volume as a function of discharge treatment time

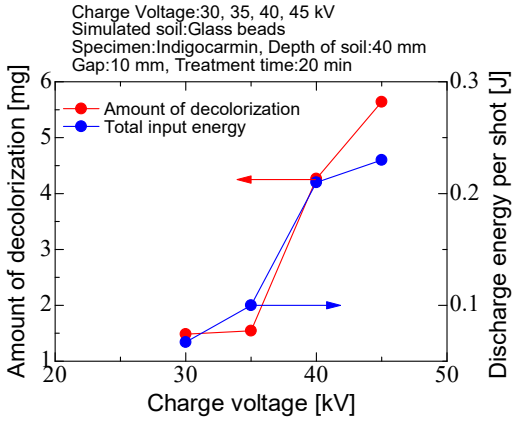

Fig. 7 Indigo carmine decolorization amount change with charging voltage

discharge through the soil was ever obtained, there was no significant difference in the amount of decolorization, whereas at charge voltages of 40 kV and higher, there was a significant increase in decolorization. This indicates that the generation of spark discharges affects the decolorization of indigo carmine.

The influence of the gap distance between the electrode tip and the soil surface on the decolorization was evaluated. Figures 8 shows the distribution of decolorization rate of indigo carmine for distance between soil surface of (a) 1 mm, (b) 5 mm and (c) 10 mm. Figure 8 shows that the decolorization rate of the soil surface was higher at a distance of 10 mm than at a distance of 1 mm between the soils. Figure 9 shows a photograph of the discharge at a distance of 1 mm between electrodes. The discharge extends directly downward. From the above, the distance from the high-voltage needle electrode to the soil is short, the discharge does not expand to the radial direction at the surface of the soil. The decolorization near the grounded electrode is enhanced with decreasing the electrode distance. Number of spark discharges observed when the soil distance was 1 mm was 100 times, 40 times at 5 mm, and 20 times at 10 mm, respectively. The shorter the distance between the soils, the more discharge penetrates into the soil, which increases the electric field near the ground electrode and promotes the generation of discharges, enhancing a decolorization reaction.

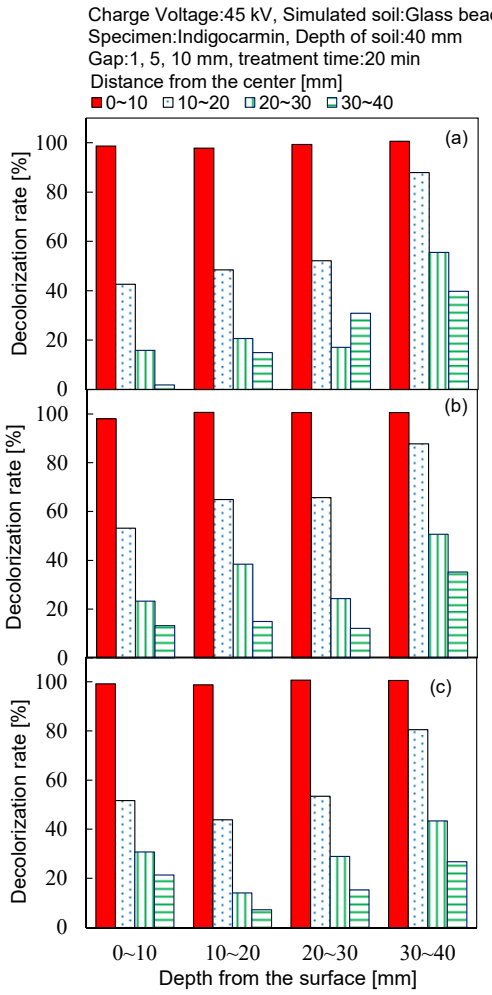

Fig. 8 Variation of indigo carmine decolorization rate with distance between soils: (a) 1 mm; (b) 5 mm; (c) 10 mm

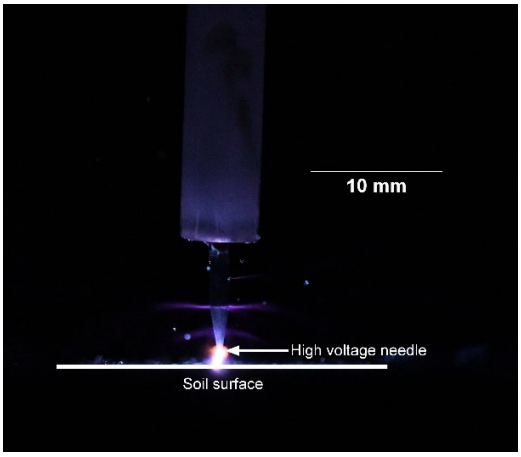

Fig. 9 Photograph of discharge at a distance of 1 mm between electrodes.

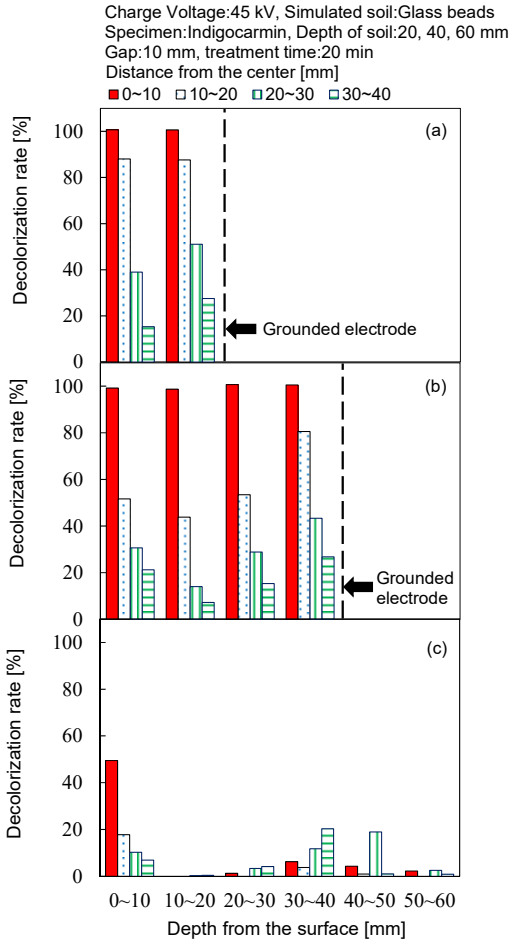

Fig. 10 Variation of indigo carmine decolorization rate with soil thickness: (a) 20 mm; (b) 40 mm; (c) 60 mm.

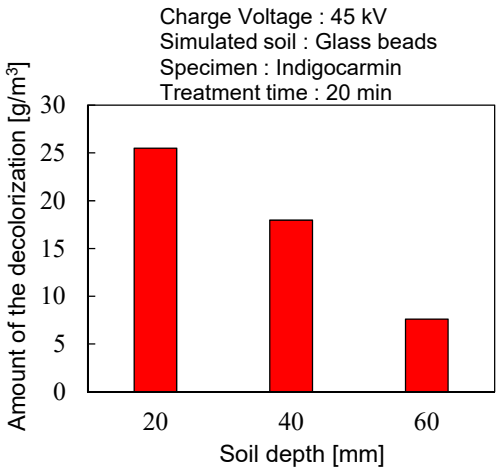

Fig. 11 Indigo carmine decolorization per unit volume by soil thickness

3.4 Influence of soil thickness change

Figure 10 shows the distribution of decolorization rate for soil thickness of (a) 20mm, (b) 40 mm and (c) 60 mm. The figure shows that the decolorization rate increases with decreasing soil thickness. The number of spark discharges observed during 100 discharges was 100 for a soil thickness of 20 mm, and 20 for 40 mm. In the case of a soil thickness of 60 mm, the spark discharges are not observed. The electric field increases with decreasing the soil thickness, which promotes of spark discharges and enhances the decolorization reactions. At a soil thickness of 60 mm, the decolorization rate increased only at the center of the soil surface because discharge did not penetrate into the soil. Figure 11 shows the amount of indigo carmine decolorization per unit volume according to soil thickness. The amount of decolorization also increased with decreasing soil thickness. The amount of indigo carmine decolorization per soil volume was divided by the discharge energy per shot. The energy per shot was 0.18 J for a soil thickness of 20 mm, 0.22 J for 40 mm, and 0.17 J for 60 mm. The energy efficiency per soil volume was 141 $g/m^3 \cdot J$ for a soil thickness of 20 mm, 81.6 $g/m^3 \cdot J$ for 40 mm, and 44.7 $g/m^3 \cdot J$ for 60 mm. This indicates that a smaller soil thickness is better for efficient discharge treatment.

4. Conclusions

The spatial distribution of soil oxidation by discharge treatment using simulated soil was investigated to study the oxidation ability of soil by high voltage pulse discharge. As a result, the higher the charging voltage and discharge treatment time, the more discharge waveforms through the soil were acquired, and the amount of indigo carmine decolorization increased. The main areas of oxidation reaction were the soil surface, the discharge path, and the soil near the ground electrode. The smaller the distance between the soils, the more the discharge penetrated the soil, and the more the decolorization rate increased. Smaller soil thicknesses were more efficiently processed.

Acknowledgments

This work was supported by a Grants-in-Aid for Scientific Research (S) (No. 19H05611).

References

[1] Dong, L., Xu, J., Feng, G., Li, X. & Chen, S. Soil bacterial and fungal community dynamics in relation to Panax notoginseng death rate in a continuous cropping system. *Sci. Rep.* 2016, Volume. 6, pp.1-11, 31802.

[2] Rosskopf, E. N., Chellemi, D. O., Kokalis-burelle, N. & T. Church, G. Alternatives to Methyl Bromide : A Florida Perspective, *Plant Heal. Prog.* 2005, Volume. 6, No. 1, 9.

[3] J. B. Ristaino and W. Thomas, Agriculture, Methyl Bromide, and the Ozone Hole: Can We Fill the Gaps?, *The American Phytopathological Society*, 1997, Volume. 81, No.9, pp.964-977.

[4] Bletsos, F. A. & Olympios, C. M. Rootstocks and Grafting of Tomatoes, Peppers and Eggplants for Soil-borne Disease Resistance, Improved Yield and Quality. *Eur. J. Plant Sci. Biotechnol.* 2008, Volume. 2, pp.62–73.

[5] Oriel, Michel, et al. "Illnesses associated with chloropicrin use in California agriculture, 1992–2003." *Reviews of Environmental Contamination and Toxicology.* 2009, Volume. 200, pp1-31.

[6] Lazra, Y. *et al.* Effects of atmospheric plasma corona discharges on soil bacteria viability. *Microorganisms.* 2020,Volume. 8, 704.

[7] Mitsugi, F. et al. Influence of Ozone Generated by Surface Barrier Discharge on Nematode and Plant Growth. *IEEE Trans. Plasma Sci.* 2016, Volume. 44, pp.3071–3076.

[8] Takahashi, K. *et al.* Development of automatically controlled corona plasma system for inactivation of pathogen in hydroponic cultivation medium of tomato. *J. Electrostat.* 2018, Volume. 91, pp.61–69.

[9] Nor, N. M., Haddad, A. & Griffiths, H. Characterization of ionization phenomena in soils under fast impulses. *IEEE Trans. Power Deliv.* 2006, Volume. 21, pp.353–361.

Influence of Gas Species on Electrical Characteristics of High-Power Pulsed Sputtering

Taishin Sato, Katsuyuki Takahashi*, Seiji Mukaigawa and Koichi Takaki*

Iwate University, Japan

**Agri-Innovation Center, Iwate University*

ABSTRACT

The influence of gas species on electrical characteristics of high-power pulsed sputtering (HPPS) discharge was investigated. The HPPS discharge is a sputtering system with two targets on the same potential facing each other. The titanium (Ti) target with a length of 60 mm, a height of 20 mm and a thickness of 5 mm was used and the gap length was set to be 10 mm. The magnetic field is created by a set of permanent magnets behind the facing targets. The magnetic field strength at the gap between the targets was 0.2 T. Electrons are trapped targets by the magnetic and electric fields to ionize gas in the gap. Argon (Ar) or nitrogen (N_2) gas was fed into the chamber with a gas pressure of 4 Pa. A rectangular pulse voltage with an amplitude in the range of -600 V to -1000 V and a pulse width of 600 μs was applied. The target current in Ar gas was approximately 35 A and was higher than 10 A in N_2 gas. The consumed power were 12 kW and 13 kW in Ar and N_2 gas, respectively. The ion density at the surface of the ionization region were 3.0×10^{19} and 1.7×10^{19} m^{-3} in Ar and N_2 gas, respectively, by the double probe measurements. The ion density decreased with increasing the vertical distance.

Keywords

HiPIMS, Sputtering, Glow Discharge, Magnetic confinement

1. Introduction

Thin film deposition is an important process for various applications of materials. It is used in various fields such as tools, industrial components, and semiconductor devices. Nitride films, such as titanium nitride (TiN) and chromium nitride (CrN), have been used in various components because of their good wear, fatigue, and corrosion resistance[1]–[3] TiN films are expected to be applied to medical application because it's high biocompatibility. Reactive magnetron sputtering with direct current (DC) or radio frequency (RF) power supply has been proposed as a method for nitride film deposition. The magnetic field of magnetron sputtering is generated on the target surface by the permanent magnets placed behind to the target. Electrons are trapped on the target surface by the magnetic and electric fields to generate high-density plasma and increase the deposition rate. The power input of DC and RF is limited to 200-500 kW/m^2 to prevent the transition from glow discharge to arc discharge owing to heating of the target by interaction with the plasma, which causes its low ionization rate. Therefore, the sputtered particles are almost neutral, and it is difficult to control the particles bombarding the substrate with bias voltage. The control of the ion bombardment to the substrate is important because it affects the hardness and wear resistance of the film. High-power impulse magnetron sputtering (HiPIMS) has been proposed by Kouznetsov *et al.* as a method of magnetron sputtering with a short-term application of high power in the order of 10^5 kW/m^2 using pulsed power supply to improve the ionization rate of sputtered particles[4]. In HiPIMS, the ionization rate of sputtered particles reaches more than 50–90 %[5]. It is

one of the most promising methods for droplet-free deposition owing to its high power density and high ionization rate. However, the target utilization efficiency is low and the system size is large. To overcome the disadvantages of HiPIMS, a high-power pulsed sputtering (HPPS) discharge with two two facing targets has been developed[6]. In the HPPS discharges, the permanent magnets behind the targets generate the magnetic field perpendicular to the target surface. The electric field is created by applying a pulsed negative voltage. Electrons undergoing cyclotron motion around the magnetic field effectively ionize the gas in the gap between the targets. After the plasma ignition, the cathode fall region is formed near the targets. The direction of the electric field around the HPPS discharge is perpendicular to the magnetic field. The electrons diffusing from the gap to the chamber wall move in the direction perpendicular to the magnetic field. Therefore, the Lorentz force reduces the diffusion and generates the glow discharge with high plasma density at between the target electrodes. In addition, HPPS discharge is expected to improve the ionization rate of sputtered particles by using a pulsed power supply. The advantages of HPPS discharge are suitable for small substrates and low-volume production. It has also been reported that power and plasma densities equivalent to HiPIMS[7]. Although electrical and sputtering characteristics of HPPS discharge in argon gas have been reported[8], there are few reports about that in nitrogen gas. In this study, the electrical characteristics of HPPS discharges are compared with those using nitrogen and argon gas. The voltage and current (V-I) characteristics were obtained by using target voltage and current waveforms. Axial and radial distribution of electron temperature and ion density were also obtained. Optical Emission Spectroscopy (OES) was performed to confirm the ionization of the sputtered particles used as the targets.

2. Experimental Setup

Figure 1 shows a schematic diagram of the HPPS unit. The HPPS unit is compact in size (60 × 67 × 86 mm^3). A pair of rectangular titanium (Ti) plates with a length of 60 mm, a height of 20 mm and a thickness of 5 mm was used as the sputtering target cathode. Two Ti target plates were placed on the magnet holders (SUS304) in which samarium-cobalt (SmCo) permanent magnets (540 mT, diameter 15 mm, height 10 mm) were placed on the opposite side with a gap length of 10 mm. A magnetic field was produced perpendicular to the targets. The strength of the magnetic field in the gap was approximately 0.2 T. Figure 2 shows a schematic diagram of the experimental apparatus. A cylindrical vacuum chamber with a diameter of 320 mm and with a height of 200 mm was evacuated to 5×10^{-3} Pa, and then the argon (Ar) or nitrogen (N_2) gas was fed into the chamber at a gas pressure of 4 Pa using a mass flow controller (HORIBA, SEC-400MK3). The pressure was observed with two different pressure gauges (MG-2I, M-320XG). Two 10 Ω resistors (Japan Resistor Mfg. Co., Ltd., GR400 100K) were connected in series with the HPPS unit to prevent the HPPS discharge plasma from transitioning from glow discharge to arc discharge due to overcurrent. A rectangular pulsed voltage V_{app} with a pulse width of 600 μs and an amplitude ranging from -600 V to -1000 V was applied to the HPPS unit with resistors connected in series using a high-voltage pulse power supply (PEKURUS, KJ06-3265; -3 kV, 100 A, 1 kHz, 1 ms). The pulse repetition rate was fixed at 1 Hz. The target voltage V_T [V] applied to the cathode targets was measured with a high-voltage probe (Tektronix, P5100A; 2.5 kV, 500 MHz). The target current I_T [A] flowing into the cathode targets was measured with current transformers (PEASON, CURRENT MONITOR 110A, Pearson 411). The voltage and current waveforms were monitored with a digital oscilloscope (Tektronix, DPO 4104B). The consumed power in plasma P can be obtained from the V_T and I_T using the following equation.

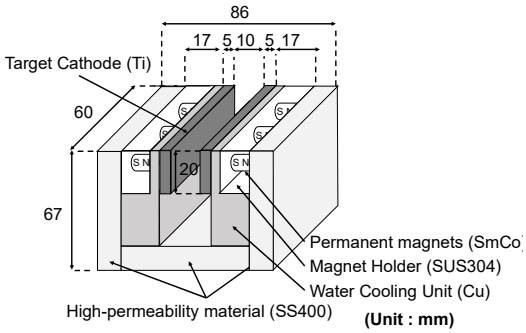

Fig. 1. HPPS unit

$$P = V_T \times I_T$$

The position distributions of electron temperature and ion density were obtained using the double probe measurements. Figure 3 shows the double probe measurement. The probe tip was a cylindrical tungsten electrode with a diameter of 1 mm and, an exposed length of 4 mm, and the rest of the probe was protected by a glass tube to prevent exposure to the plasma. Two of these electrodes were used to form a double probe. The probe voltage was varied from -40 V to 40 V. The potentials of the two electrodes and the power supply that applied the voltage to the probe were floating. A 33 μF ceramic capacitor was connected in parallel with the probes to prevent voltage drop. To measure the vertical distribution of electron temperature and ion density, the double probe was placed at the center between the target electrodes and at a distance L away from the HPPS unit. L = 0 mm was the surface of the HPPS unit, and L was varied from 0 mm to 60 mm. To measure the horizontal distribution of electron temperature and ion density, the probe was also positioned from the front of the chamber. The probe was placed at a vertical distance L of 30 mm and the probe was placed at a horizontal distance R. R was varied from 0 mm to 80 mm parallel to the target electrodes. The probe current was measured by changing the probe voltage. Assuming that the electron energy distribution function is Maxwellian, the electron temperature T_e is calculated as follows:

$$\mathrm{d}\ln(\Sigma I_i / I_{e1} - 1) / \mathrm{d}V_p = -e / kT_e$$

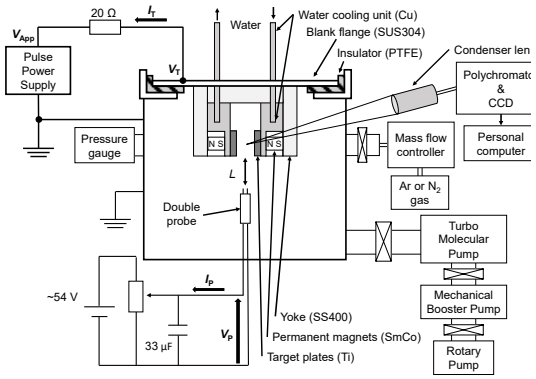

Fig. 2. Schematic diagram of the experimental apparatus

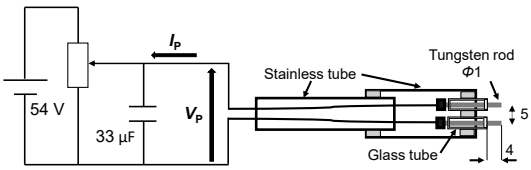

Fig. 3. The double probe measurement

where e is the elementary charge, k is the Boltzmann constant. ΣI_i and I_e are the ion current and the electron current flowing in the probe at 400 μs, and V_p is the probe bias. The ion density n_i is calculated as follows,

$$n_i = I_i / 0.61 e u_B$$

where I_i is the ion saturation current, S is the surface area of the probe and u_B is the Bohm velocity. Optical emission spectroscopy (OES) was measured using a spectrometer (StellarNet, BLUE-Wave UVN-25; 600 Gr mm^{-1} grating). The plasma emission was observed by focusing on the center of the gap using a condenser lens with a focal length of 200 mm. The exposure time was 1 s. The excitation and ionization rates of the target were estimated from the measured emission intensities.

3. Results and Discussion

3.1 Electrical Characteristics

Figure 4 shows typical waveforms of (a) the target voltage, (b) the target current and (c) the consumed power in Ar and N_2 gas at -1000 V applied voltage. The target voltage at the plasma ignition was -350 V and -600 V in Ar and N_2 gas, respectively. The target voltage

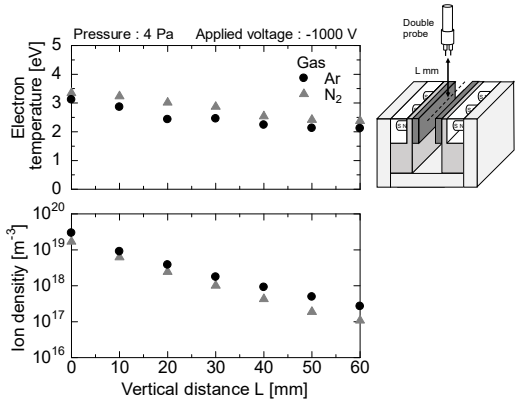

Fig. 6. The electron temperature and ion density as a function of the vertical distance L from the electrode surface as measured by the double probe measurements

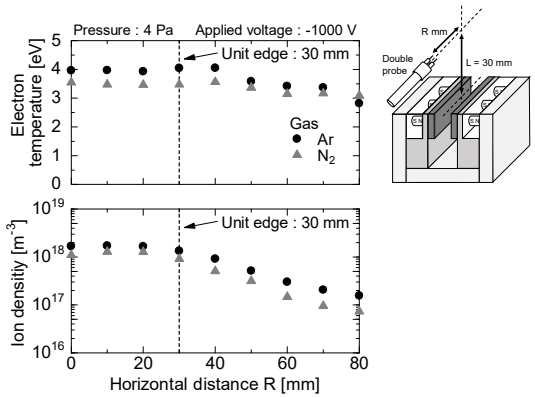

Fig. 7. The electron temperature and ion density as a function of horizontal distance R from the electrode

nm) is more prominent in Ar gas than in N_2 gas.

Figure 9 shows the OES intensities at 368.25, 391.44, 498.17 and 334.94 nm corresponding to the excitation states of Ar II, N_2^+, Ti I and Ti II, respectively, as a function of consumed power in (a) Ar and (b) N_2 gas. The OES intensities of the gas ions and Ti increased with increasing consumed power.

4. Conclusions

The electrical characteristics of HPPS discharges are compared with those using nitrogen and argon gas. The target current in Ar gas was approximately 35 A and was higher than 10 A in N_2 gas. The target voltage was almost constant regardless of the applied voltage,

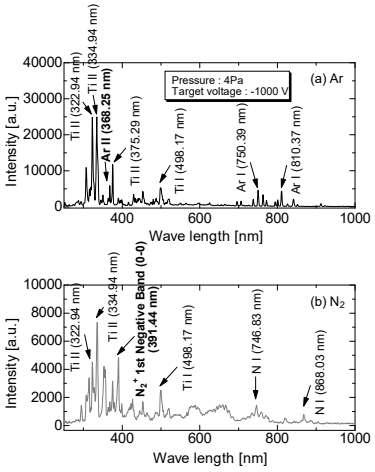

Fig. 8. Emission spectra in (a) Ar and (b) N_2 gas

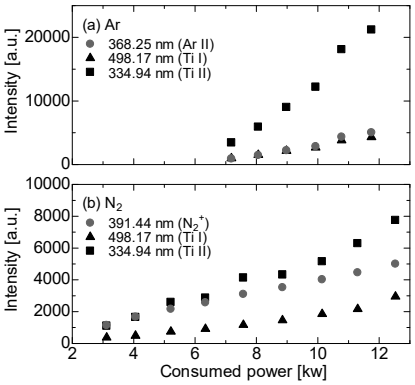

Fig. 9. The OES intensities at 368.25, 391.44, 498.17 and 334.94 nm corresponding to the excitation states of Ar II, N_2^+, Ti I and Ti II, respectively, as a function of the consumed power in (a) Ar and (b) N_2 gas

showing normal glow characteristics. The vertical distribution of electron temperature and ion density ranged from 2.0 eV to 3.5 eV and 10^{17} m^{-3} to 10^{19} m^{-3}, respectively. The horizonal distribution of electron temperature and ion density also ranged from 2.8 eV to 4.0 eV and 10^{16} to 10^{18} m^{-3}, respectively. The electron temperature and ion density were not affected by the horizontal distance when the horizontal distance was less than 30 mm. However, when the horizontal distance is in the range of 40 to 80 mm. In the emission spectra, Ti I and Ti II are dominant in both spectra.

Acknowledgments

The author would like to thank Ken Yukimura for his valuable comments and discussions. The author would also like to thank Yutaka Shida at the Iwate University technical staff. This work was supported by a Grant-in-Aid for Scientific Research (S) from the Japan Society for the Promotion of Science, Grant Number 19H05611.

References

[1] B. Y. Tang, P. K. Chu, S. Y. Wang, K. W. Chow, and X. F. Wang, "Methane and nitrogen plasma immersion ion implantation of titanium metal," *Surf. Coatings Technol.*, vol. 103-104, 1998.

[2] T. Czerwiec, N. Renevier, and H. Michel, "Low-temperature plasma-assisted nitriding," *Surf. Coatings Technol.*, vol. 131, no. 1-3, pp. 267-277, 2000.

[3] B. Navinšek, P. Panjan, and J. Krušič, "Hard coatings on soft metallic substrates," *Surf. Coatings Technol.*, vol. 98, no. 1–3, pp. 809–815, 1998, doi: 10.1016/S0257-8972(97)00316-2.

[4] V. Kouznetsov, K. MacÁk, J. M. Schneider, U. Helmersson, and I. Petrov, "A novel pulsed magnetron sputter technique utilizing very high target power densities," *Surf. Coatings Technol.*, vol. 122, no. 2–3, pp. 290–293, 1999, doi: 10.1016/S0257-8972(99)00292-3.

[5] G. Bräuer, B. Szyszka, M. Vergöhl, and R. Bandorf, "Magnetron sputtering - Milestones of 30 years," *Vacuum*, vol. 84, no. 12, pp. 1354–1359, 2010, doi: 10.1016/j.vacuum.2009.12.014.

[6] K. Yukimura, R. Mieda, H. Tamagaki, and T. Okimoto, "Electrical characteristics of arc-free high-power pulsed sputtering glow plasma," *Surf. Coat. Technol.*, vol. 202, no. 22–23, pp. 5246–5250, 2008, doi: 10.1016/j.surfcoat.2008.06.021.

[7] K. Azuma and T. Kimura, "Plasma Parameters of Titanium-Based Metallic Plasma Generated by a Compact-Type High-Power Pulsed Sputtering Penning Discharge," *IEEE Transactions on Plasma Science*, vol. 44, no.12, pp. 3201-3206, 2016.

[8] S. Abe, K. Takahashi, S. Mukaigawa, K. Takaki, and K. Yukimura, "Comparison of plasma characteristics of high-power pulsed sputtering glow discharge and hollow-cathode discharge," *Jpn. J. Appl. Phys.*, vol. 60, no. 1, p. 015501, 2020, doi: 10.35848/1347-4065/abcd78.

Observation of the stripe and filamentary self-organized structure of atmospheric pressure nitrogen microgap dielectric barrier discharge

Ryota Akaishi, Katuyuki Takahashi, Koichi Takaki, Seiji Mukaigawa

Iwate University, Ueda 4-3-5, Morioka, Iwate 020-8551, Japan

ABSTRACT

In this study, the discharge phase of an atmospheric pressure nitrogen microgap dielectric barrier discharge self-organized structure was observed. Stripe structures were observed in discharge patterns with two peaks of discharge current under conditions of long exposure time and a high number of integration times. In the discharge region, with an exposure time of 1 μs and several integrations of 1, discharges with a random arrangement of large and small filaments were observed. The average movement speed of the filament was estimated to be at least 61 mm/s.

Keywords

Microgap dielectric barrier discharge, Nitrogen plasma, Self-organized plasma, hexagonal filament structure

1. Introduction

A dielectric barrier discharge (DBD) is a discharge caused by an alternating voltage applied to a pair of electrodes, one or both of which are covered in the dielectric material. Microplasmas generated by DBD have been observed to self-organize their discharge structure under certain conditions (applied voltage, frequency, gas species, gas flow rate, dielectric material, gap length, and electrode structure) [1]. DBD self-organization is believed to be based on the Turing mechanism, and theoretical models to explain this self-organization have also been proposed [2]. Self-organization is an undesirable nonuniform discharge in several industrial applications; however, the periodic discharge structure generated by self-organization has recently been applied to plasma photonic crystals [3]. With short-time observation techniques, hexagonal lattice structures and stripe structures in helium microgap DBDs are visually observed, and stripe structures are shown to be composed of hexagonal structures [4]. There are several examples of observations of stripe structures in the case of N_2 discharge, but no observations of discharge phases on a short-time scale have been reported.

Fig. 1. Schematic of a microgap discharge cell

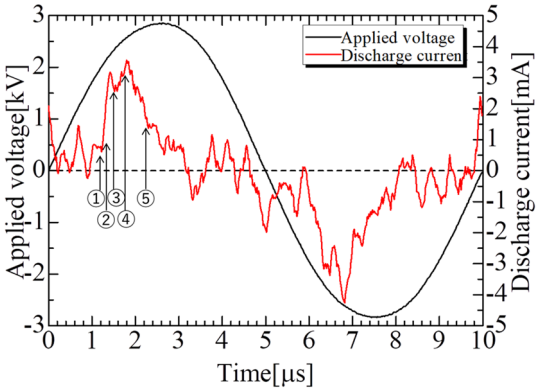

Fig. 2. Voltage and current waveforms during the formation of self-organized structures.

In this study, we observed the self-organized structure of atmospheric pressure nitrogen microgap

DBDs in real time to better understand the discharge phase, particularly the stripe structure pattern.

2. Experimental Setup

The microgap discharge cell is schematically depicted in Figure 1. The dielectric length is 0.53 mm and the gap length is 0.14 mm; both the dielectric and the spacer are glass with a relative permittivity of 6.7. The electrode consisted of 15 × 10 mm indium tin oxide, which was deposited on one side of the dielectric. The power source was a high-frequency power supply with a frequency of 100 kHz. The applied voltage and current were measured using a high voltage probe (Tektronix P6015) and a Rogowski coil (Pearson CT2877) respectively, and the waveforms were viewed on an oscilloscope. The discharge current was calculated using equivalent circuit analysis from the measured voltage and current waveforms. To capture discharge images, an ICCD camera (HAMAMATSU PHOTONICS K.K. M7971-01) with a gate width of 1 ms–100 ns and a totalization frequency of 1–500 was used. Nitrogen was used as the gas and the flow rate was controlled by a mass flow controller.

3. Results and Discussion

The voltage-current waveforms during the formation of the self-organized structure are depicted in Fig. 2. The voltage applied is 2.7 kV, and the flow rate is 2.0 L/min. A pulse of discharge current can be seen once every half cycle.

The time evolution of the discharge phase as captured by the ICCD camera is depicted in Fig. 3. Each image from (1) to (5) corresponds to time from (1) to (5) noted on the waveform in Fig. 2. The exposure time is 100 μs and the number of integrations is 500. In the upper part of the image, the gas flow is upstream, and in the lower part, it is downstream. The images were adjusted so that the luminance was uniform throughout. The central part of the stripe was discharged at time (1) and the stripe discharge was observed at time (2). At time (3) the entire stripe discharge weakened, at time (4) the discharge of the stripe structure collapsed, and at time

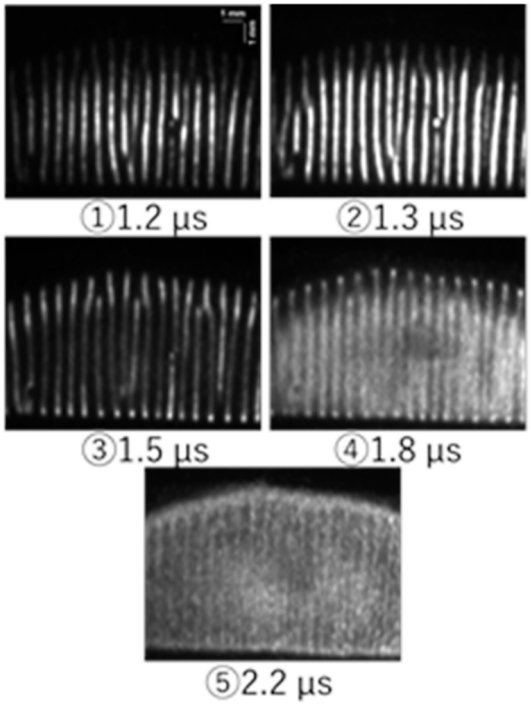

Fig. 3. Discharge phase in time evolution (exposure time 100 ns, integration times 500).

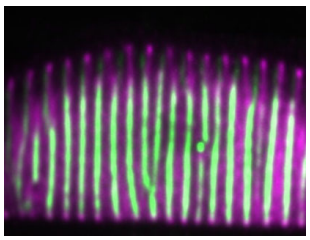

Fig. 4. Superimposition of discharge images at ②t = 1.3 μs(green) and ④t = 1.8μs(magenta)

(5) an interfilament discharge was observed.

Fig. 4 shows the superposition of image Fig. 3.② (t = 1.3 μm) and image Fig. 3.④ (t = 1.8 μm). Image ② is represented by green and image ④ by magenta. The superimposition of images using these colors results in the superimposition of two images. When images are superimposed using these colors, the overlapping area of the emission region of the discharge in the two images becomes white. In Fig. 4, there are many areas that show the colors of images ② and ④, and only a few areas that are white. There is little overlap in the position of the discharges. Therefore, the stripe-shaped self-organized discharge at t = 1.8 μm occurs between the stripe-shaped discharges that occurred at t = 1.3 μm. Therefore, the

interfilament discharge at t = 1.8 μm occurs between the stripe discharges that occurred at t = 1.3 μm.

Fig. 5 depicts images of the discharge aspect taken at time (Fig. 3.②) t = 1.3 μs with various exposure times. The number of integrations has been limited to one. Stripe structures were observed at (a) an exposure time of 1 ms, filament structures were observed at (b) 100 μs and (c) 50 μs exposure times. At (d) exposure time of 1 μs, random discharges of large and small filaments were observed in the discharge region. By superimposing several discharges, the hexagonal structural arrangement of filaments in nitrogen microgap discharges is observed, indicating that filaments do not simultaneously appear in a single discharge current pulse.

A magnified superposition of images taken at exposure times of (b) 100 μs and (c) 50 μs is depicted in Fig. 6. The time of exposure is t = 1.3 μs. The image with an exposure time of 100 μs is marked in green and the one with an exposure time of 50 μs in magenta. The filaments depicted in these images occur on the same stripe but at slightly different positions.

The filaments in Figs. 5(b) and 5(c) have nearly the same diameter and filament spacing and can thus be considered similar filaments. As a result, the stripe structure observed at longer exposure times is thought to be caused by filament movement in the flow direction when the gate is open. Based on this concept, the filament average movement speed can be approximated in the following manner. For the filaments to seem to overlap during the exposure time Δt, the distance traveled in the gas flow direction must be at least $\Delta\bar{L} = \bar{L} - \bar{L}^{\wedge\prime}$ must be greater. From this, the upper limit of the filament velocity can be expressed as follows:

$$\Delta L / \Delta t = v$$

From Figs. 5(b) and 5(c), $\bar{L}$ = 0.27 mm and $\bar{L}^{\wedge\prime}$ = 0.26 mm, which gives an average filament travel speed of at least 61 mm/s. This velocity is lesser than the gas velocity.

4. Conclusions

To analyze the stripe structure, short-time

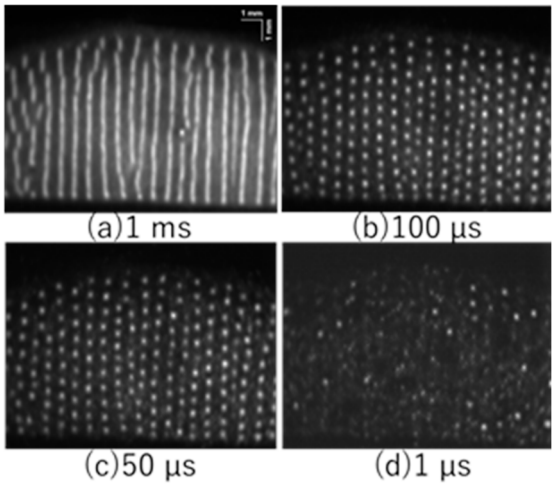

Fig. 5. Variation of discharge aspect with

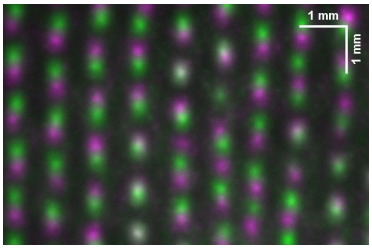

Fig. 6. Superimposition of discharge phases (Fig. 5(b) GREEN and Fig. 5(c) MAGENTA)

observations of atmospheric pressure nitrogen microgap DBD self-organized structures were performed in this study. Large and small filaments were randomly discharged in the discharge region, according to observations of the discharge aspect with an exposure time of 1 μs and an integration count of 1. On the basis of the images with varying exposure times, the average movement speed was estimated to be at least 61 mm/s.

References

[1] E. Ammelt, Yu. A. Astrov, H. G. Purwins. Phys. Rev.E. **58**, 7109-7117 (1998).

[2] C.Radehaus, H.Willebrand, R.Dohmen, and F.-J.Niedernostheide, G.Bengel, H.-G.purwins. Phys. Rev. A, **45**, 2546 (1992).

[3] O. Sakai, T. Sakaguchi, K. Tachibana. Appl. Phys. Lett. **87**, 241505 (2005).

[4] H. Sato, et al., IEEE Trans. Electron Devices **49**, 91-97 (2021).

Filamentation of 2.45-GHz microwave discharge plasmas in sub-atmospheric pressure

Zentarou Sasaki, Tsubasa Saito, Takaharu Kamada*, Katsuyuki Takahashi, Koichi Takaki and Seiji Mukaigawa

Iwate University, Ueda 4- 3-5, Morioka, Iwate 020-8551, Japan.

* *National Institute of Technology Hachinohe College, Tamonoki Uwanotai 16-1, Hachinohe, Aomori 039-1192, Japan*

Abstract: Filamentary discharge plasmas were generated by 2.45-GHz microwave in a sub-atmospheric pressure. The filament length and thickness were measured. The results show that the maximum length, which is about half of the wavelength in the tube of a vacuum vessel considered a waveguide, is determined by a change in power balance due to circuit losses independent of pressure. Increasing pressure decreases the plasma volume but does not change the power consumption because the plasma density also increases.

Keywords: Microwave plasma, photonic crystals

1. Introduction

Plasma photonic crystals (PPCs), which are periodically arranged plasmas, have potential engineering applications for electromagnetic wave control devices. In this study, we generate filamentary structures using 2.45-GHz microwave discharge plasmas, which can generate high-density plasma, and study their plasma characteristics, bearing in mind the construction of PPCs designed to control electromagnetic waves near 10 GHz.

The radial contraction of plasmas at atmospheric pressure is often observed in microwave plasmas [1,2]. To obtain stable plasma filaments, filamentary discharges on electrode rods are generated using a method in which copper electrode rods are placed inside a cylindrical metal container as a cavity resonator under sub-atmospheric pressure with zero flow velocity. To control the filamentary structures, changes in microwave power balance and plasma filament length and thickness were measured in the pressure range of 200–900 hPa and microwave incident power range of 150–900 W. Plasma densities were also determined from emission spectroscopy.

2. Experimental set-up

Figure 1 shows a schematic of our experimental set-up. The microwave power supply comprises a control unit (JHF MKN-102-3S2-PS), a generator (JHF MKN-102-3S2-0SC), an isolator (JHF WUG-22M1), a directional coupler (JHF WDK-C-0295), a 3-stub matching device (JHF WMS-021XH2B) and a mode changer (WTM-TE10-TM01). Microwaves are introduced into a cylindrical vacuum vessel (as a cavity resonator). The microwave power is measured by a directional coupler, and the input power P is obtained by the difference between the incident power P_{inc} and the reflected power P_{ref} ($P = P_{inc} - P_{ref}$). He gas is introduced from the vacuum vessel's side and evacuated from its bottom by a rotary pump (ALCATEL Pascal 10).

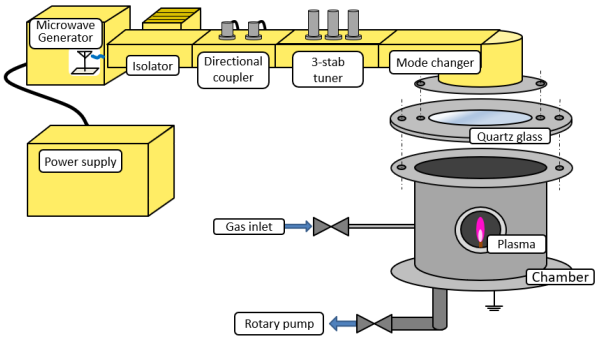

Fig. 1. Experimental set-up.

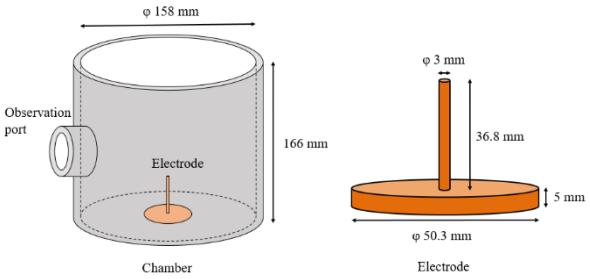

Fig. 2. Vacuum chamber (as a cavity resonator) and electrode.

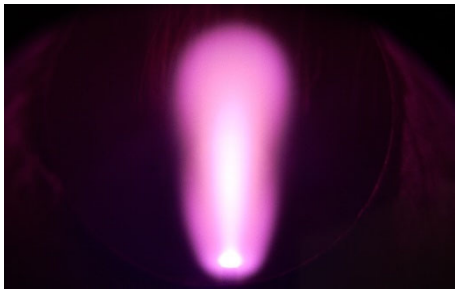

Fig. 3. Typical image of the microwave plasma filament.

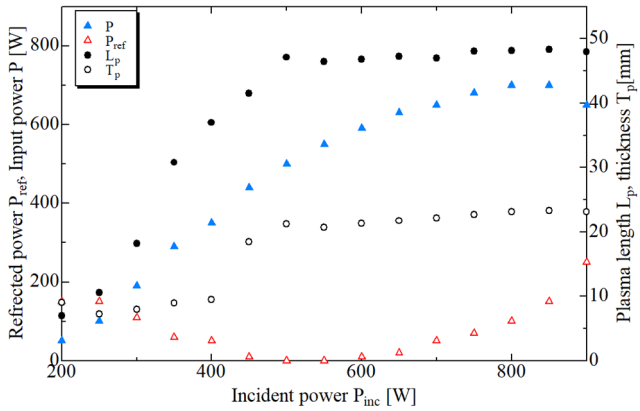

Fig. 4. Filament length L_p and filament thickness T_p.

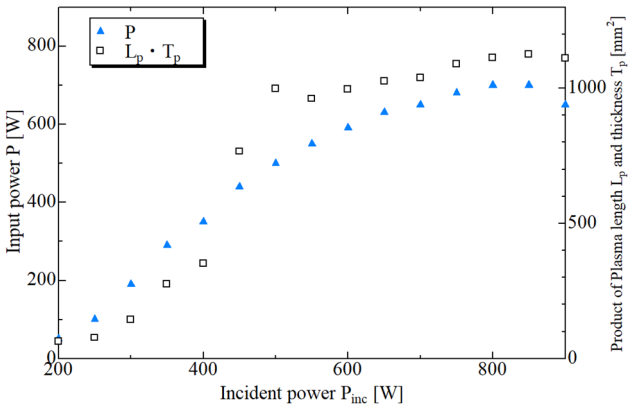

Fig. 5. Product of Filament length L_p and thickness T_p versus P_{inc} at 500 hPa.

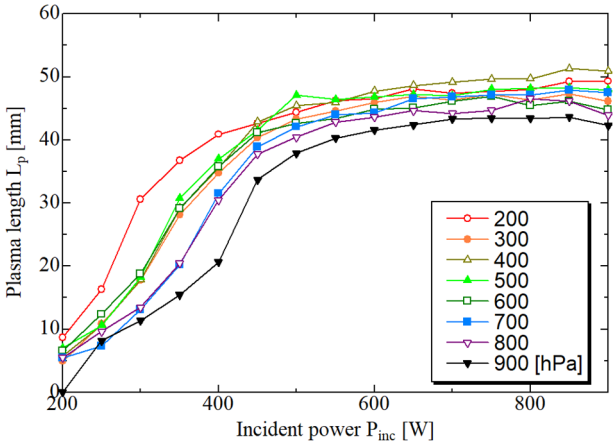

Fig. 6. Plasma length L_p at several sub-atmospheric pressures.

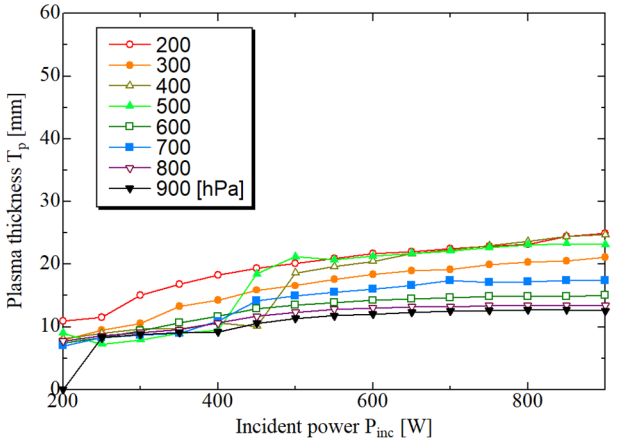

Fig. 7. Plasma thickness T_p at several sub-atmospheric pressures.

Figure 2 shows the copper electrodes and their arrangement in the vacuum vessel. The vacuum vessel has an inner diameter and height of 158 and 166 mm, respectively, and is made of Type 304 stainless steel. It has two observation windows, which are used for digital imaging and spectroscopy. The copper electrodes comprise a supporting disc and a rod. The diameter and thickness of the disc are 50.3 and 5.0 mm, respectively, and the length and thickness of the rod are 3.0 and 36.8 mm, respectively. The electrode rod is placed at the centre of the lower part of the vacuum vessel and is electrically grounded.

Figure 3 shows a typical image of the generated microwave plasma filament at a 1,000-hPa pressure and a 450-W input power (500-W incident power and 50-W reflected power).

When microwaves are injected into the vacuum vessel, plasma filaments are generated on the electrode rods. The gas flow rate is zero. The filament length and thickness are obtained from images captured by a digital camera (NIKON Coolpix S9900), which are converted to 16-bit grayscale and binarised to separate the discharge region. Emission spectra are measured using a spectrometer (HAMAMATSU PHOTONICS C10027-01, 200–950 nm, FWHM < 2 nm). Excitation temperatures and electron densities are determined from the emission spectra. Excitation temperatures were determined by the two-line intensity ratio method using He 706 nm lines (20.96–22.72 eV, $1.83 \times 10^7\ s^{-1}$) and He 587 nm lines (20.96–23.07 eV, $7.07 \times 10^7\ s^{-1}$) [3]. Electron densities are derived by measuring the Stark width of the 706 nm He lines. The instrumental width and gas temperature are assumed to be 3.59 nm and 10,000 K, respectively.

3. Results

Figure 4 shows the reflected power P_{ref}, input power P, plasma length L_p and plasma thickness T_p versus the incident power P_{inc} at a 500-hPa vessel pressure. The power input increases gradually with increasing incident power, approaching 700 W. The reflected power is the same as that of the matching plasma at 500 W (vessel pressure: 500 hPa). The reflected power is 0 W at an incident power of 500 W (matching point) and increases as one moves away from the matching point. The plasma length is nearly constant in the incident power range of

500–900-W (saturation region), about 40–50 mm, whereas it decreases as the incident power decreases from about 450 to 200 W (transition region), and the plasma turns off when the incident power falls below 200 W. The plasma thickness remains thin in the transition region, whereas it becomes one step thicker at about 20 mm in the saturation region.

Figure 5 shows the curves of the product of filament length L_p and filament thickness T_p against the input power P, indicating a strong correlation. In the saturated region, the $L_p \cdot T_p$ product increases with power input P, but the curve is relatively flat.

Figures 6 and 7 show the plots of L_p and T_p at 200–900 hPa. Most of the plots are correlated with the input power P, and the values of L_p and T_p generally decrease with increasing pressure. At a 100-hPa pressure, a filament is formed, and a uniform discharge occurs; meanwhile, at 900 hPa and 200 W, the plasma turns off.

Figure 8 is a plot of the values of the $L_p \cdot T_p$ product at 200–900 hPa. The values are highly pressure dependent, and the value of the $L_p \cdot T_p$ product tends to decrease with increasing pressure, attributable to the increase in the mean free path and the change in the breakdown electric field due to the reduced pressure affecting the filament cross-sectional area.

Figure 9 shows the excitation temperature and electron density values obtained from the emission spectra. The excitation temperature is around 6,000 K and varies slightly. The electron density varies in the range of $4.81 \times 10^9 - 4.02 \times 10^{10}$ cm^{-3}, with mild increasing trend with increasing pressure. The pressure variation range, as well as the electron density variation range, is approximately one order of magnitude, suggesting that the electron density variation is due to the pressure-induced plasma contraction.

The electron density is low because the spectrometer system's measurement range includes areas outside the filament region and a spatially averaged electron density is calculated. Because there is no significant change in the plasma density, the filament core is homogeneous, and the increase in filament length is attributable to the increase in core volume. The $L_p \cdot T_p$ product correlates well with the power input P, responding to pressure increase/decrease, and there is no pressure dependence of the incident and reflected power. The power consumption in the plasma is determined by the change in power balance due to circuit losses. In filament propagation, pressure also affects the length and thickness (and hence the volume) of the plasma. Meanwhile, the filament length takes a maximum value of about 50 mm to form a saturated region. When the vacuum vessel is considered a waveguide, the wavelength of 2.45-GHz microwaves in the tube, λ_g, is approximately 133 mm. The maximum value of about 50 mm is about half the wavelength in the tube (66.5 mm).

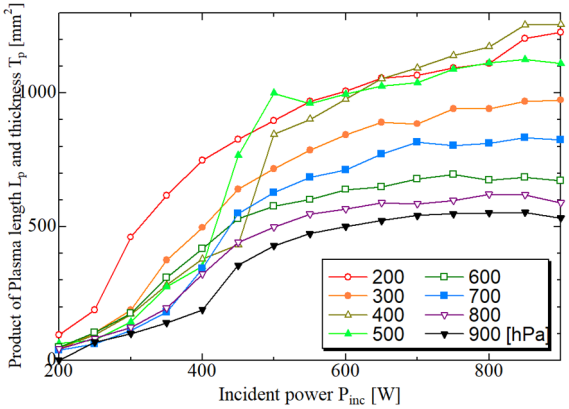

Fig. 8. Product of Plasma length L_p and thickness T_p in several sub-atmospheric pressures.

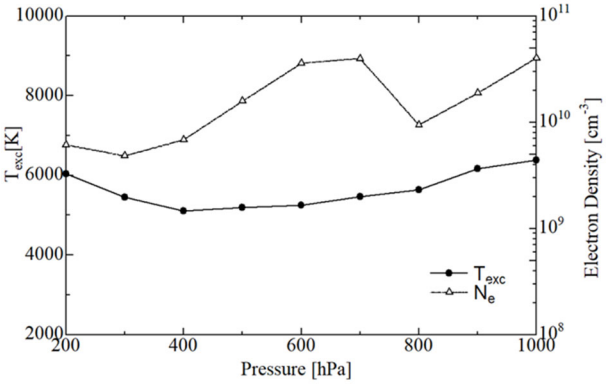

Fig. 9. Excitation temperature T_{exc} and electron density N_e as a function of pressure (P_{inc} = 500 W).

4. Conclusion

Filamentary discharge plasmas were generated by 2.45-GHz microwave irradiation in a sub-atmospheric pressure range of 200–500 hPa. The filament length L_p, the filament thickness T_p and the $L_p \cdot T_p$ product were investigated at 200–900 W incident power. The filament length is divided into two regions: transition and saturation. The filament length is proportional to the power in the former, whereas the filament length is stable at about 40–50 mm in the latter. The plasma filament size is determined by the change in power balance due to circuit losses independent of pressure. Increasing the pressure decreases the plasma volume but does not change the power consumption because the plasma density also increases.

5.References

[1] M. Snirer *et al.*, Plasma Sources Sci. Technol., **30**, 095009 (2021).
[2] J. Hnilica *et al.*, J. Phys. D: Appl. Phys., **45**, 055201 (2012).
[3] https://www.nist.gov/ He I lines and spectrum

Beam number dependence on implosion dynamics of fuel pellet with flower-shape tamper in heavy-ion inertial fusion

Zhehao LIN, Kazumasa TAKAHASHI, Toru SASAKI, Takashi KIKUCHI,
Atsushi SUNAHARA*
Nagaoka University of Technology
**Purdue University*

ABSTRACT

Implosion dynamics study is key issue in heavy-ion-beam driven inertial confinement fusion, which is hopeful to achieve fusion energy release. Modification of flower-shape tamper was proved to be effective to reduce the irradiation nonuniformity and increase areal density of fuel in our previous study. In this study, we present the effects of flower-shape tamper during implosion under the condition of different numbers of driven heavy-ion-beam.

Keywords

Heavy-ion-beam, Inertial confinement fusion, Modification of fuel pellet

1. Introduction

Heavy-ion inertial fusion (HIF), which is an inertial confinement fusion (ICF) scheme driven by heavy-ion-beam (HIB), is a hopeful way to achieve fusion energy release [1][2]. A direct driven HIF fuel pellet commonly consists of a void core, a fuel layer, an ablator layer, and a tamper layer. HIBs irradiate the fuel pellet, and deposit the major part of kinetic energy to the ablator layer. The ablator layer is heated by the irradiation of HIBs to a dense plasma state then expands and compresses the fuel. High temperature and low fuel density area surrounded by a cold high-density fuel is formed in the center of fuel pellet. The high energy particles created by ignition in the central high-temperature area heat the surrounding dense fuel, a substantial portion of the fuel reacts to release energy.

Modification of fuel pellet structure is an effective way to increase the irradiation uniformity [3] and areal density during implosion [4]. The purpose of this study is to compare the effects of fuel pellet structural modification of flower-shape tamper [3][4] under the condition of different numbers of HIBs.

2. Governing equation and calculation condition

We used a two-dimensional cylindrical Euler fluid with ideal gas equation-of-state (EOS) as our simulation model. The governing equations are as follows:

$$\frac{\partial \rho}{\partial t}+\frac{1}{r}\frac{\partial (r\rho u_{\mathrm{r}})}{\partial r}+\frac{\partial (\rho u_{\mathrm{z}})}{\partial z}=0 \tag{1}$$

$$\begin{aligned}&\frac{\partial u_{\mathrm{r}}}{\partial t}+u_{\mathrm{r}}\frac{\partial u_{\mathrm{r}}}{\partial r}+u_{\mathrm{z}}\frac{\partial u_{\mathrm{r}}}{\partial z}+\frac{1}{\rho}\frac{\partial \left(P_{\mathrm{i}}+P_{\mathrm{e}}+Q_{\mathrm{ir}}+Q_{\mathrm{er}}\right)}{\partial r}=0\\ &\frac{\partial u_{\mathrm{z}}}{\partial t}+u_{\mathrm{r}}\frac{\partial u_{\mathrm{z}}}{\partial r}+u_{\mathrm{z}}\frac{\partial u_{\mathrm{z}}}{\partial z}+\frac{1}{\rho}\frac{\partial \left(P_{\mathrm{i}}+P_{\mathrm{e}}+Q_{\mathrm{iz}}+Q_{\mathrm{ez}}\right)}{\partial z}=0\end{aligned} \tag{2}$$

$$\begin{aligned}&\left(\frac{\partial T_{\mathrm{i}}}{\partial t}+u_{\mathrm{r}}\frac{\partial T_{\mathrm{i}}}{\partial r}+u_{\mathrm{z}}\frac{\partial T_{\mathrm{i}}}{\partial z}\right)+\frac{P_{\mathrm{i}}}{\rho C v_{\mathrm{i}}}\left(\frac{1}{r}\frac{\partial r u_{\mathrm{r}}}{\partial r}+\frac{\partial u_{\mathrm{z}}}{\partial z}\right)+\\ &\frac{1}{\rho C v_{\mathrm{i}}}\left(Q_{\mathrm{ir}}\frac{1}{r}\frac{\partial r u_{\mathrm{r}}}{\partial r}+Q_{\mathrm{iz}}\frac{\partial u_{\mathrm{z}}}{\partial z}\right)+\omega_{\mathrm{ie}}(T_{\mathrm{i}}-T_{\mathrm{e}})=0\\ &\left(\frac{\partial T_{\mathrm{e}}}{\partial t}+u_{\mathrm{r}}\frac{\partial T_{\mathrm{e}}}{\partial r}+u_{\mathrm{z}}\frac{\partial T_{\mathrm{e}}}{\partial z}\right)+\frac{P_{\mathrm{e}}}{\rho C v_{\mathrm{e}}}\left(\frac{1}{r}\frac{\partial r u_{\mathrm{r}}}{\partial r}+\frac{\partial u_{\mathrm{z}}}{\partial z}\right)\\ &+\frac{1}{\rho C v_{\mathrm{e}}}\left(Q_{\mathrm{er}}\frac{1}{r}\frac{\partial r u_{\mathrm{r}}}{\partial r}+Q_{\mathrm{ez}}\frac{\partial u_{\mathrm{z}}}{\partial z}\right)-\frac{\omega_{\mathrm{ie}}}{Z_{\mathrm{eff}}}(T_{\mathrm{i}}-T_{\mathrm{e}})\\ &=\frac{\Delta E_{\mathrm{free}}+\Delta E_{\mathrm{bound}}}{\rho C v_{\mathrm{e}}\Delta V}.\end{aligned} \tag{3}$$

Here, ρ is the density, T_{i} and T_{e} are the temperatures of ions and electrons, Q_{ir} and Q_{iz} are the artificial viscosities of ions in the *r*- and *z*-directions, Q_{er} and Q_{ez} are the artificial viscosities of electrons in the *r*- and *z*-directions, Cv_{i} and Cv_{e} are the ion and electron heat capacities, P_{i} and P_{e} are the ion and electron pressures, ω_{ie} is the ion-

electron collision frequency, Z_{eff} is the effective charge of the ion, ΔE_{free} and $\Delta E_{\mathrm{bound}}$ are the deposition energies to free and bound electrons, and ΔV is the cell volume, respectively.

We used CIP (constrained interpolation profile) [5] method with MmB (local maximum and minimum bounds) [6] correction to calculate the advection terms of the governing equations. For the non-advection terms of governing equations, we used central difference method. We set the mesh grids at 300 × 300 points. For numerical stability, we used an artificial viscosity [7] with splitting method [8]. We calculated the ionization states by Saha equation for local thermal equilibrium state [9].

We calculated energy deposition from incident HIBs in two parts: Coulomb interactions of incident ions with bound and free electrons of fuel pellet. For energy deposition to bound electrons, we used the Bethe–Bloch and LSS theories, and for energy deposition to free elections, we used the Jackson plasma binary and collective theory [10].

3. Fuel pellet structure and irradiation configuration

A conventional spherical fuel pellet is shown in Fig.1. Figure 1(a) shows the fuel pellet structure at each layer. Figure 1(b) shows the fuel pellet with 4 incident HIBs in the calculation area, which is referred to the "4-beam type". The shaded red areas indicate the areas covered by the incident HIBs. Figure 1(c) shows the fuel pellet with 6 incident HIBs in the calculation area, which is referred to the "6-beam type". A mixture of D (deuterium) and T (tritium) was used as the fuel. For the fuel pellet composition, we used a core of low-density DT gas, a DT ice as fuel layer, an aluminum ablator layer, and a lead tamper layer, respectively.

We proposed the structural modification of fuel pellet with a flower-shape tamper for the normal spherical fuel pellet [3][4]. The flower-shape tamper modification was converting the spherical tamper to a flower-shape tamper as is shown in Figs.2 and 3. Figure 2(a) shows the 4-beam type fuel pellet and (b) shows the pellet with the incident HIBs. Figure 3(a) shows the 6-beam type fuel pellet and (b) shows the pellet with the incident HIBs.

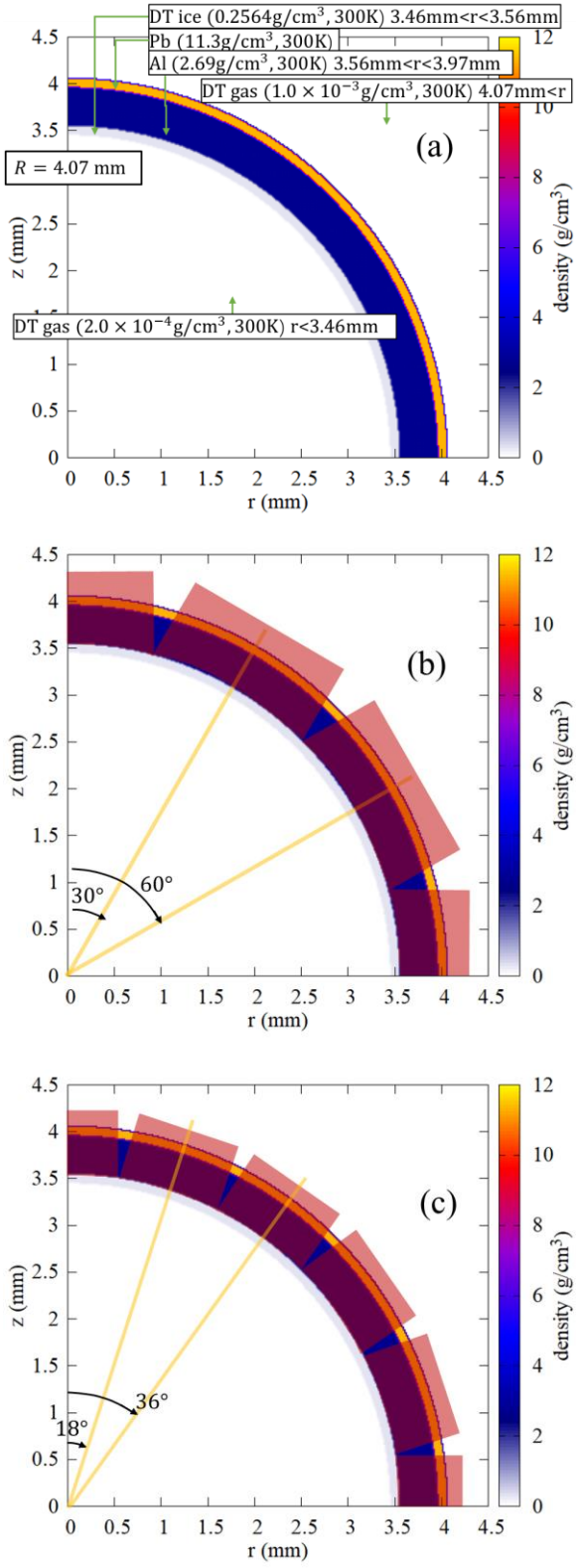

Fig. 1 Conventional spherical fuel pellet. (a) each layer, (b) with 4-beam type incident HIBs, and (c) with 6-beam type incident HIBs.

In this paper, the curvature of tamper is referred as "R". In Fig.2, the curvature of tamper petal was $R = 2.47$ mm, and in Fig.3 the curvature of tamper petal was $R = 1.47$ mm. When $R = 4.07$ mm, the tamper is a uniform thickness shell of fuel pellet, i.e., the tamper is a conventional spherical tamper as shown in Fig.1, and any tamper with R smaller than 4.07 mm is a flower-shape tamper.

The thicknesses from outer edge of tamper to the inner edge of ablator are different at the different parts of the incident HIB as shown in Fig. 4, which causes energy deposition non-uniformity of Bragg-peak area. To compensated this difference, we proposed the modification of flower-shape tamper in Figs.2 and 3 [3][4].

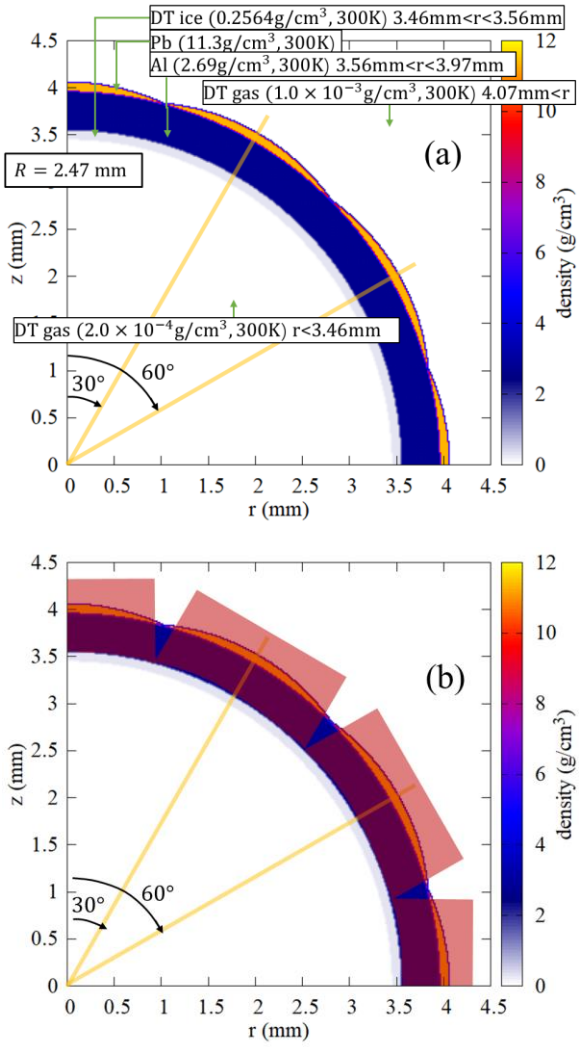

Fig. 2 Fuel pellet with the modification of flower-shape tamper for 4-beam type HIBs irradiation. (a) at each layer and (b) with incident HIBs.

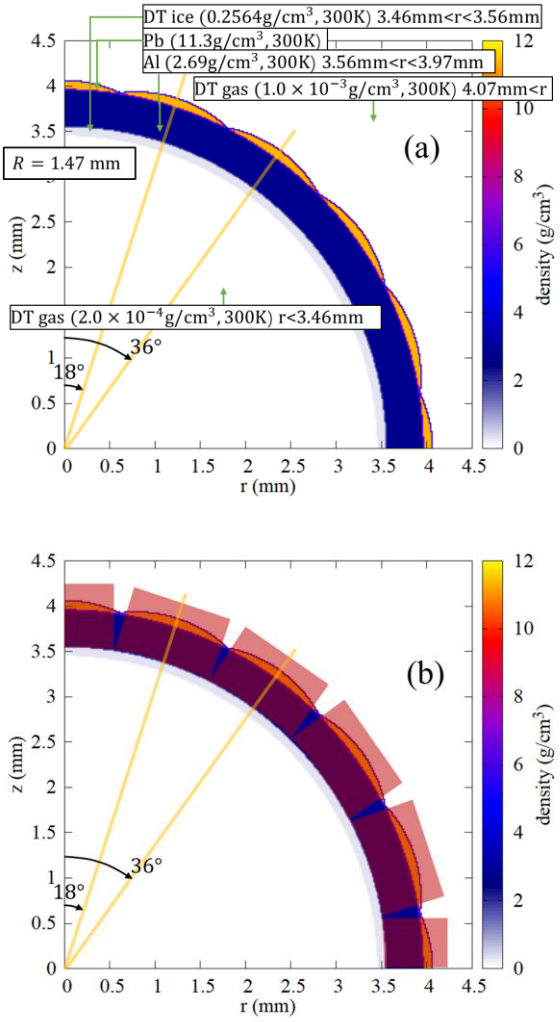

Fig. 3 Fuel pellet with the modification of flower-shape tamper for 6-beam type HIBs. (a) at each layer and (b) with incident HIBs.

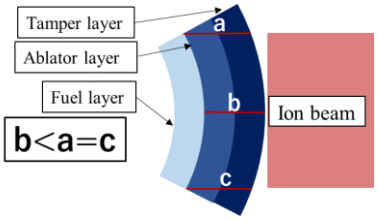

Fig. 4 Ion beam irradiating target with tamper layer. At the edge of the incident HIB, the thickness from outer edge of tamper to the inner edge of ablator is a or c, whereas at the center of the incident HIB, the thickness is b, and b < a = c.

We used Pb^{+} with 11.3 GeV of kinetic energy as the incident HIBs. The Bragg peak of incident ion was near the inner edge of the ablator. The incident HIBs has a uniform transverse particle distribution [11]. The beam radius of 4-beam type was 0.92 mm, and the beam radius of 6-beam type was 0.56 mm.

To covers the whole surface of fuel pellet, 46 HIBs were required in 4-beam type, and 127 HIBs were required in 6-beam type. The total irradiation power was 545 TW, and the total energy of the HIBs was 2.7 MJ. The total irradiation power history is shown in Fig. 5. The irradiation duration was 5 ns. The beam current and power per beam were 1 kA and 11.8 TW, respectively.

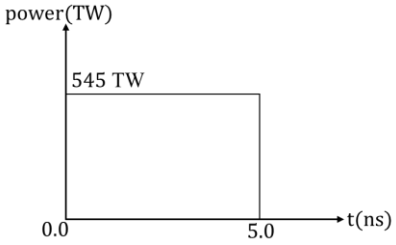

Fig. 5 Irradiation power history.

4. Results

Figure 6 shows the energy deposition distributions for 4-beam type at 1.0 ns. Figure 6(a) shows the distribution for the conventional fuel pellet with the 4-beam type irradiation. Figure 6(b) shows the distribution for the fuel pellet with flower-shape tamper with $R = 3.77$ mm in the 4-beam type irradiation. Figure 7 shows the density distribution of 4-beam type at 1.0 ns. Figure 7(a) and (b) show the corresponding density distribution to Fig.6(a) and Fig.6(b), respectively.

Figure 8 shows the energy deposition distributions for 6-beam type at 1.0 ns. Figure 8(a) shows the distribution for the conventional fuel pellet by the 6-beam type irradiation. Figure 8(b) shows the distribution for the fuel pellet with flower-shape tamper $R = 3.77$ mm by 6-beam type irradiation. Figure 9 shows the density distribution for the 6-beam type at 1.0 ns. Figure 9(a) and (b) show the corresponding density distribution to Fig.8(a) and Fig.8(b), respectively.

Figure 10 shows the areal density history of DT with different tamper petal radius. The areal density is the average areal density of simulation area where the ion temperature bigger than 500 eV. Figure 10(a) shows the areal density time history of 4-beam type pellet, and Fig.10(b) shows the areal density time history of 6-beam type pellet. Figure10 shows that in 4-beam type pellet, the modification of flower-shape tamper increased the maximum areal density during implosion, whereas in 6-beam type pellet, the modification of flower-shape tamper decreased the

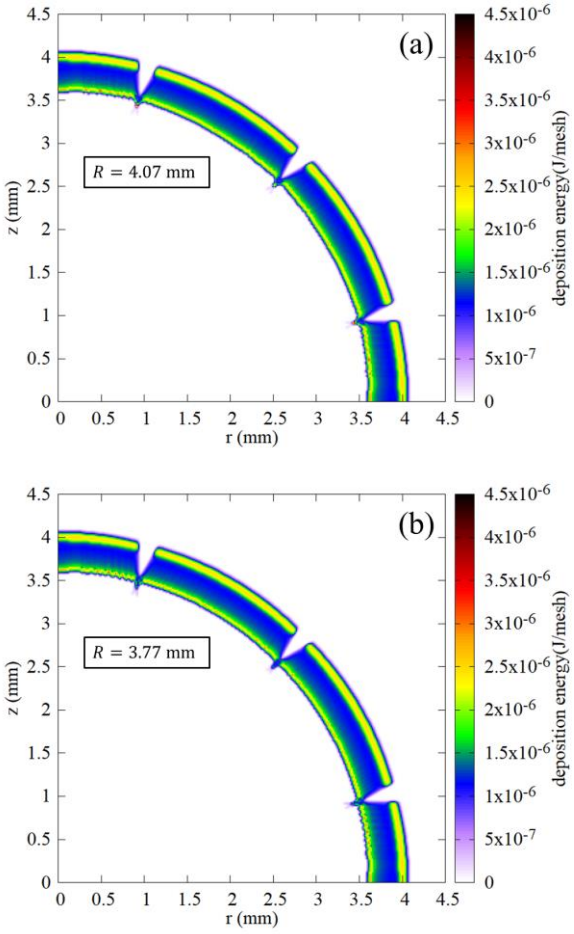

Fig. 6 Energy deposition distributions at 1.0 ns for 4-beam type irradiation, (a) for tamper petal radius $R = 4.07$ mm and (b) for tamper petal radius $R = 3.77$ mm.

maximum areal density during implosion. The maximum areal density of conventional fuel pellet in 6-beam type is smaller than 4-beam type, which is attributed to the uniform transverse particle distribution of incident HIBs. Due to the uniform

transverse particle distribution of incident HIBs, the uniformity in the area irradiated by the incident HIBs is high, the nonuniformity during implosion mainly caused by the unirradiated area of the incident HIBs, and the unirradiated area in 6-beam type is bigger than the unirradiated area in 4-beam type.

We defined the RMS irradiation nonuniformity in the circumferential direction during the HIB irradiation as follows:

$$\sigma_{\mathrm{RMS}} = \sum_{1}^{n_{\max}} W_n \, \sigma_{\mathrm{rms}n} \tag{4}$$

$$W_n = \frac{E_n}{\sum_{1}^{n_{\max}} E_n} \tag{5}$$

$$\sigma_{\mathrm{rms}n} = \sum_{k_{\min}}^{k_{\max}} w_k \, \sigma_{\mathrm{rms}n}^{k} \tag{6}$$

$$w_k = \frac{E_n^k}{\sum_{k_{\min}}^{k_{\max}} E_n^k} \tag{7}$$

$$\sigma_{\mathrm{rms}n}^{k} = \frac{1}{\langle E \rangle_k} \sqrt{\frac{\int_0^{\pi/2} (\langle E \rangle_k - E_k(\theta))^2 \, \mathrm{d}L(\theta)_k}{\int_0^{\pi/2} \mathrm{d}L(\theta)_k}} \tag{8}$$

Here, σ_{RMS} is the RMS irradiation nonuniformity in whole irradiation duration, $n_{\max}$ is the time step of maximum irradiation time, i.e., the time step of 5.0 ns, W_n is the weighting of RMS irradiation nonuniformity at the nth time step, $\sigma_{\mathrm{rms}n}$ is the RMS irradiation nonuniformity at the nth time step, E_n is the total energy deposition from HIBs at the nth time step. We divided the fuel pellet into spherical shell layer with the thickness of mesh size. E_n^k is the energy deposition from HIBs to the kth shell of fuel pellet at the nth time step. $\sigma_{\mathrm{rms}n}^{k}$ is the RMS irradiation nonuniformity in the kth shell of fuel pellet at the nth time step, $k_{\min}$ is the shell layer number of the deepest part irradiated by HIBs in fuel pellet, $k_{\max}$ is the shell layer number of the surface of fuel pellet, w_k is the weighting of RMS irradiation nonuniformity at the kth shell. The simulation area is a quarter of a circle, which has the radian of $\pi/2$. As the results, Eq.(8), i.e., the definition equation of $\sigma_{\mathrm{rms}n}^{k}$ was calculated from the radian of 0 to the radian of $\pi/2$. $\langle E \rangle_k$ is the average energy deposition from HIBs to the kth shell, $E_k(\theta)$ is the energy deposition from HIBs to the kth shell at the area with the angle of θ, $\mathrm{d}L(\theta)_k$ is the arc length in the kth shell at the area with the angle of θ.

Figure 11 shows the RMS irradiation nonuniformity of different fuel pellet. Figure 11 shows that in either

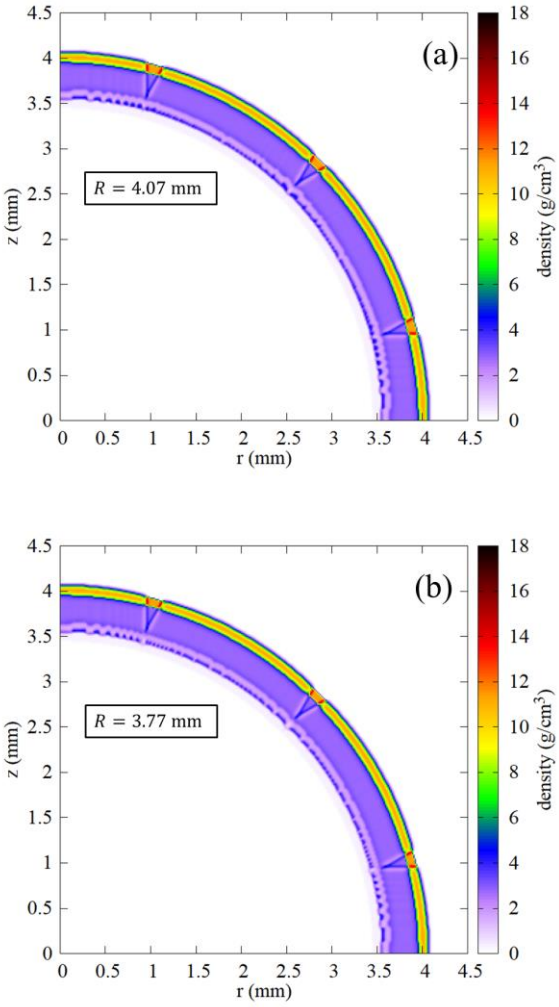

Fig. 7 Density distributions at 1.0 ns for 4-beam type irradiation, (a) for tamper petal radius R = 4.07 mm and (b) for tamper petal radius R = 3.77 mm.

4-beam type or 6-beam type, flower-shape tamper decreased the irradiation nonuniformity, and in either 4-beam type or 6-beam type, the RMS irradiation nonuniformity is a small value, which is attributed to the uniform transverse particle distribution of incident HIBs. Whereas in Fig.10, the flower-shape tamper decreased the maximum areal density during implosion in 6-beam type, which is opposite to the RMS irradiation nonuniformity in 6-beam type. As the results, besides irradiation nonuniformity, there are other factors besides irradiation nonuniformity that affect areal density during implosion.

5. Conclusion

The fuel pellet modification of flower-shape tamper had opposite effects to areal density of fuel during implosion in 4-beam type and 6-beam type. In 4-beam type, the areal density of fuel increased by the modification of flower-shape tamper, whereas in 6-beam type, the areal density of fuel decreased by the modification of flower-shape tamper. Either 4-beam type or 6-beam type, the modification of flower-shape tamper decreased the RMS irradiation nonuniformity.

As the results, there are other factors besides irradiation nonuniformity that affect areal density during implosion. In the following study, we will analyze implosion wave pattern and reduce the non-physical nonuniformity of energy deposition due to mesh effects.

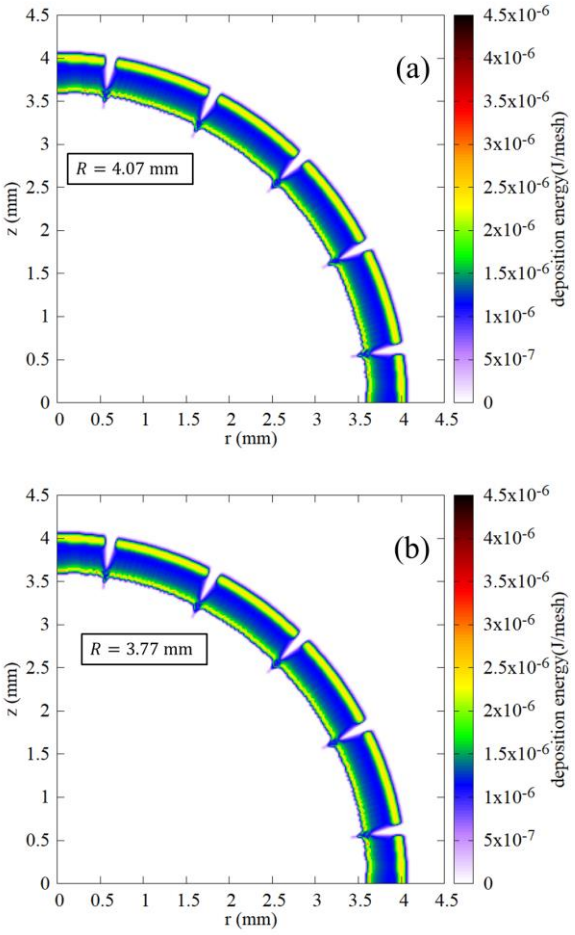

Fig. 8 Energy deposition distributions at 1.0 ns for 6-beam type irradiation, (a) for tamper petal radius R = 4.07 mm and (b) for tamper petal radius R = 3.77 mm.

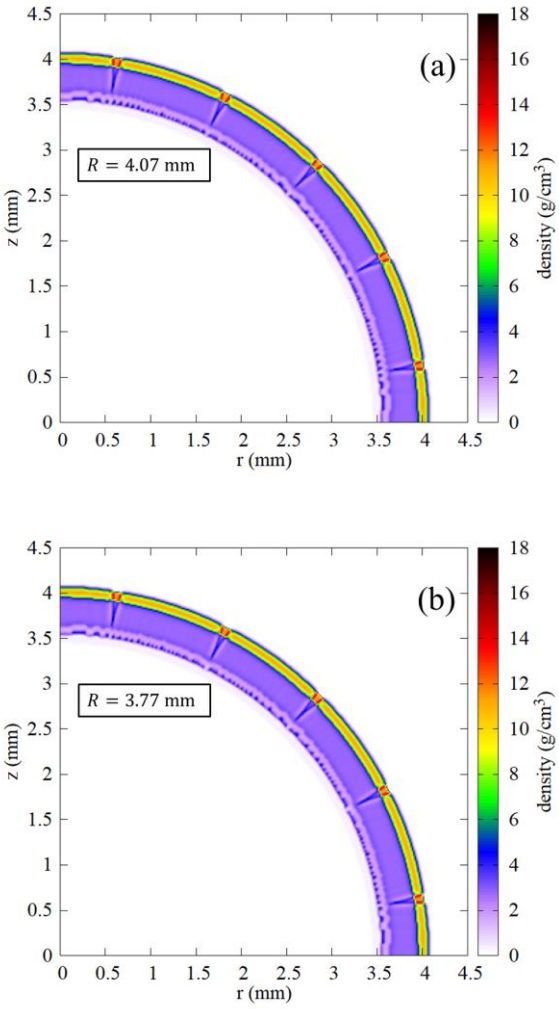

Fig. 9 Density distributions at 1.0 ns for 6-beam type irradiation, (a) for tamper petal radius R = 4.07 mm and (b) for tamper petal radius R = 3.77 mm.

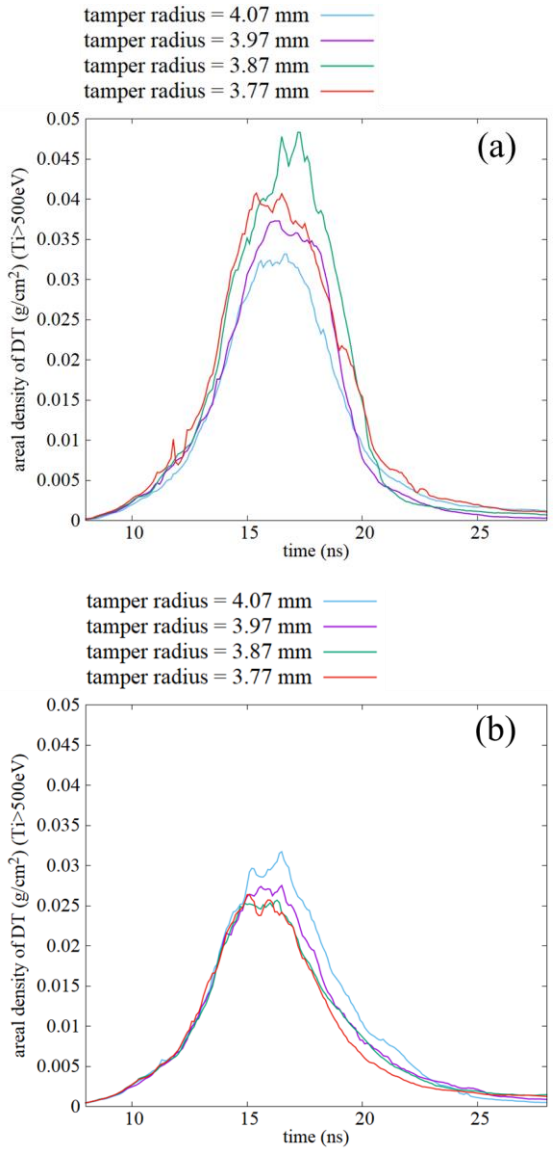

Fig. 10 Areal density of DT fuel for fuel pellet with different tamper petal radius. (a) 4-beam type; (b) 6-beam type.

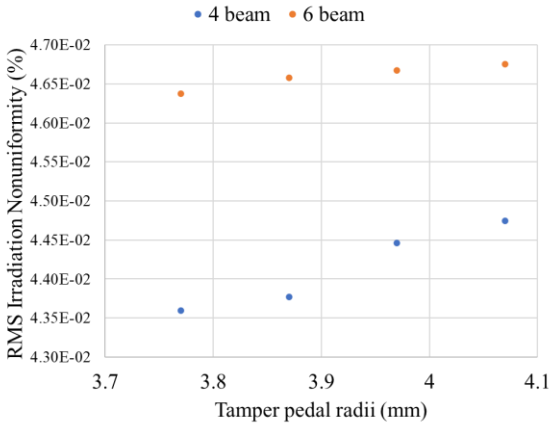

Fig. 11 RMS irradiation nonuniformity of different fuel pellet.

References

[1] K. Horioka, "Progress in particle-beam-driven inertial fusion research: Activities in Japan", *Matter Radiat. Extremes.* 3, pp.12-27 (2018).

[2] S. Kawata, "Direct-drive heavy ion beam inertial confinement fusion: a review, toward our future energy source", *Advances Phys. X.* 6, 1873860 (2021).

[3] Z. Lin, *et al*., "Reduction of Energy Deposition Non-Uniformity by Adjustment of Pellet Structure for Heavy-Ion-Beam Inertial Confinement Fusion", *Plasma Fusion Res.* 17, 2404064 (2022).

[4] Z. Lin, *et al*., in preparation.

[5] T. Yabe, "The Constrained Interpolation Profile Method for Multiphase Analysis", *J. Comput. Phys.* 169, 556–593 (2001).

[6] H. Wu and S. Yang, "MmB-A New Class of Accurate High Resolution Schemes for Conservation Laws in Two Dimensions", *IMPACT of Computing in Science and Engineering.* 1, 217-259 (1989).

[7] V. F. Kuropatenko, "On Difference Methods for the equations of hydrodynamics", *Amer. Math. Soc., Providence*. 116 (1967).

[8] D. S. Miller, "Splitting shock heating between ions and electrons in an ionized gas", *Comput. Fluids*. 210, 104672 (2020).

[9] J. W. Fowler, “Saha Equation Normalized to Total Atomic Number Density”, https://arxiv.org/abs/1209.1111 .

[10] T. A. Mehlhorn, “A finite material temperature model for ion energy deposition in ion-driven inertial confinement fusion targets”, *J. Appl. Phys*. 52, 6522 (1981).

[11] T. Kikuchi, “Beam dynamics and emittance growth during final beam bunching in HIF driver systems”, et al, *Nucl. Instrum. Methods. Phys. Res. A*. 544 262–267 (2005).

Relationship between required tritium amount contributing parameters in power generation system for heavy-ion inertial fusion

KAZUMA Takumi, TAKAHASHI Kazumasa, SASAKI Toru, KIKUCHI Takashi

Nagaoka Univ. Tech.

ABSTRACT

In a heavy-ion inertial fusion power plant, we researched on required tritium amount with parameters in a system analysis. The tritium amount required per time and per shot were estimated using the system analysis. The parameters contributing to the required tritium amount were evaluated in a rate of change of tritium amount relative to the rate of change of the parameters.

Keywords

Heavy-ion Inertial Fusion, Required Tritium Amount, Power Plant, Steam Turbine System Efficiency

1. Introduction

Heavy-ion inertial fusion (HIF) power generation is expected to be a new power generation method without fossil fuel requirement [1]. Figure 1 shows a system model for inertial confinement fusion power plant. A HIF power plant consists of many components, and the relationship between each component is unknown [2]. In this study, we focused on amount of tritium required in the power plant operation as one of the many parameters for the HIF power generation system.

2. System Model

For the system analysis, a system model of the HIF power plant was developed as shown in Fig.1. The parameter calculations were performed under the condition of a net electrical power output of 1 GWe from the power plant. In this system model, it was assumed that the fuel pellet is irradiated with a heavy-ion beams and imploded. The generated fusion output

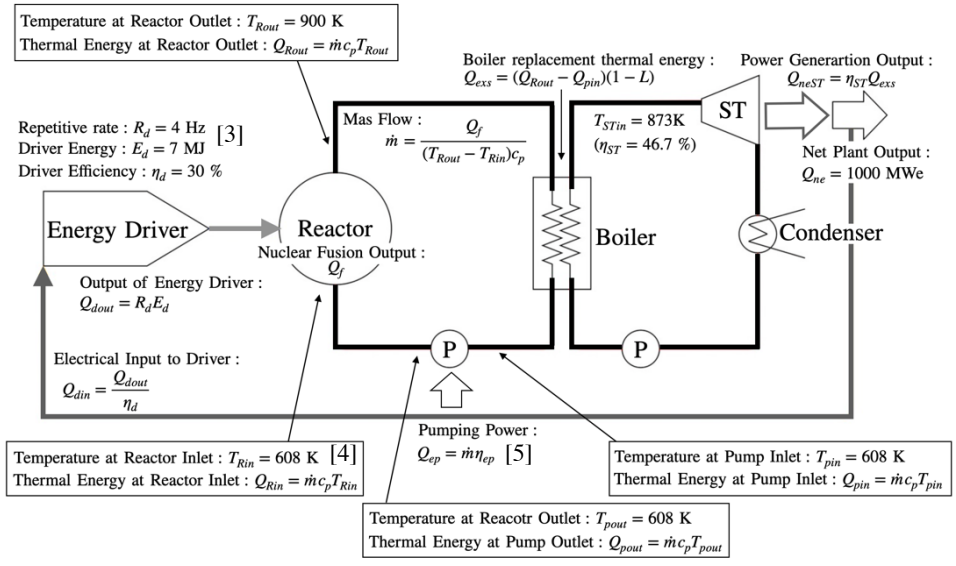

Fig.1 System model for inertial fusion power plant Power

energy is recovered as thermal energy to heat the coolant. The heated coolant boils water in a boiler and operates a steam turbine to generate electricity. A portion of the electrical power output is used to drive the heavy ion beam.

3. Results

Figures 2, 3, 4 and 5 show the amount of tritium required per time in each parameter changes. Figure 2 shows the tritium amount per time as a function of system efficiency η_{ST} for a steam turbine. The higher system efficiency of the steam turbine causes smaller fusion output power required to achieve the net power output of 1 GWe. As a result, the less amount of tritium is required because of the lower requirement for the fusion output power.

Figure 3 shows the amount of tritium per time as a function of energy driver efficiency η_d. The higher driver efficiency causes smaller fusion output power required to achieve the net electrical power output. As a result, the less amount of tritium is required because of the lower requirement of for the fusion power.

Figure 4 shows the tritium amount per time as a function of driver output energy E_d. The higher the driver output energy requires greater electrical input to the driver. The fusion output power required to achieve the net electrical power output was increased to compensate the increase. As a result, the amount of tritium required is also increased.

Figure 5 shows the tritium amount per time as a function of driver repetitive rate R_d. A higher repetitive rate increases the electrical input to the driver per time. This requires an increase in the fusion output power required to achieve the net power output. As a result, the amount of tritium required is also increased.

The change in tritium amount per time at each parameter is shown in Table 1. The effect of each parameter on tritium was evaluated by the required tritium amount ratio, which is calculated by Eq. (1). The large ratio means that the effect on tritium amount is large, while the small ratio means that the effect on tritium amount is small.

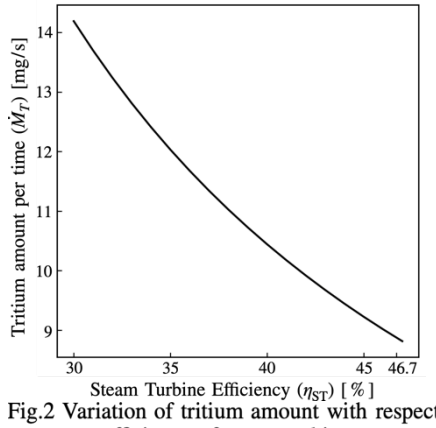

Fig.2 Variation of tritium amount with respect to system efficiency of steam turbine

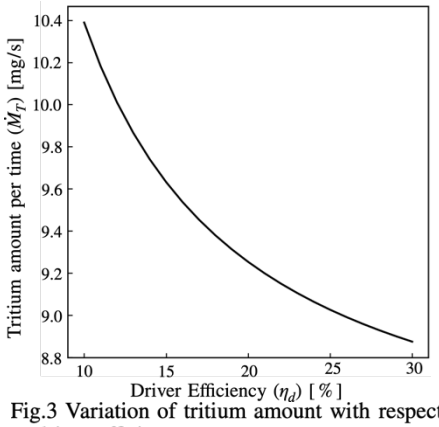

Fig.3 Variation of tritium amount with respect to driver efficiency

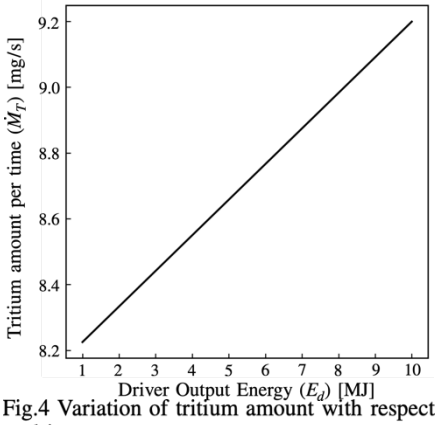

Fig.4 Variation of tritium amount with respect to driver output energy

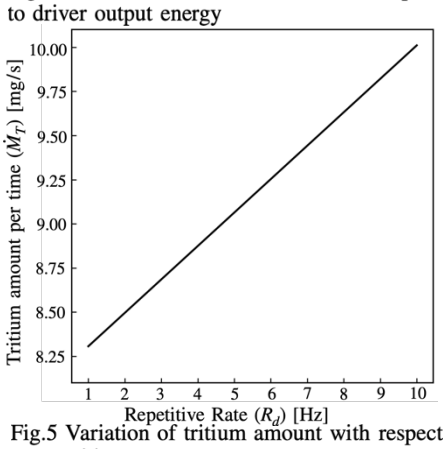

Fig.5 Variation of tritium amount with respect to repetitive rate

$$R_{\mathrm{RTA}} = \frac{(M_{Tmax} - M_{Tmin})/M_{Tave}}{(x_{max} - x_{min})/x_{ave}} \quad (1)$$

Here, M_{Tmax}, M_{Tmin}, and M_{Tave} are the maximum, minimum, and average amounts of tritium required, respectively. x_{max}, x_{min}, and x_{ave} are the maximum, minimum, and average values of the parameters, respectively.

Table 1 Tritium amount required per time

	η_{ST} = 30~46.7%	η_{d} = 10~30%	E_{d} = 1~10MJ	R_{d} = 1~10Hz
M_{Tmin} [mg/s]	9.02	8.87	8.23	8.31
M_{Tmax} [mg/s]	14.2	10.4	9.20	10.0
$M_{\mathrm{Tmax}} - M_{\mathrm{Tmin}}$ [mg/s]	5.18	1.53	0.97	1.69
R_{RTA}	1.10	0.162	0.0683	0.114

Table 1 shows that the amount of tritium required is from 8 to 14 mg, and that the most influential of the four parameters on the amount of tritium is the system efficiency of the steam turbine, while the least influential is the driver output energy.

4. Conclusions

In the HIF power plant, we researched on the required tritium amount with parameters in the system analysis. The tritium amount required per time and per shot were estimated using the system analysis. The parameters contributing to the required tritium amount were evaluated in the ratio of change of tritium amount relative to the rate of change of the parameters. The evaluation of the required tritium amount ratio revealed that η_{ST} had the greatest impact on the tritium amount, while E_d had the least impact.

References

[1] K. HORIOKA, "Progress in Particle-Beam-Driven Inertial Fusion Research: Activities in Japan", *Matter Radiation Extremes* **3**. 12 (2018)

[2] A. INOUE *et al*., "Comparative Study on Cost Evaluation and Network Visualization of Particle Accelerator Components for Heavy Ion Inertial Fusion", *J. Phys.: Confs. Ser*. **717**, 012097 (2016).

[3] T. KIKUCHI and Nob. HARADA, "Low Pellet Gain and High Efficiency ICF Power Plant Model by MHD Power Generation", Proc. 13th Intr. Confs. High-Power Part. Beams (Beams2000), 838 (2000)

[4] M. NISHIKAWA, *et al*., "The Frontiers of Research on Fusion Blanket Technology", *J. Plasma Fusion Res*., vol.79, No.7, 681 (2003)

[5] Y. CHIKAZAWA, *et al*., *JAEA Research*, 30 (2006)

Study on Injection Velocity of Fuel Pellet into Reactor for Heavy-Ion Inertial Fusion

Takashi Kikuchi, Kazumasa Takahashi, Toru Sasaki, and Mayuko Koga*

Nagaoka University of Technology
** University of Hyogo*

ABSTRACT

We investigated numerically an injection velocity required by heat conduction in a fuel pellet for heavy-ion inertial fusion. A numerical scheme was studied for the heat conduction calculation for the fuel pellet in the reactor chamber. The calculation result showed the time for melting of solid fuel. The required injection velocity was evaluated with the time for melting of solid fuel by determining the chamber radius. The differences on the temperature distribution history were not observed from the viewpoint of the gas pressure in the reactor chamber. It was found that the temperature distribution history depends on the target structure from the comparison of the calculation results. The lower injection velocity is required for a target pellet in heavy-ion inertial fusion, because a target structure for heavy-ion inertial fusion has tamper and foam layers and the heat conduction is interfered by the layers.

Keywords

Heavy–Ion Inertial Fusion, Fuel Pellet Injection, Injection Velocity, Reactor Chamber, Background Gas Pressure

1 Introduction

A heavy-ion inertial fusion (HIF) system is one of candidates of inertial confinement fusion (ICF) [1, 2]. Heavy-ion beams illuminate a fuel target in a reactor chamber, and heated up the irradiated fuel target. In the fuel target, which consists of other structural materials and deuterium (D) and tritium (T) as a fuel for nuclear fusion reactions , ablation plasma is generated due to the heavy-ion beam irradiation, and the fuel is compressed into the center of target by the ablation plasma. Dense fuel core with high temperature is formed at the target center, and the nuclear energy is released by the nuclear fusion reactions.

Figure 1 shows typical operation for the ICF scheme and typical situation of a fuel pellet in the ICF reactor [1, 2]. The fuel pellet is repeatedly injected into the reactor chamber with several Hz. The fuel pellet is illuminated by several numbers

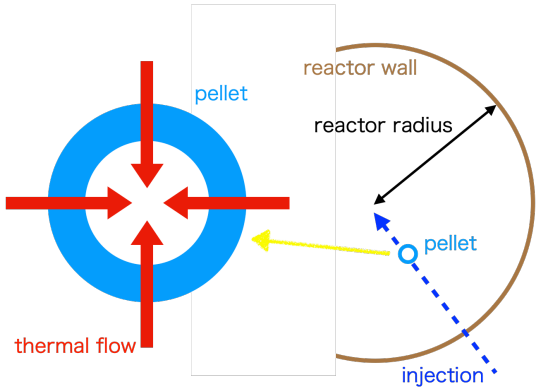

Figure 1: Typical ICF operation and situation of fuel pellet in ICF reactor.

of the intense laser and the intense ion beam. For this reason, the position of fuel pellet should be controlled accurately at the designated one at each shot [3–5]. On the other hand, it is difficult to control the injection into designated position in the reactor at each shot with higher injection velocity. The fuel pellet is heated by the thermal conduction from the background gas in the reactor chamber. As a result, the lower injection velocity of the fuel pellet causes the melting of solid fuel in the fuel pellet, because the long time flight with the lower injection velocity gives the time for melting the low-temperature solid fuel.

It is expected that the heat conduction in the fuel pellet depends on the several factors such as the gas pressure and the gas temperature in the reactor chamber, the fuel pellet structure, and so on. In this study, we investigated numerically the injection velocity required from the viewpoint of the melting of the solid DT fuel and the heat conduction with the several conditions. The numerical scheme was studied for the heat conduction calculation in the fuel pellet, and the calculation conditions were assumed by the two types of fuel targets for a laser driven ICF and HIF in the reactor chamber conditions.

2 Calculation Method for Heat Conduction

The thermal diffusion equation was obtained by

$$\rho c_v \frac{\partial T}{\partial t} = \nabla \cdot (\kappa \nabla T) \,, \tag{1}$$

where ρ is the density, c_v is the specific heat, κ is the thermal conductivity, respectively. In a spherical coordinate, the time-dependent one-dimensional thermal diffusion equation in the radial direction was rewritten by

$$\rho c_v \frac{\partial T}{\partial t} = \frac{1}{r^2} \frac{\partial}{\partial r} \left(r^2 \kappa \frac{\partial T}{\partial r} \right) . \tag{2}$$

Figure 2 shows the computational model with the discretized grid and the arrangement of variables. We considered the discretization method for the thermal diffusion equation by five schemes based on explicit, semi implicit, and implicit methods for the temporal derivative.

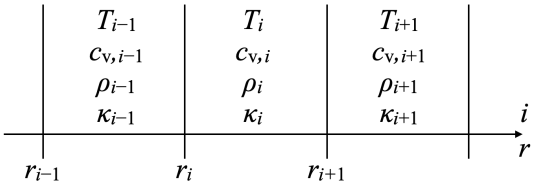

Figure 2: Computational model with arrangement of variables.

In the case of explicit method, the thermal diffusion equation was discretized by

$$\rho_i c_{v,i} \frac{T_i^{n+1} - T_i^n}{\Delta t} = \frac{1}{r_{i+1/2}^2 \Delta r} \left(r_{i+1}^2 \kappa_{i+1/2} \frac{T_{i+1}^n - T_i^n}{\Delta r} - r_i^2 \kappa_{i-1/2} \frac{T_i^n - T_{i-1}^n}{\Delta r} \right) . \tag{3}$$

Here n is the discretized time step index, i is the discretized spatial grid index, Δt is the discretized time step width, Δr is the discretized spatial grid interval, $r_{i+1/2} = (r_i + r_{i+1})/2$, $\kappa_{i+1/2} = (\kappa_i + \kappa_{i+1})/2$, and $\kappa_{i-1/2} = (\kappa_i + \kappa_{i-1})/2$, respectively. The above equation was rewritten by

$$T_i^{n+1} = T_i^n + \frac{\Delta t}{\rho_i c_{v,i} r_{i+1/2}^2 \Delta r^2} \Big[r_{i+1}^2 \kappa_{i+1/2} T_{i+1}^n - \left(r_{i+1}^2 \kappa_{i+1/2} + r_i^2 \kappa_{i-1/2} \right) T_i^n + r_i^2 \kappa_{i-1/2} T_{i-1}^n \Big] . \tag{4}$$

As well known criterion, the time step width was limited by $\Delta t \leq \Delta^2 / 2D$, where Δ is the spacial discrete width, and in this study,

$$\Delta t \leq \left[\frac{\rho_i c_{v,i} r_{i+1/2}^2 \Delta r^2}{r_{i+1}^2 \kappa_{i+1/2} + r_i^2 \kappa_{i-1/2}} \right]_{min} , \tag{5}$$

for the numerical stability.

DuFort-Frankel method is one of explicit schemes with unconditionally stable from the viewpoint of Von Neumann stability analysis [6]. However it is useful in the condition of $\Delta t / \Delta \ll 1$, because the discretized equation corresponds to the former diffusion equation for $\Delta t / \Delta \to 0$. In this study, it is difficult to satisfy the condition, because the ratio of the time step width to the spatial grid width was estimated as not enough small for the large time step width with the material properties.

In the case of semi-implicit method, the Crank-Nicolson method [7] was used as a well known

scheme, and the equation was given by

$$\rho_i c_{v,i}\frac{T_i^{n+1}-T_i^n}{\Delta t} = \frac{1}{2r_{i+1/2}^2\Delta r}\Big(r_{i+1}^2\kappa_{i+1/2}\frac{T_{i+1}^{n+1}-T_i^{n+1}}{\Delta r} - r_i^2\kappa_{i-1/2}\frac{T_i^{n+1}-T_{i-1}^{n+1}}{\Delta r} + r_{i+1}^2\kappa_{i+1/2}\frac{T_{i+1}^{n}-T_i^{n}}{\Delta r} - r_i^2\kappa_{i-1/2}\frac{T_i^{n}-T_{i-1}^{n}}{\Delta r}\Big). \quad (6)$$

The above equation was rewritten by

$$\left(1+\frac{r_{i+1}^2k_{i+1/2}\Delta t + r_i^2k_{i-1/2}\Delta t}{2r_{i+1/2}^2\Delta r^2\rho_i c_{v,i}}\right)T_i^{n+1} = \frac{r_{i+1}^2k_{i+1/2}\Delta t}{2r_{i+1/2}^2\Delta^2 r\rho_i c_{v,i}}T_{i+1}^{n+1} + \frac{r_i^2k_{i-1/2}\Delta t}{2r_{i+1/2}^2\Delta r^2\rho_i c_{v,i}}T_{i-1}^{n+1} + \frac{r_{i+1}^2k_{i+1/2}\Delta t}{2r_{i+1/2}^2\Delta r^2\rho_i c_{v,i}}T_{i+1}^{n} + \left(1-\frac{r_{i+1}^2k_{i+1/2}\Delta t + r_i^2k_{i-1/2}\Delta t}{2r_{i+1/2}^2\Delta r^2\rho_i c_{v,i}}\right)T_i^n + \frac{r_i^2k_{i-1/2}\Delta t}{2r_{i+1/2}^2\Delta r^2\rho_i c_{v,i}}T_{i-1}^{n}. \quad (7)$$

As a result, the time step width was not limited for the numerical stability. However larger time step width causes an oscillating solution as indicated as the term $\left(1-\frac{r_{i+1}^2k_{i+1/2}\Delta t+r_i^2k_{i-1/2}\Delta t}{2r_{i+1/2}^2\Delta r^2\rho_i c_{v,i}}\right)$ in Eq.(7).

The modified Crank-Nicolson method improves the convergence using the variables at three time levels such as T^{n+1}, T^n, and T^{n-1} [6]. Although the method was applied to the problem of our study and was checked in terms of numerical stability and accuracy, the merit was not found in this case.

In the case of implicit method, the equation was discretized by

$$\rho_i c_{v,i}\frac{T_i^{n+1}-T_i^n}{\Delta t} = \frac{1}{r_{i+1/2}^2\Delta r}\left(r_{i+1}^2\kappa_{i+1/2}\frac{T_{i+1}^{n+1}-T_i^{n+1}}{\Delta r} - r_i^2\kappa_{i-1/2}\frac{T_i^{n+1}-T_{i-1}^{n+1}}{\Delta r}\right). \quad (8)$$

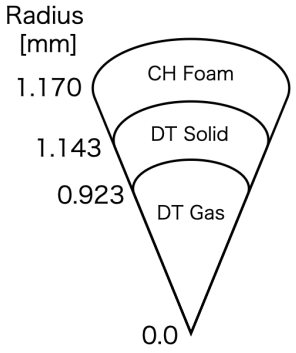

Figure 3: Fuel pellet model for laser driven ICF.

The above equation was rewritten by

$$\left(1+\frac{r_{i+1}^2\kappa_{i+1/2}\Delta t}{r_{i+1/2}^2\Delta r^2\rho_i c_{v,i}}+\frac{r_i^2\kappa_{i-1/2}\Delta t}{r_{i+1/2}^2\Delta r^2\rho_i c_{v,i}}\right)T_i^{n+1} = T_i^n + \frac{r_{i+1}^2\kappa_{i+1/2}\Delta t}{r_{i+1/2}^2\Delta r^2\rho_i c_{v,i}}T_{i+1}^{n+1} + \frac{r_i^2\kappa_{i-1/2}\Delta t}{r_{i+1/2}^2\Delta r^2\rho_i c_{v,i}}T_{i-1}^{n+1}. \quad (9)$$

As a result, the time step width was not limited for the numerical stability.

Based on the test calculation results with the above schemes, the implicit method with the Thomas tridiagonal algorithm for the matrix solver [8] was applied to the thermal diffusion equation due to the ability of the large time step with the convergence of solution in this study.

3 Calculation Condition for Heat Conduction in Fuel Pellet

As discussed in previous section, we demonstrated to calculate the heat conduction in fuel pellet for two conditions.

One of them was a fuel pellet for HIF scheme, which was assumed in Fig. 1 of Ref. [9]. The fuel pellet consist of DT gas, DT solid (fuel), Al pusher, Al foam, Al ablator, and Pb tamper layers. The temperature was assumed by 10 K at the initial condition.

Figure 3 shows the fuel pellet model for a laser driven ICF, which was designed for the LIFT project [10]. The fuel pellet consist of DT gas, DT solid (fuel), CH foam layers, respectively. The temperature was assumed by 10 K at the initial condition.

The outer layer of the fuel pellet was assumed by the air as the background gas in the reactor

chamber. The temperature was assumed by 1500 K, and the density was given by the equation-of-state for the ideal gas at each gas pressure. The pressure was required less than 100 Pa [11] in the reactor design for laser driven ICF. The pressure was required by 1 Pa for the laser driven ICF with fast ignition scheme [12]. In the case of HIF reactor, the gas pressure was determined by the modes of heavy-ion beam propagation in the reactor chamber [13]. In our previous study [14], the mode of vacuum transport was assumed for the estimation of gas pressure, because of avoiding the various instabilities for heavy-ion beam propagation through the gas environment. The pressure was required in ranges of 0.01∼0.1 Pa [15] for the case of HIF. The background gas pressures in the reactor chamber were assumed by 0.1, 1, and 10 Pa for the laser fusion, by 0.01, 0.1, and 1 Pa for the HIF, respectively [14].

4 Calculation Result for Heat Conduction in Fuel Pellet

According to the conditions in the previous section, the temperature distribution history was calculated for the fuel pellet heated by the background gas in the ICF reactor chamber.

Figure 4 shows the temperature distribution history in DT solid layer of fuel pellet model for the laser fusion as shown in Fig. 3. As shown in Fig. 4, it was estimated that the solid fuel will be melted after 5.5 ms, because the triple point of D_2 is 18.7 K [16]. For this reason, it is estimated that the injection velocity of 545 m/s is required for the reactor chamber radius of 3 m. On the other hand, the differences on the temperature distribution history were not observed from the viewpoint of the gas pressure in the reactor chamber.

Figure 5 shows the temperature distribution history in DT solid layer of fuel pellet model for HIF. As shown in Fig. 5, it was estimated that the solid fuel will be not melted during 100 ms. For this reason, it is estimated that the injection velocity less than 30 m/s is required for the reactor chamber radius of 3 m. On the other hand, the differences on the temperature distribution history were not observed from the viewpoint of the gas pressure in the reactor chamber.

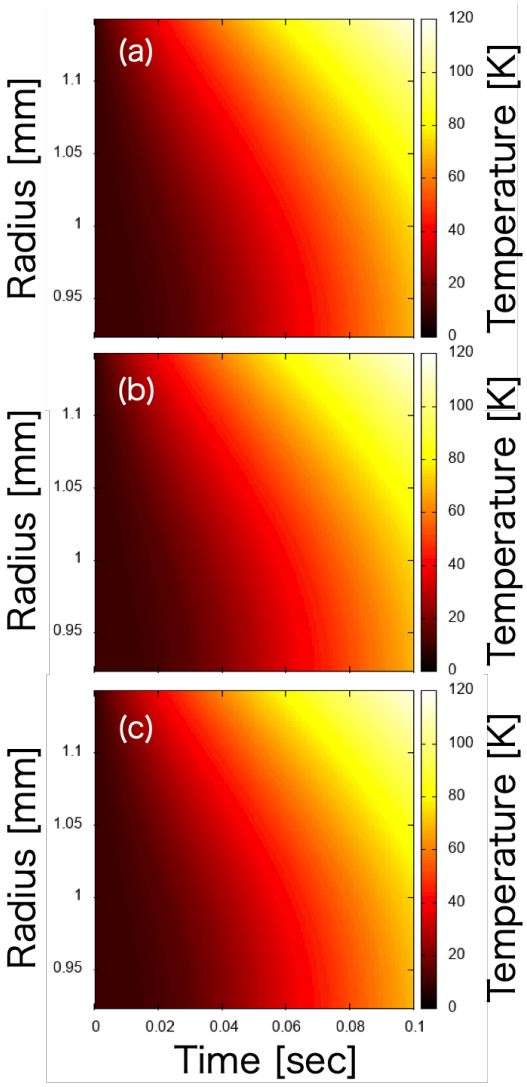

Figure 4: Temperature distribution history in DT solid layer of fuel pellet model for laser fusion, (a) for 0.1 Pa, (b) for 1 Pa, and (c) for 10 Pa of reactor gas pressure, respectively.

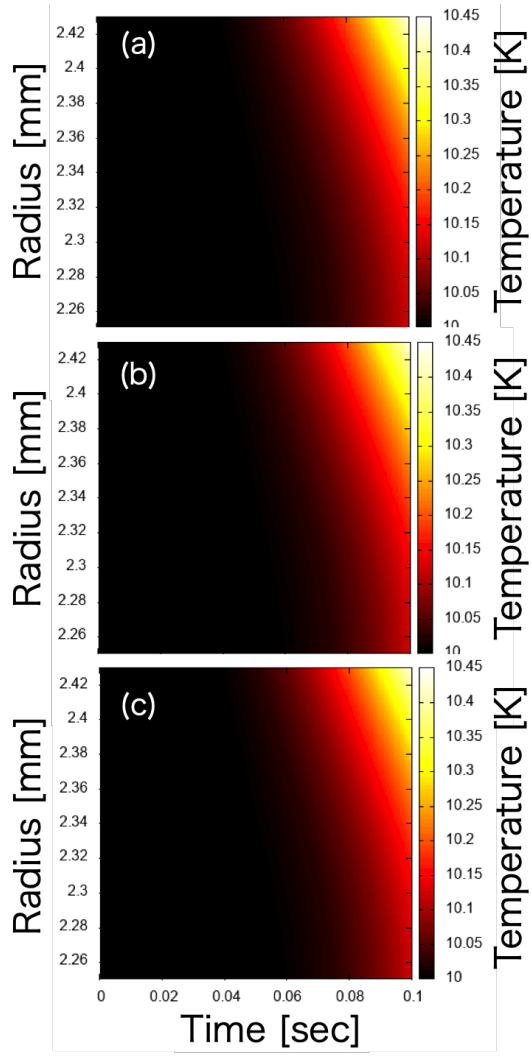

Figure 5: Temperature distribution history in DT solid layer of fuel pellet model for HIF, (a) for 0.01 Pa, (b) for 0.1 Pa, and (c) for 1 Pa of reactor gas pressure, respectively.

In comparisons with Fig. 4 and Fig. 5, it was found that the temperature distribution history depends on the target structure, not the gas pressure in the reactor chamber.

5 Conclusion

In this study, we investigated numerically the injection velocity required from the viewpoint of the melting of the solid DT fuel and the heat conduction with the several conditions. The numerical scheme was studied for the heat conduction calculation for the fuel pellet in the ICF reactor chamber, and the implicit method with the Thomas tridiagonal algorithm was applied to the thermal diffusion equation. The calculation conditions were assumed by the two types of fuel targets for the laser driven ICF and HIF in the reactor chamber conditions.

The calculation result showed that the time for melting of solid DT fuel was 5.5 ms for the target pellet in the LIFT. The time for melting of solid DT fuel was estimated as greater than 100 ms for the target pellet in the HIF. For the chamber radius of 3 m, the required injection velocities were evaluated by 545 m/s for the target pellet in the LIFT and 30 m/s or less for the target pellet in the HIF.

The differences on the temperature distribution history were not observed from the viewpoint of the gas pressure in the reactor chamber. It was found that the temperature distribution history depends on the target structure from the comparison of the calculation results for the two types of pellets.

The target structure for the direct-driven HIF has the tamper and the foam layers owing to the stopping power of heavy-ion beams in the target material. For this reason, the lower injection velocity is required for the target pellet in HIF, because the heat conduction is interfered by the layers. This is one of advantages for the operation of ICF power plant in HIF system.

Acknowledgment

The authors would like to thank Prof. Ryusuke TSUJI for useful information of injection velocity of target pellet.

References

[1] S. ATZENI and J. MEYER-TER-VEHN, *The Physics of Inertial Fusion: Beam Plasma Interaction, Hydrodynamics, Hot Dense Matter* (Oxford Univ., N.Y., 2004).

[2] S. PFALZNER, *An Introduction to Inertial Confinement Fusion (Series in Plasma Physics)* (CRC Press, 2006).

[3] E.I. VALMIANSKI, R.W. PETZOLDT, and N.B. ALEXANDER, *Fusion Sci. Tech.* **43**, pp.334∼338 (2003).

[4] T. NORIMATSU, K. NAGAI, T. TAKEDA, K. MIMA, and T. YAMANAKA, *Fusion Sci. Tech.* **43**, pp.339∼345 (2003).

[5] M. KOGA, S. UCHINO, E. MAEDA, K. YAMANOI, and A. IWAMOTO, *Plasma Fusion Res.* **17**, pp.2404052-1∼2404052-4 (2022).

[6] S. JARDIN, *Computational Methods in Plasma Physics (Computational Science Series)* (CRC Press, 2010).

[7] J. CRANK and P. NICOLSON, *Mathematical Proceedings of the Cambridge Philosophical Society* **43(1)**, pp.50∼67 (1947).

[8] R.W. HOCKNEY and J.W. EASTWOOD, *Computer Simulation Using Particles* (Taylor & Francis, 1988), pp.185∼186.

[9] N. WATANABE, K. TAKAHASHI, T. SASAKI, and T. KIKUCHI, *Plasma Fusion Res.* **17**, pp.2404086-1∼2404086-4 (2022).

[10] *Committee Report of Conceptual Design for Experimental Reactor of Laser Fusion with Fast Ignition*, p.48 (ILE, Osaka Univ. and IFE Forum, 2015) (in Japanese).

[11] W.R. MEIER, *Fusion Eng. Design* **89**, pp.2489∼2492 (2014).

[12] *Conceptual Design for Fast Ignition Laser Fusion Power Plant*, p.64 (ILE, Osaka Univ. and IFE Forum, 2006) (in Japanese).

[13] A.B. LANGDON, *Particle Accelerators* **37-38**, pp.175∼180 (1992).

[14] T. KIKUCHI, Y. UCHIDA, M. NAKAMURA, Y. KAJIMURA, K. HORIOKA, *NIFS-PROC* **123**, pp.85∼89 (2023).

[15] R.W. MOIR, *Fusion Tech.* **25**, pp.5∼25 (1994).

[16] L.A. SCHWALBE, *J. Phys. Chem. Ref. Data* **15**, pp.1351∼1356 (1986).

Publication List of NIFS-PROC. Series

NIFS-PROC-110
Edited by Jun Hasegawa and Tetsuo Ozaki
Resent Developments of Pulsed Power Technology and Plasma Application Research
Jan. 12, 2018

NIFS-PROC-111
Edited by Liqun HU, Shigeru MORITA and Yeong-Kook OH
Proceeding of A3 Foresight Program Seminar on Critical Physics Issues Specific to Steady State Sustainment of High-Performance Plasmas 12 - 15 December, 2017, Chongqing, China
Jun. 11, 2018

NIFS-PROC-112
Edited by E. Kikutani (KEK) and S. Kubo (NIFS)
Proceedings of the meeting on Archives in Fields of Natural Sciences in FY 2017
Oct. 18, 2018 (Written in Japanses)

NIFS-PROC-113
Pulsed Power and High-Density Plasma and its Applications
Edited by Koichi Takaki and Tetsuo Ozaki
Feb. 6, 2019

NIFS-PROC-114
The 7th Japan-China-Korea Joint Seminar on Atomic and Molecular Processes in Plasma (AMPP2018)
Edited by Daiji Kato, Ling Zhang, and Xiaobin Ding
May 10, 2019

NIFS-PROC-115
CFQS TEAM
NIFS-SWJTU JOINT PROJECT FOR CFQS -PHYSICS AND ENGINEERING DESIGN-
VER. 2.1 2019. SEP.
Nov. 8, 2019

NIFS-PROC-116
Satoshi Ohdachi, Editor of the Post-CUP Workshop proceeding
Collected papers at the 2019 Post-CUP Workshop & JSPS-CAS Bilateral Joint Research Projects Workshop, 24th-26th July, 2019, Nagoya, Japan
Feb. 21, 2020

NIFS-PROC-117
Edited by E. Kikutani (KEK) and S. Kubo (NIFS)
Proceedings of the meetings on Archives in Fields of Natural Sciences in FY2018
June. 9, 2020 (Written in Japanses)

NIFS-PROC-118
Edited by Tetsuo Ozaki and Sunao Katsuki
New Development of Beam Physics and the Application by New Generation Plused Power Technology
June. 29, 2020
National Institute for Fusion Science, National Institutes of Natural Sciences
Institute of Fusion Science, School of Physical Science and Technology, Southwest Jiaotong University

NIFS-PROC-119
Hefei Keye Electro Physical Equipment Manufacturing Co. Ltd.
NIFS-SWJTU JOINT PROJECT FOR CFQS -PHYSICS AND ENGINEERING DESIGN-
VER. 3.1 2020. NOV.
Jan. 25, 2021

NIFS-PROC-120
Edited by Izumi Tsutsui (KEK) and Shin Kubo (NIFS)
Proceedings of the meetings on Archives in Fields of Natural Sciences in FY2019
Feb. 25, 2021

NIFS-PROC-121
Edited by Hiroaki Ito and Tetsuo Ozak
Frontier of Advanced Pulsed Power Technology and its Application to Plasma and Particle Beam
Nov. 08, 2021

NIFS-PROC-122
National Institute for Fusion Science, National Institutes of Natural Sciences
Institute of Fusion Science, School of Physical Science and Technology, Southwest Jiaotong University
Hefei Keye Electro Physical Equipment Manufacturing Co. Ltd.
NIFS-SWJTU JOINT PROJECT FOR CFQS -PHYSICS AND ENGINEERING DESIGN-
VER. 4.1 2022. JAN.
Feb. 10, 2022

NIFS-PROC-123
Edited by Jun Hasegawa and Tetsuo Ozaki
Resent Developments of Pulsed Power Technology and Plasma Application Research
Feb. 5, 2023

NIFS-PROC-124
Frontiers of Pulse Power Technology Development
Edited by Weihua Jiang
Feb. 5, 2023

NIFS-PROC-125
Recent trends in technologies of pulse power, high-density plasma and particle beams
Edited by Koichi Takaki and Tetsuo Ozaki
July 1, 2023